INVESTIGATION OF TWINNING NUCLEATION AND PROPAGATION IN MAGNESIUM BY MOLECULAR DYNAMICS

by

Enver Kapan

B.S., Mechanical Engineering, Boğaziçi University, 2013

M.S., Mechanical Engineering, Boğaziçi University, 2016

Submitted to the Institute for Graduate Studies in
Science and Engineering in partial fulfillment of
the requirements for the degree of
Doctor of Philosophy

Graduate Program in Mechanical Engineering

Boğaziçi University

2023

ACKNOWLEDGEMENTS

"PhD is not fun!" once told Assoc. Prof. Jeremy Mason to me. I didn't understood that at the time since he seemed to be having fun in the research business. I can now concur his motto after all these arduous years of graduate study. Working on a scientific problem is not the only component to a graduate study; it takes more than that. It takes patience and dedication. These are two virtues not commonly combined in a young researcher. I feel obliged to thank him here for he had provided me with motivation and critical insight when I lacked them. He has been more than a collaborator in my project. My supervisors Assoc. Prof. C. Can Aydıner and Assist. Prof. Sertan Alkan have always been kind, attentive and patient. It is with these three remarkable mentors' guidance and brilliance that this dissertation was possible and I should acknowledge my privilege to have the chance of working with them. I thank the other members of the dissertation committee Prof. Nuri Ersoy, Prof. Türkan Haliloğlu and Prof. Güney Güven Yapıcı for their interest in my work and their constant support and positivity which has been a huge encouragement.

Friendship in academia is special. One makes close friends with similar taste in nature after a series of simple scientific discussions. At the beginning of my graduate study, I made three, what I call, fellow mentors; Dr. Mustafa Şengör, Dr. Fatih Ertuğrul Öz and Dr. Kenan Çınar, who were all PhD candidates at the time. I've learnt from them quite many details of experimentation, numerical techniques or just general aspects of mechanics and materials science that are typically overlooked in courses. They have become friends during these little 'classes' on the minutiae of our subject. I'll always remember their sincerity and grace. The Mechanics of the Advanced Materials Lab was a little community of precious people. Dr. Nima Şafak, Buğra Üçel, Necdet Özdür and Olcay Türkoğlu are lifelong friends of mine whom I met in the lab. The small talk in the lab were sometimes the saviors of the day during the times we felt overwhelmed. Also, it feels strange to look back and notice that what sometimes sustained my fascination with science and engineering were the short

discussions with these bright people. I'll also remember both the technical and non-technical conversations with dear friends Dr. Tolga Akıner and Umut Soysal from the department. All these people made my time in the department a joyous stint and they greatly contributed to my expertise as a researcher. The nice people of the Mason Research Group in UC Davis deserve a mention here. Dr. Ozan Burak Eriçok, Dr. Erdem Eren, Dr. Jared Stimac and Conner Winkeljohn were wonderful colleagues. Ozan and Erdem along with Vehbi Bayraktar and Ammar Haydari of the Turkish student community were my guides in the lovely town of Davis during my visiting research stint in Davis, California. My roommates Bedirhan Laçin, Jiregna Sheikata, our landlady Joanne Chambers and I became a closely-knitted family shortly after we settled in. The memories we share will always be remembered. I owe these folks a lot since my time in Davis had been truly a remedy for me after two years of uncertainty during the Covid-19 pandemic.

I would like to thank also my lifetime friends Cüneyd Özbaş, Dr. Ahmet Hakan Coşkun and Emirhan Ertugay, Dr. Zeynel Güler and others that will take pages to name for their incessant support. They have always been a second family to me and they helped me see the bigger picture in life whenever I engulfed myself into anxiety because of the worries of a typical PhD candidate.

Lastly, I express my infinite gratitude to my parents and siblings for everything. In time, I came to understand that family is everything in many regards and the devotion of parents to their children is unparalleled.

I would also like to thank TUBİTAK BİDEB for their endorsement. This work was supported and partially funded by the TUBİTAK BİDEB 2214-A research program under the project code 1059B141900441.

ABSTRACT

INVESTIGATION OF TWINNING NUCLEATION AND PROPAGATION IN MAGNESIUM BY MOLECULAR DYNAMICS

Modeling deformation twin nucleation in magnesium has proven to be a challenging task. In particular, the absence of a heterogeneous twin nucleation model which provides accurate energetic descriptions for twin-related structures indicates a need to more deeply understand twin energetics. To address this problem, in a two-part study, molecular dynamics simulations are performed to follow the energetic evolution of $\{10\bar{1}2\}$ tension twin embryos nucleating from an asymmetrically-tilted grain boundary. The line, surface and volumetric terms associated with twin nucleation are identified. A micromechanical model is proposed where the stress field around the twin nucleus is estimated using the Eshelby formalism, and the contributions of the various twin related structures to the total energy of the twin are evaluated. In the second part of the study, a geometric model is proposed to complement the micromechanical model such that the geometric variables associated with twin related structures are predicted from a few mesoscopic parameters. The results of the geometric model are substituted into the micromechanical model to obtain potential energy surfaces of a wide range of twin configurations. Classical nucleation theory is implemented to predict the nucleation energy barrier for $\{10\bar{1}2\}$ twinning in Mg. The reduction in the grain boundary energy arising from the change in character of the prior grain boundary is found to be able to offset the energy costs of creating the other interfaces. The defect structures bounding the stacking faults that form inside the twin are also found to possibly have significant energetic contributions. These results suggest that both of these effects could be critical considerations when predicting twin nucleation sites in magnesium.

ÖZET

MAGNEZYUM METALİNDE İKİZ ÇEKİRDEKLENMESİ VE YAYILIMININ MOLEKÜLER DİNAMİK METODU İLE İNCELENMESİ

Magnezyum malzemesinde deformasyon ikizi çekirdeklenmesinin modellenmesi oldukça çetrefilli bir problem teşkil eder. Özellikle, ikiz bağlantılı yapıların enerjetiğini doğru bir şekilde tarif eden heterojen bir ikizlenme modelinin olmayışı, ikiz enerjetiğinin daha derinlemesine anlaşılması gerektiğine işaret etmektedir. Bu problemi ele almak için, iki aşamalı bir çalışma dahilinde, önce bir asimetrik-eğik tanecik sınırından çekirdeklenen $\{10\bar{1}2\}$ çekme ikizi embriyosunun enerjetik evrimi moleküler dinamik simülasyonunda takip edildi. İkiz çekirdeklenmesi ile ilişkili doğrusal, yüzey ve hacim terimleri tespit edildi. İkiz etrafındaki gerinim alanlarını Eshelby formalizmi çerçevesinde tahmin eden bir mikromekanik model öne sürüldü. Bu mikromekanik model ile ikiz enerjisine dahil olan çeşitli ikiz yapılarının payları değerlendirildi. Çalışmanın ikinci kısmında, geliştirilen mikromekanik modeli tamamlamak maksadıyla, ikiz yapılarına ilişkin geometrik değişkenleri sınırlı sayıda orta ölçekli parametreden tahmin edebilen bir model ortaya konuldu. Bu geometrik modelin geniş bir ikiz konfigürasyon seti için sonuçları elde edildi ve mikromekanik modelde yerine konuldu. Böylece bu ikiz seti için potansiyel enerji yüzeyi elde edildi. Klasik ikizlenme teorisi kullanılarak, Mg için $\{10\bar{1}2\}$ ikizlenmesi için enerji bariyeri hesaplandı. Üzerinde ikizlenme gerçekleşen tanecik sınırının ikizlenmeyle karakter değiştirmesi neticesinde meydana gelen tanecik sınırı enerjisindeki düşüşün diğer ikiz yüzeylerinin oluşumu için gereken enerji yükünü karşıladığı bulundu. İkizlerin içinde yer alan dizilim hatalarının iki ucundaki doğrusal hataların da ikizin toplam enerjisine ciddi katkı yapmış olabileceği tahmin edildi. Bu sonuçlar, gözlemlenen bu iki etkinin magnezyumda ikiz çekirdeklenme mahallinin tespiti için kritik faktörler olabileceğini göstermektedir.

TABLE OF CONTENTS

LIST OF FIGURES

LIST OF TABLES

LIST OF SYMBOLS

$\mathbf{A}$	Regressor matrix
a_1, a_2	Major and minor semiaxes of the ellipse
a, b	Radii of the ellipse along/normal to the grain boundary
Al	Aluminum
b_i	Burgers vector length of the ith dislocation
C_{ijkl}	Elastic constants
dl	Infinitesimal elliptic arc segment
dl_{ctb}	Infinitesimal coherent twin boundary arc segment
dl_{pb}	Infinitesimal prismatic-basal boundary arc segment
$d_\perp$	Vertical separation between two stacking faults
e	Eccentricity of the ellipse
E_{inh}	Elastic strain energy
K	Elastic pre-constant
K_1, K_2	First and second invariant planes for a twin mechanism
k_B	Boltzmann constant
$l_\perp$	Separation between the bounding stacking faults
m, m'	Slopes of a stacking fault line and the conjugate diameter
Mg	Magnesium
$\hat{n}$	Unit vector along the outgoing normal at a point on the ellipse
r_i	Length of the ith stacking fault
r_{SF}	Average length of stacking faults
r_0	Reference separation of the ends of a stacking fault segment
S_{ijkl}	Eshelby tensor
t	Thickness of the nucleus (ellipse) in the z-direction
T_D	Debye Temperature
Ti	Titanium
V	Volume

α	Angle of the tangent line at a point on the ellipse
β	Atomic jump frequency
γ_{CTB}	Interfacial energy of the coherent twin boundary
γ_{SF}	Stacking fault energy
γ_{PB}	Interfacial energy of the prismatic-basal twin boundary
$\gamma_{\Delta\Gamma}$	Change in the interfacial energy of the grain boundary
ΔE	Change in the potential energy
$\Delta\Gamma$	Transforming grain boundary upon twinning
δ_{max}	Maximum bulging distance of a twin nucleus
ε_{ij}	Strain tensor
ε^p	Eigenstrain associated with the active twin mechanism
η_1, η_2	First and second invariant directions for a twin mechanism
θ	Grain boundary inclination
ρ_{SF}	Linear density of stacking faults inside a twin
σ_{ij}	Stress tensor
ϕ	Inclination of the c-axis of the parent grain
ψ	Parametric angle for the ellipse

LIST OF ACRONYMS/ABBREVIATIONS

ATGB	Asymmetrically Tilt Grain Boundary
BP/PB	Basal-Prismatic/Prismatic Basal Incoherent Twin Boundary
CNT	Classical Nucleation Theory
CRSS	Critical Resolved Shear Stress
CTB	Coherent Twin Boundary
DXA	Dislocation Extraction Algorithm
EBSD	Electron Back-scattered Diffraction
G1, G2, G3, G4	Grains 1,2,3 and 4
HCP	Hexagonal Close-Packed
LAMMPS	Large-scale Atomic/Molecular Massively Parallel Simulator
LP	Load Point
MEP	Minimum Energy Pathway
MD	Molecular Dynamics
NPT	Isothermal Isobaric Ensemble
OVITO	Open Visualization Tool
PTM	Polyhedral Template Matching
SF	Stacking Fault
STGB	Symmetrically Tilt Grain Boundary
TEM	Transmission Electron Microscopy
ZTS	Zero Temperature String

1. INTRODUCTION

1.1. Motivation

The demand for efficient lightweight structures that also have high durability has significantly increased interest in lightweight metal alloys. In recent years, the lightweight trio (aluminium (Al), titanium (Ti) and magnesium (Mg) alloys) have seen growing deployment in structural applications like transportation vehicles, aerospace structures and also electronic device casings. Densities of the lightweight metals are significantly lower than steel, which is the most conventional structural material. Al and Ti have densities of $2700\,\frac{kg}{m^3}$ and $4500\,\frac{kg}{m^3}$ respectively, while steel has a density of $7800 - 8000\,\frac{kg}{m^3}$. Mg alloys, with a strikingly low density of $1740\,\frac{kg}{m^3}$, hold special promise for increasing fuel efficiency in transportation through light-weighting [1, 2]. The advantage and potential of Mg in lightweight applications is even more obvious from the strength vs. density map of different classes of materials provided in Figure 1.1 where it is easily noticeable that the Mg alloy family resides at the leftmost region of the metals family. The abundance of Mg, the ninth most abundant element in the universe [3] and eighth in the Earth's crust [1], is another factor that contributes to its eligibility as a structural material for lightweight applications.

Despite all the potential of Mg alloys as candidate lightweight materials, use remains limited due to poor *ductility*, the ability to elongate without breaking, and *formability*, the ability to take arbitrary shape. Figure 1.2 shows the strength vs. elongation map of commonly used metals. As seen from the figure, Mg alloys have a narrower elongation range, with most ductile Mg alloy achieving a room temperature maximum elongation of around 20% whereas Al and Ti alloys can have more than $> 40 - 50\%$ elongation. The problem of low formability is further worsened in wrought magnesium alloys due to the crystallographic textures that develop during processing causing severely anisotropic deformation behavior [4]. Low ductility causes Mg alloys to fail in a very brittle fashion, i.e. they do not elongate much before they suddenly break.

Due to the sudden nature of failure, brittle failure is generally named catastrophic failure, suggesting the importance of ductility for material and structural safety. Low formability, linked to low ductility, complicates the processing of Mg alloys and pushes up manufacturing costs. Both factors remain as significant obstacles to the widespread use of Mg in lightweight applications.

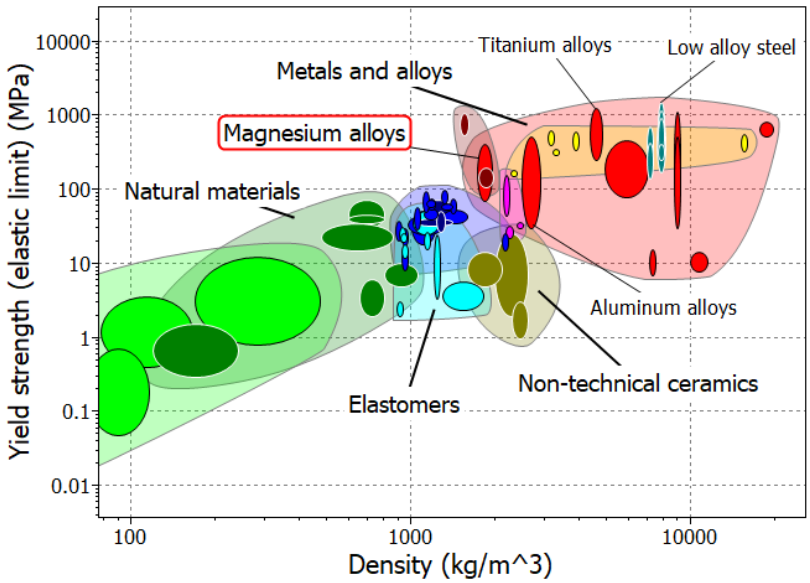

Figure 1.1. Strength vs. density mapping of engineering material families. Magnesium alloys reside at the leftmost region of metals.

Efforts to solve the decades-standing problem of low formability of Mg alloys attracted intensified research interest as global scale energy and environmental problems became urgent. The culprit behind poor formability is the limited number of easy dislocation glide (i.e. slip) systems that can accommodate deformation [5]. In Mg, easy slip is confined to the basal plane of the hexagonal close-packed (hcp) lattice. The pyramidal $\langle c + a \rangle$ slip systems that operate out of the basal plane (in the c-axis direction) require about two orders of magnitude higher stresses to activate compared to basal slip. Taylor's criterion [6] states that, for a polycrystalline metal to accommodate an arbitrary homogeneous plastic deformation, five independent slip systems are necessary. Thus, in the case of Mg, the Taylor's criterion is not satisfied. However, as Kocks and Westlake pointed out [7], the lack of easy slip systems in low-symmetry

structures may be compensated by activation of localized deformation (mechanical) twinning around high stress concentration regions, typically occurring on or near grain boundaries [8–10]. Several modes of deformation twinning including $\{10\bar{1}2\}$, $\{10\bar{1}1\}$ and $\{10\bar{1}3\}$ have been experimentally observed in Mg under different loading conditions [11–15]. The $\{10\bar{1}2\}$ mode, among them, is found to be profuse in bulk Mg [16].

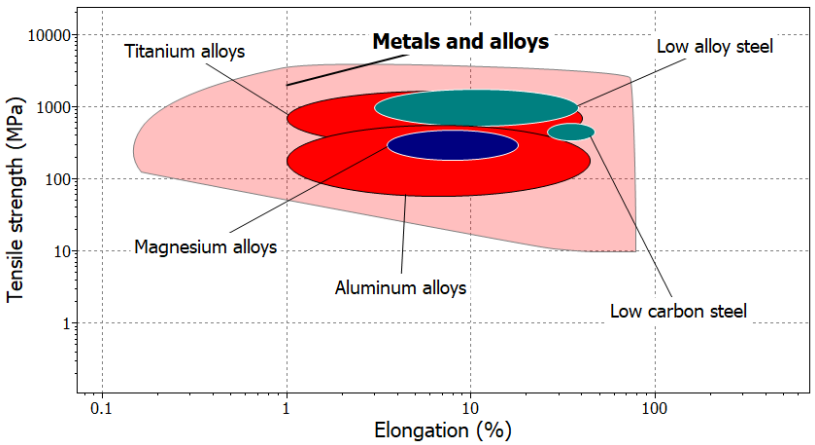

Figure 1.2. Strength vs. max. elongation mapping of engineering material families. Magnesium alloys reside in the middle region of metals.

Deformation twinning is central to the microscale and macroscale mechanical behavior of Mg. First, twinning is at the root of plastic anisotropy observed in textured polycrystals of Mg alloys subjected to tension-compression cycles, prompting the sigmoidal shape of the stress-strain curves [17, 18]. This is due to the polar nature of deformation twinning, i.e. a twinning mode activates under only one sense of the load. For example, the $\{10\bar{1}2\}$ mode is an extension twin mode in Mg, i.e. it only operates when there is elongation along c-axis of the parent grain. This becomes crucial in the case of reversed loading of textured samples where the grains have preferred orientations. In such cases, twinning is substantially active during only one stage of the loading. When the load sense is reversed, first the previously formed twins are partially reversed and then other slip mechanisms activate, effectively changing the entire behavior [19]. Secondly, twinning is directly linked to macroscale strain localization patterns characteristic of some wrought Mg alloys. The connection between strain localization and twinning in Mg alloys is highlighted in a series of experimental

investigations through digital image correlation analysis. In an initial study, Aydıner and Telemez [20] revealed that the macroscale shear bands, constituted by local coordination of individual $\{10\bar{1}2\}$ twins, encompass the entire sample. Kapan et al. [21] demonstrated the contrasting localization patterns in rolled and extruded samples of a Mg alloy due to changed coordination networks of twins inside different relative grain orientation populations. Later, Shafaghi et al. [22] resolved the cyclic strain heterogeneity patterns at the grain scale in a rolled Mg sample and further showed that the heterogeneity patterns linked to different deformation mechanisms begin to coexist in later cycles. They concluded that the insistence of strain localizations through cycles possibly sheds light on the damage accumulation process and requires careful consideration. Corroborating this conclusion, twinning is associated with damage accumulation and failure in Mg alloys in several electron microscopy studies [23–27]. It is shown that the $\{10\bar{1}2\}$ twin mechanism contributes to cyclic damage accumulation due to dislocation-twin interactions and twin boundaries acting as stress concentration and crack initiation sites. In fatigue failure, increasing remnant twin density was shown to be a main factor in failure of the material [24, 28, 29]. Lastly, twinning influences the texture evolution during processing/forming [30, 31].

Simulating these mesoscale phenomena in Mg by continuum level crystal plasticity models is challenging since dislocation slip and twinning are intrinsically different mechanisms. A continuum model that embodies the essential features of both mechanisms is elusive. Dislocations are line defects disrupting the atomic order of crystals [32]. They have many orders of magnitude smaller sizes than an individual grain and are available, in the probabilistic sense, at every region inside a grain. Dislocation slip-based deformation involves gliding motion of a large number of dislocations, resulting in a distribution of simple shearing events inside the structure. The aggregate of these individual shearing events gives the total plastic deformation of the observed material. The spatially diffuse character of slip allows for point-wise analysis of strain distribution at the sub-grain level [33–35]. This is achieved by formulation of a slip condition at a material point based on the Schmid's law, which states that a single incremental shearing/slip event takes place at a point if the shear stress resolved on

the slip plane at that point exceeds a critical value (i.e. a critical resolved shear stress, CRSS). Thanks to the diffuse nature of slip, grain-scale crystal plasticity formulations have been successful in modeling the macroscopic elasto-plastic behavior of conventional metallic materials that deform predominantly by slip [35].

In contrast to dislocation slip, twinning prompts a localized finite strain accompanying the abrupt reorientation of a region of the parent crystal. In the resultant state, the twinned region of the crystal is separated from the parent crystal by sharp interfaces. Clearly, the mathematical framework developed for the distributed/delocalized deformation induced by slip activity is unfit to describe the twinning mechanism. Early attempts to incorporate the deformation twinning mechanism into the established crystal plasticity models introduced the idea of a pseudo-slip scheme [36,37] where a volume fraction parameter is devised to implicitly account for the twinned part of the material. Accordingly, an integration point (in the models with spatial resolution) can be, effectively, at a superposition state of twinned and not twinned and the volume fraction parameter indicating the twinned volume fraction. This representation contradicts the physical case where twinning at a point is binary, i.e. a material point (or an atom at the atomic scale) belongs to a region that is either twinned or not twinned. Likewise, the twinning condition in this approach mimics Schmid's law which is based on the macroscopically resolved shear stress whereas the actual interior and exterior stress states of a twin have been experimentally shown to be drastically different [38]. Besides, Schmid's factor is shown to be inadequate in determining the activated twin variant in heterogeneous nucleation events [39]. As a result, the pseudo-slip approach fails to accurately predict critical deformation phenomena, with peculiar macroscale strain localization patterns being the preeminent example. Evidently, a truly explicit twin formation model is needed to inform physically valid mesoscale models. Such a model must be able to describe the formation of new interfaces and other structures associated with the twin, predict the initiation site as well as the critical size and shape of a sustainable twin nucleus, and calculate the energy barrier for a given twin nucleation event. Recently developed crystal plasticity models that incorporate various explicit twinning schemes fail to fully meet these requirements [40–43] (for a

comprehensive discussion on these efforts see Refs. [44–46]). A rigorous understanding of twinning physics is necessary for the development of accurate crystal plasticity models that satisfactorily incorporate twinning.

The characteristics of individual twinning events and the twin-related structures at play have been extensively studied using electron microscopy, theoretical crystallographic calculations [47–49] and molecular dynamics (MD) simulations. In particular, MD studies have been successful in aiding the identification of the atomic structure of the faceted twin boundary comprising coherent and incoherent segments [50–53], computation of interfacial energies of these boundaries [54–58] and the comprehension of twin growth kinetics correlated with twin boundary mobility [59–63]. The MD method was also used to simulate the defect substructure of twins. Notably, the atomic structure of the experimentally identified I_1 type stacking faults [64–66] has become a focus in recent MD studies [66–71] due to its potential role in twin boundary mobility. A brief review of other MD studies that focus on twinning is presented in Chapter 3.

Mechanistically, twin formation occurs in steps involving the nucleation, propagation and growth (thickening) stages as sketched in Figure 1.3a-c [72]. In a typical twinning event, first, a stable twin embryo forms in the nucleation stage. Upon reaching a critical size, it propagates with the advance of the twin tip (front) across the crystal [73]. In a polycrystal material, a complete propagation stage ends when the twin tip reaches another grain boundary or another defect, e.g. another twin boundary. At the early propagation stage a typical twin is only a few atomic layers thick and it is elongated towards the interior of the grain. This is typically characterized by the needle shape of twins that appear in the electron back-scattered diffraction (EBSD) data [74]. The growth stage entails the growth of the twin in the normal direction to the twin plane. The growth process is facilitated by complex shear/shuffle processes [50, 75] which add new layers to the twinned region [54, 76–78]. Intriguingly, some in-situ studies reported suppression of the grain growth towards grain interior when a bulk Mg alloy is cold-worked as sketched in Figure 1.3d [79]. Instead, they observed multiple nuclei originate from low-angle grain boundaries, then grow along the grain boundary

and eventually coalesce upon further loading/processing (Figure 1.3d-e). This behavior differs from the typical twinning stages summarized above. These different twin growth modes may be consequential to the higher twinnability of a special subset of grain boundaries and/or the twin boundary mobility inside the parent grain. Clearly, the effect of the grain boundary character on the twin progression is notable and worthy of deeper investigation.

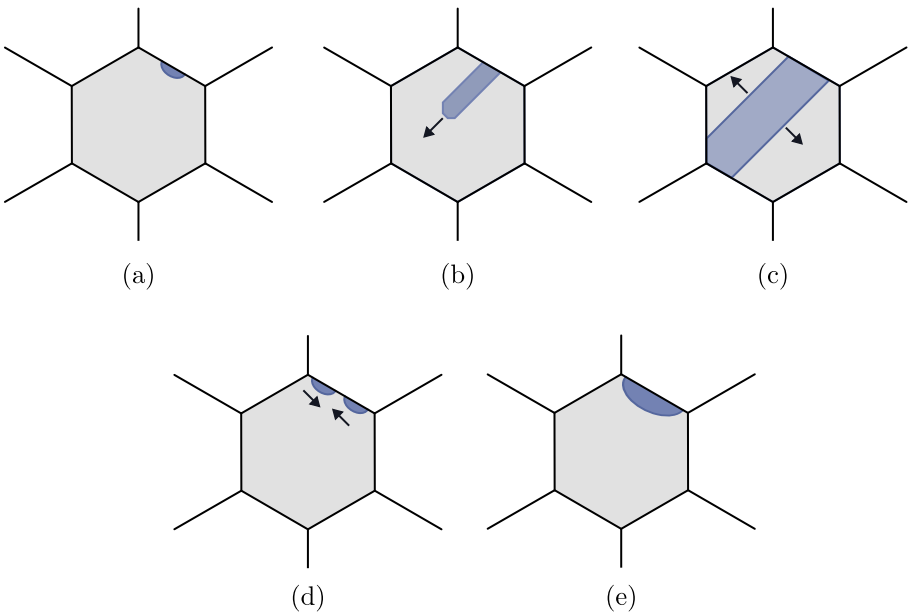

Figure 1.3. Sketches show (a-b-c) the nucleation, propagation and growth stages of deformation twinning. (d-e) Alternatively, multiple twin nuclei can nucleate from the same grain boundary. Depending on the character of the grain boundary, these nuclei can grow along the grain boundary and coalesce to generate a larger twin [79].

Of twinning stages, the nucleation problem has proven to be particularly difficult though. Experimentally, twin nucleation is too abrupt such that an appreciable twin observed in a transmission electron microscope (TEM) is almost already in the early-growth stage, defying a clear examination of the nucleation stage [80]. In fact, visualization of a twin embryo in the early-propagation stage at the atomic resolution has been realized only very recently [77, 81–83]. In addition, twinning is a heterogeneous event driven by the the complicated and variable high stress regions around preexisting defects (e.g. grain boundaries [84–87], dislocation pile-ups [88], twin bound-

aries [89, 90]), making the prediction and inspection of a possible twin nucleation site difficult. Atomistic simulations are employed to offset this limited experimental capability in studying nucleation physics. However, the exact mechanism of a twinning event varies with the nucleation site in a polycrystal, limiting the ability of diverse MD simulations designed to study specific twinning events to provide generic information (as briefly explained in Chapter 3). Energy-based theoretical models have been a tool used to study the nucleation/formation problem, with atomic-scale simulations receiving from such theories.

Analytical models give insight about the critical geometry and nucleation energy barrier for the formation of a stable twin embryo for different twin morphologies. Lee and Yoo [91], using classical nucleation theory (CNT), investigated the effect of the orientation of the applied stress on the aspect ratio of a nucleated twin. In their model, the elastic strain energy caused by the transformation shear as well as the interaction energy between the applied stress field and the stress field of the twin are calculated using Eshelby's inclusion theory; Eshelby theory constitutes a very powerful framework to model a wide range of twin-related phenomena. However, they ignored the contribution of the twin boundaries to the total energy of the twin. In a later study [92], they computed the nucleation energy barrier and the critical aspect ratio for a spheroidal shaped twin under a given applied stress state in a model hcp material. This time, they computed the interfacial energy of the twin boundary using MD and incorporated it into the total twin energy expression. They concluded that the nucleation barrier depends sensitively on the twin boundary energy. However, they assumed that the twin is surrounded by the coherent twin boundary only, whereas TEM studies have resolved different types of twin boundaries including the prevalent basal-prismatic (BP) or prismatic basal (PB) incoherent twin boundaries [53, 76]. Nevertheless, this pioneering study showcases the combination of MD and micromechanical theory to achieve a continuum model informed by atomistic detail. CNT, in conjunction with Eshelby theory, was later used by Lebensohn and Tome [93] to investigate the stress-state associated with twin nucleation. They concluded that the effect of stress components normal to the twin plane becomes relevant only if those components are an order of

magnitude larger than the resolved shear stress. Recently, Liu et al. [94] used the same method to calculate the nucleation energy barrier and critical aspect ratios (both in- and out-of-plane) of a homogeneously nucleated spheroidal shaped twin without any prior assumptions made on the morphology of the twin. They also calculated the stress field around the twin while considering the effect of plastic deformation triggered by the exterior stress field of the twin. Liu et al. [95] further showed that the interaction energy of the stress-fields of the primary and secondary twins in a grain is minimized when the total stress fields in the vicinity of their junction boundary are favored by both twins. Paudel et al. [96] used a micromechanical formulation based on the Eshelby solution to calculate the elastic fields of twins nucleating in a textured Mg under a three-point bending condition. They calculated a CRSS value for $\{10\bar{1}2\}$ twinning and predicted the twin spacing in the case of multiple twinning. Eshelby theory was also used to predict precipitation hardening effects on twinning in Mg alloys [97] and was combined with the phase-field method to simulate the auto-catalytic nucleation of $\{10\bar{1}2\}$ twins in Mg [98].

The cited analytical studies demonstrate impressive computational speed in determining critical physical properties, such as the nucleation energy barrier. Leveraging the scale independence of the continuum framework of Eshelby inclusion theory, these studies retain generality even at the atomic level. However, it is essential to acknowledge that these studies do not account for all factors that could contribute significantly to the total energy of the twin. Notably, the excess energies associated with characteristic defect substructures and the transformation of the grain boundary on which the twin nucleates are not considered. The latter factor in particular could be crucial, given that grain boundaries serve as the primary sites for twin nucleation and their character could dictate the direction of further twin growth [79].

1.2. Scope and Outline of the Thesis

A heterogeneous twin nucleation model which provides accurate energetic descriptions for twin related structures is still absent. The aim of this thesis is to achieve

such a model for heterogeneous $\{10\bar{1}2\}$ twin nucleation in polycrystalline Mg. Understanding twin nucleation is important, not just to precisely capture the characteristics of the initial stage, but also to reasonably predict the ensuing propagation and growth stages. Here, the main goal is to obtain a micromechanical formulation that predicts the critical size, critical shape and the energy barrier for the formation of a stable twin nucleus on a grain boundary. These key pieces of information may enable an explicit twin scheme in a crystal plasticity model that incorporates the physical features of a twin. Classical nucleation theory, in its simplest form, can predict the energy barrier, size and geometry of a twin embryo in the case of homogeneous nucleation. However, it needs to be extended to describe a heterogeneous event by including energetic terms associated with the heterogeneous nucleation mechanisms of twinning in the total energy expression. Identification of such terms requires atomistic details which can be obtained via MD simulations. Hence, the present study combines MD with micromechanical theory to analyze twin energetics by proposing an efficient and systematic bridging of atomistic information to continuum scale models.

To this end, MD simulations are performed in Chapter 3 to follow the energetic evolution of $\{10\bar{1}2\}$ tension twin embryos nucleating from a grain boundary. The line, surface and volumetric terms associated with twin nucleation are identified. A micromechanical model is proposed where the stress field around the twin nucleus is estimated using the Eshelby formalism, and the contributions of the various twin-related structures to the total energy of the twin are evaluated.

In Chapter 4, a geometric model is constructed for an elliptic cylinder shaped twin originating from a grain boundary. The model takes into account several microstructural parameters, including the inclination of the grain boundary, the orientation of the parent grain and the dimensions of the twin. It yields the areas of the distinct twin boundaries, the lengths of individual stacking fault lines inside the twin, and the twin volume. The outputs of the geometric model are then imported to the micromechanical model obtained in Chapter 3. Without such a geometric model, those quantities have to be computed from MD simulations for each twin configuration. Availability of

a geometric model that can estimate those quantities as functions of the shape of the ellipsoidal twin reduces the computational cost dramatically. Then, the total potential energy surfaces for nuclei with varying configurations are computed at different applied load levels. The saddle points of these potential energy surfaces, which indicate the nucleation energy barrier and the size and shape of the critical nucleus at the corresponding load level are found using a steepest-descent algorithm within the classical nucleation theory framework.

Potential future work is discussed in Chapter 6. A brief introduction to deformation mechanisms in Mg, the molecular dynamics method, Eshelby inclusion theory and the classical nucleation theory is provided in Chapter 2.

2. BACKGROUND

Mg plastically deforms through a combination of dislocation slip and deformation twinning systems. Thus, the contrasting characteristics of the two mechanisms deserves a brief discussion here. At the atomic level, dislocation mediated slip is conveyed via the glide of dislocations over certain crystallograpic planes (slip plane) in certain directions (slip direction). The dislocation glide is, in general, favorable over the densest planes, called close-packed planes, in a densely packed direction. These systems activate when the resolved shear stress over the slip plane exceeds CRSS for that slip system. On the other hand, slip activation over non-close-packed planes requires much higher stresses or higher thermal energy for the mobilization of the dislocation core. Mg has an hcp crystal structure with an $ABABAB...$ stacking of the close-packed planes with the result that the easy glide of dislocations is only feasible over the basal plane of the Mg lattice. At the crystal level, an overall shape change is achieved through the individual glide of many dislocations as sketched in Figure 2.1a.

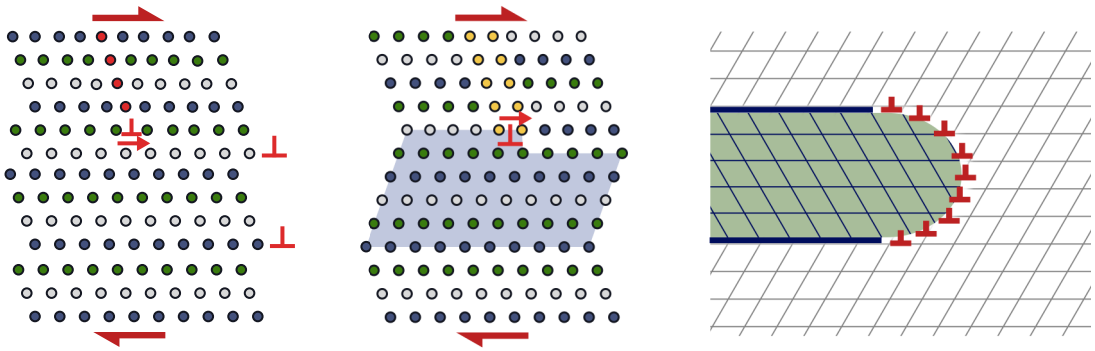

Figure 2.1. Achievement of shape change via (a) dislocation glide versus (b) deformation twinning. (c) Coordinated glide of partial dislocations for twin propagation.

In contrast, in deformation twinning, a shape change is achieved through reorientation of a region (twin) inside the original crystal as sketched in Figure 2.1b. Further evolution of the twin can be mediated by the coordinated movement of partial disloca-

tions over the twin/parent interface. A visualization of this mechanism is demonstrated for a simple crystal structure in Figure 2.1b. The twin interface is translated by one atomic plane normal to itself with the glide of the partial dislocation on the interface, denoted by the '$\perp$' sign, to the right. In 3D, the propagation or growth of involves, not just one, but localized and coordinated glide of many partial dislocations on the twin interface as sketched in Figure 2.1c. In more complex lattices, the migration of the twin boundary might involve more complex atomic motions than just the glide of partial dislocations.

2.1. Plastic Deformation Mechanisms in Magnesium

The slip planes and directions of common dislocation slip systems observed in bulk Mg are listed in Table 2.1 and are indicated inside representative hcp unit cells in Figure 2.2a-d. Here the $a_1 - a_2 - a_3 - c$ axes denote the inherent coordinate system used for hexagonal symmetry. The a_i-axes lie in the (0001) basal plane and the c-axis denotes the perpendicular direction to the basal plane. As noted above, basal $\langle a \rangle$ slip is the easiest slip mechanism. The reported CRSS values for the basal $\langle a \rangle$ system range between 0.8-10 MPa [99, 100]. The prismatic $\langle a \rangle$ slip is the next easiest slip system. Basal slip systems and prismatic slip systems together comprise 4 easy systems which is still less than the 5 systems required to be able to achieve arbitrary shape change. Pyramidal I $\langle a \rangle$ slip does not provide an extra independent slip system as its slip direction is coplanar with the basal and prismatic slip. On the other hand, the pyramidal II $\langle c + a \rangle$ slip system can provide c-axis straining. However the relative activity of this system compared to the basal $\langle a \rangle$ slip is found to be around 0.1 [99] due to its 50-100 times higher CRSS value than that of basal $\langle a \rangle$ slip [101–105].

The hard $\langle c + a \rangle$ slip is shown to be active only in very limited plasticity in the case of c-axis straining of Mg single crystals [106]. Associated with this, the dominant response to straining along the c-axis in Mg is twinning. The common twin modes observed in Mg are the $\{10\bar{1}2\}$ extension and $\{10\bar{1}1\}$ compression modes. The twin planes and directions for these mechanisms are illustrated in Figure 2.2e-f. $\{10\bar{1}1\}$ twin

mode require higher stresses to activate. Like $\langle c+a \rangle$ slip, $\{10\bar{1}1\}$ twinning is found to be active only to a very limited extent and it is typically associated with failure at low strains [14]. The $\{10\bar{1}2\}$ mode is, on the other hand, ubiquitous in Mg and is the focus of this study.

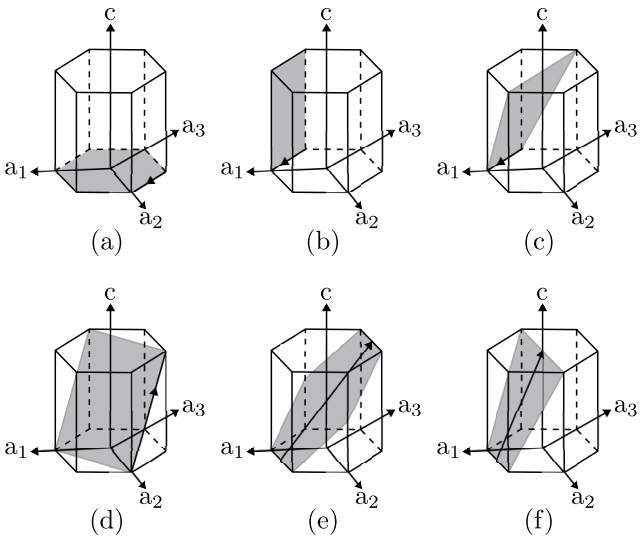

Figure 2.2. Common slip and twinning systems found in Mg and Mg alloys. (a) basal slip: $\{0001\}\langle 11\bar{2}0\rangle$, (b) prismatic slip: $\{1\bar{1}00\}\langle 11\bar{2}0\rangle$ (c) pyramidal $\langle a \rangle$ slip: $\{1\bar{1}01\}\langle 11\bar{2}0\rangle$ (d) pyramidal $\langle c+a \rangle$ $\{11\bar{2}2\}\langle 11\bar{2}3\rangle$ slip, (e) extension twin, $\{10\bar{1}2\}\langle \bar{1}012\rangle$, (f) $\{10\bar{1}1\}$ compression twin, $\{10\bar{1}1\}\langle \bar{1}011\rangle$.

Table 2.1. Primary slip systems in Mg and Mg alloys.

Slip system no.	Burger's vector	Slip direction	Slip plane	No. of independent sys.
basal	a	$\langle 11\bar{2}0\rangle$	$\{0001\}$	2
prism (type I)	a	$\langle 11\bar{2}0\rangle$	$\{10\bar{1}0\}$	2
pyramidal (type I)	a	$\langle 11\bar{2}0\rangle$	$\{10\bar{1}1\}$	4
pyramidal (type II)	c+a	$\langle 11\bar{2}3\rangle$	$\{11\bar{2}2\}$	5

2.1.1. Deformation Twinning

From the crystallographic standpoint, the twin lattice has a mirror symmetry with the parent lattice with respect to a twin plane (called K_1). The crystallographic

relation between the twin and parent lattices for the $\{10\bar{1}2\}$ mode is illustrated with representative unit cells of the respective lattices in Figure 2.3a.

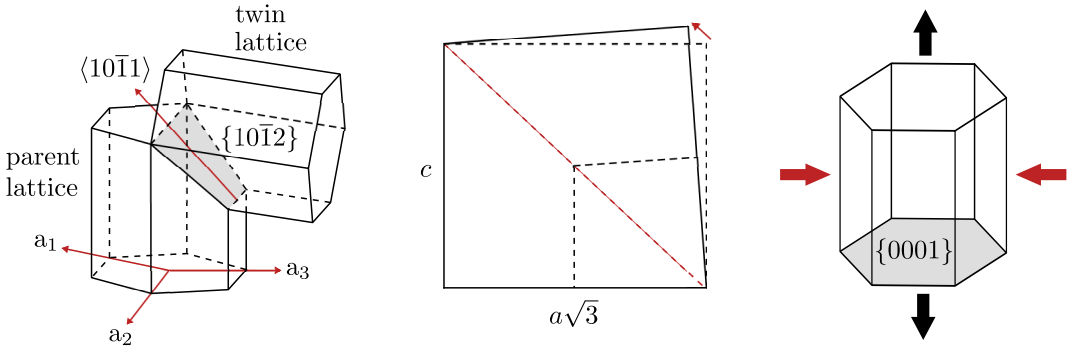

Figure 2.3. (a) Relative orientations of the parent and twin lattices with respect to the mirror (twin) plane. (b) The shearing motion over the plane of shear seen from the side view. (c) Direction of loading that triggers $\{10\bar{1}2\}$ extension twin activation in Mg.

During the reorientation of the twin, there are two planes and two directions that remain invariant (i.e. undistorted) [72]. The first invariant plane is the K_1 plane that constitutes the mirror plane. For the $\{10\bar{1}2\}$ mode shown in Figure 2.3a, the K_1 plane is the $\{10\bar{1}2\}$ plane. The second invariant plane K_2 has the same form as K_1 and is also called the conjugate twin plane. The first invariant direction η_1 lies in the K_1 plane. For the $\{10\bar{1}2\}$ mode sketched in Figure 2.3a, η_1 is the $\langle 10\bar{1}1\rangle$ direction. From the continuum perspective, deformation twinning kinematically corresponds to simple shearing of the atomic planes parallel to the twin plane in the η_1 direction as shown in Figure 2.3b. This simple shearing definition can also be deduced in Figure 2.1b by discerning the shape change the twinned region (shaded blue region) undergoes relative to the rest of the material. The twin lattice can also be obtained through reflection of the parent lattice with respect to K_1 or, equivalently, 180° rotation about η_1. This has the effect of reorienting the twin by ~86°. The second invariant direction η_2 lies in the K_2 plane and is perpendicular to the intersection of K_1 and K_2 planes. These four elements describe a twin mode crystallographically. η_1, η_2, and the normals of the K_1

and K_2 planes all lie in the shear plane of the twin which coincides with the plane of paper in Figure 2.3b.

Twinning operates only in one direction of shear because the mirror image configuration is obtained by shearing in only one direction as shown in Figure 2.3b. The operative direction of a twin mode is determined from the lattice constants. If $\frac{c}{a} > \sqrt{3}$ for a given hcp crystal then the $\{10\bar{1}2\}$ mode causes extension in the c-axis direction and vice versa. For Mg, since $\frac{c}{a} = 1.624$, which is less than $\sqrt{3} = 1.732$, the $\{10\bar{1}2\}$ mechanism is an extensive mode. Hence, the $\{10\bar{1}2\}$ mode can be activated by tensile straining along the c-axis. As seen in Figure 2.3c, this can be achieved through either direct tension along the c-axis or compression parallel to the basal plane.

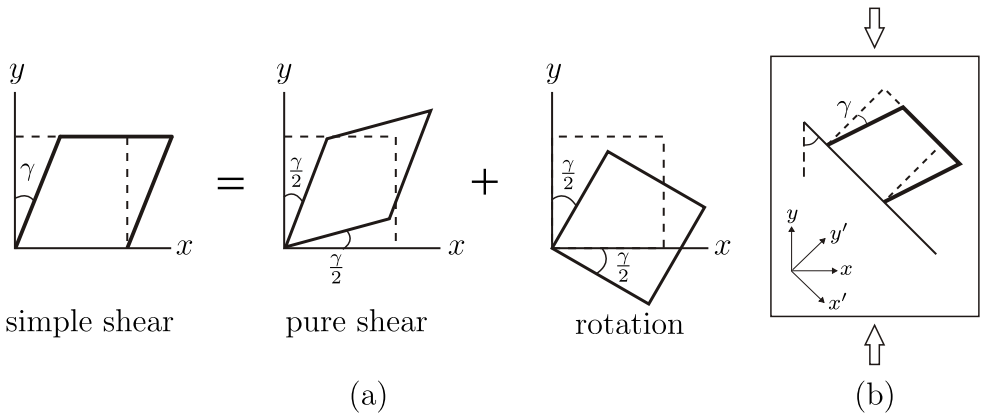

Figure 2.4. (a) Pure shear and rotation components of a simple shear. (b) The effect of simple shear over the shear plane corresponds to extension and contraction in the principle axes directions.

In contrast to slip, the magnitude of the shear caused by twinning is exact due to the precise symmetry relation between the twin and the parent grain. The magnitude of the characteristic twin shear is, again, determined by the dimensions of the unit cell. For Mg, the $\{10\bar{1}2\}$ mode induces a ~13% shear. The strains that arise due to simple shearing during twinning are *eigenstrains*, i.e. they do not cause elastic stresses in the bodies that twin without external constraints. Kinematically, the simple shear induced by twinning can be decomposed into pure shear and rotation components as depicted

in Figure 2.4a. The pure shear component is related to the actual distortion of the twinned region and the rotation part imposes only a rigid-body rotation. The shear strains prescribed by the pure shear are equal to the half of the characteristic shear as seen in Figurereffig:simplesheara. These shear strains give the eigenstrain associated with the twin mode. Accordingly, the eigenstrain for the $\{10\bar{1}2\}$ mode in Mg, in the twin-native coordinate system denoted by the $x' - y'$ axes in Figure 2.4b, is

$$\boldsymbol{\varepsilon}^{p'} = \begin{bmatrix} 0 & \frac{\gamma}{2} & 0 \\ \frac{\gamma}{2} & 0 & 0 \\ 0 & 0 & 0 \end{bmatrix} = \begin{bmatrix} 0 & 0.065 & 0 \\ 0.065 & 0 & 0 \\ 0 & 0 & 0 \end{bmatrix}. \tag{2.1}$$

The effect of pure shear is manifested by extension and contraction along the principal strain axes directions. For the $\{10\bar{1}2\}$ mode in Mg, since the reorientation angle is $\sim 86^\circ \approx 90^\circ$, the principal strain axes are closely aligned with the c-axis and the basal plane. This can be visualized by considering Figure 2.3c and Figure 2.4b together where the principle strain axes closely align with the $x - y$ axes that lie along the c-axis and basal plane directions respectively. Then, the eigenstrain in the principle coordinate system can be obtained through a basis change by $\sim 45^\circ$ as

$$\boldsymbol{\varepsilon}^{p} = \begin{bmatrix} \cos 45 & \sin 45 & 0 \\ -\sin 45 & \cos 45 & 0 \\ 0 & 0 & 1 \end{bmatrix} \begin{bmatrix} 0 & \frac{\gamma}{2} & 0 \\ \frac{\gamma}{2} & 0 & 0 \\ 0 & 0 & 0 \end{bmatrix} \begin{bmatrix} \cos 45 & -\sin 45 & 0 \\ \sin 45 & \cos 45 & 0 \\ 0 & 0 & 1 \end{bmatrix} = \begin{bmatrix} \frac{\gamma}{2} & 0 & 0 \\ 0 & -\frac{\gamma}{2} & 0 \\ 0 & 0 & 0 \end{bmatrix}. \tag{2.2}$$

Besides twin kinematics, twin nucleation is another central aspect of twinning. It involves formation of a *thermodynamically stable twin embryo*, where a small region of the material (consisting of $\approx$ 10 to 20 atomic planes) is twinned [107]. During nucleation, the excess energy introduced by formation of a twinned region and the associated boundaries (twin-grain surfaces) must be balanced by the dissipation of strain energy imposed by external loading. There are multiple ways to form a twin, each implying a different kind of atomic motion [32]. Possible mechanisms, illustrated in Figure 2.5 for the case of twinning with respect to the middle plane of the simple cubic crystal shown, include (a) pure glide, (b) glide+shuffling, (c) parallel shuffling and (d) pure shuffling. The exact reactions that yield twin formation are still debated. Therefore, an energy based approach to the twin nucleation problem is desired for

its generality as it does not presume any particular twinning mechanism. Molecular dynamics simulations are employed, on the other hand, to capture the atomic details.

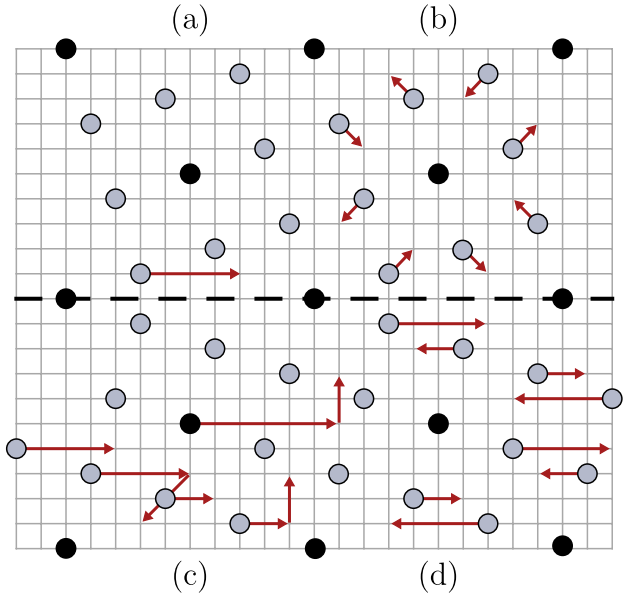

Figure 2.5. Achievement of twinning via (a) glide, (b) pure shuffling, (c) combination of glide and shuffling, (d) pure shuffle parallel to the twin boundary (see Ref. [32] for further discussion).

2.2. Essentials of Molecular Dynamics Simulation

In molecular dynamics, a system is defined by the positions and momenta of its constituent atoms. Atoms are pictured in an idealized form where the position of an atom is assumed to be the position of the center of its nucleus, and all interactions between atoms are described by an interatomic potential. The main idea is to compute the forces on each atom from the interatomic potential, and then solve Newton's equations to determine the trajectories of their movement.

Starting with Newton's second law, the force on atom i in a system with N atoms is

$$\boldsymbol{F}_i = m_i \boldsymbol{a}_i = \frac{\mathrm{d}^2 \boldsymbol{r}_i}{\mathrm{d}t^2}. \tag{2.3}$$

For conservative forces, the negative of the gradient of the potential energy with respect to an atom gives the force on that atom. Hence, following the notation used in Ref. [108], the force on atom i is written as

$$\boldsymbol{F}_i = -\nabla_i U\left(\boldsymbol{r}_1, \boldsymbol{r}_2, \boldsymbol{r}_3, ..., \boldsymbol{r}_N\right) = -\nabla_i U\left(\boldsymbol{r}^N\right), \tag{2.4}$$

where the gradient is taken with respect to the coordinates of atom i. The interatomic potential U approximates the sum of interaction energies between atoms in a system and is a function of coordinates of atoms. These interactions include, but are not restricted to, the effects of overlapped electronic shells around nuclei, the interaction of dipoles due to electronic fluctuations around nuclei (van der Waals interaction), and specifically for metals, the interaction between the delocalized (free) electrons and the atomic cores.

At the beginning of the simulation, the coordinates and the velocities of individual atoms are initialized. Then, the forces and the accelerations for each atom are obtained. Newton's equations can be integrated numerically over time to update the velocities and positions of the atoms to yield the motion of the system. This can be done by writing

$$\boldsymbol{v}_i\left(t+\delta t\right) = \boldsymbol{v}_i\left(t\right) + \boldsymbol{a}_i\left(t\right)\delta t \tag{2.5}$$

$$\boldsymbol{r}_i\left(t+\delta t\right) = \boldsymbol{r}_i\left(t\right) + \boldsymbol{v}_i\left(t\right)\delta t + \frac{1}{2}\boldsymbol{a}_i\left(t\right)\delta t^2. \tag{2.6}$$

However, the update rules in Equation (2.5) assume atoms have constant accelerations during each time step. Although a straightforward way of solving for the equations of motion, these update rules do not yield self-consistent results. That is, the accelerations calculated from the position functions $\boldsymbol{r}_i$ obtained by this way generally do not match those obtained by solving Newton's equations directly. Consequently, a significant error accumulates over time.

To satisfy self-consistency, alternative algorithms are used to integrate Equation (2.3). One commonly used algorithm is the velocity-Verlet algorithm [109], a modified version of the basic Verlet algorithm [110], that explicitly updates velocities together

with the positions. The implementation steps of the velocity-Verlet algorithms are

$$\begin{aligned}
\boldsymbol{v}_i\left(t+\frac{1}{2}\delta t\right) &= \boldsymbol{v}_i(t)+\frac{1}{2}\boldsymbol{a}_i(t)\,\delta t \\
\boldsymbol{r}_i(t+\delta t) &= \boldsymbol{r}_i(t)+\boldsymbol{v}_i\left(t+\frac{1}{2}\delta t\right) \\
\boldsymbol{F}_i(t+\delta t) &= -\nabla_i U\left(\boldsymbol{r}^N(t+\delta t)\right) \\
\boldsymbol{v}_i(t+\delta t) &= \boldsymbol{v}_i\left(t+\frac{1}{2}\delta t\right)+\frac{1}{2}\boldsymbol{a}_i(t+\delta t)\,\delta t.
\end{aligned} \tag{2.7}$$

After determining the update rules, what remains to be found is a suitable interatomic potential that accurately predicts material properties.

2.2.1. The Embedded Atom Model Potentials

In the embedded atom method, the interatomic potential has two parts. The first part represents the pairwise interactions between atoms and the second part represents the energy required to embed an atom in an electron gas of density ρ_i. The interatomic potential, then, takes the form:

$$U[\boldsymbol{r}] = \frac{1}{2}\sum_i \sum_{j\neq i} \Phi[r_{ij}] + \sum_i V_i[\rho_i]\,. \tag{2.8}$$

The term r_{ij} is the distance between atom i and atom j. The name of the method comes from the $V[\rho_i]$ term, which is called the embedding function. The argument ρ_i of the embedding function is the local electronic density and is itself a function of the distance between the atom i and the other atoms. This can be expressed in compact form as $\rho_i = \sum_{j\neq i} f[r_{ij}]$. The term $f[r_{ij}]$ is the electron density around the position of the atom i due to the neighbor atom j. An atom does not interact with its own free electrons and the total density sum is over only the neighbor atoms. The embedded atom method potential that is used in this study is developed by Wu et al. [111]. The parameters for this potential were calibrated by comparing mechanical (e.g. Peierls stresses, stacking fault energies and Young's modulus) and structural (e.g. lattice constants) property predictions obtained with the potential to the predictions of quantum mechanical simulations and experimental observations.

The Large-scale Atomic/Molecular Massively Parallel Simulator (LAMMPS) is used to carry out the MD simulations. LAMMPS uses the velocity-Verlet algorithm for time integration. The system temperature and the pressure boundary conditions are maintained by employing a Nose-Hoover style thermostat/barostat [112] which thermodynamically corresponds to an NPT ensemble. Further details of the molecular dynamics method and the embedded atom model are given in standard texts on molecular simulation [108, 113, 114].

2.3. Classical Nucleation Theory

Classical nucleation theory [115] studies the formation of a new phase inside a medium where the medium is metastable with respect to the formation of this new phase. A variety of physical phenomena including deformation twinning can be treated within the classical nucleation theory framework. Here, for convenience, the newly formed phase is called the cluster or the embryo and the medium is called the matrix. In the classical model, for nucleation of a stable cluster, first a small part of the matrix is converted to the new phase. Then, this new embryo must survive the barrier forces to nucleation and grow into a larger and stable cluster that will not convert back to the matrix phase. The total potential energy of the cluster can be decomposed into a bulk energy term and an interfacial energy term such that

$$\Delta E_{total} = \Delta E_{bulk} + \Delta E_{interfacial}. \tag{2.9}$$

The interfacial area term is, in general, positive since the formation of new interfaces induces excess energies. Hence, the interfacial term constitutes a barrier to formation. If the bulk energy term is negative, then it constitutes a driving force for the nucleation event. When the embryo is small, the interfacial energies are relatively larger. As the embryo grows, the volumetric term starts to dominate. For an embryo to grow and reach a size which ensures its stability, it has to overcome an energy barrier. The critical cluster size and the energy barrier are found from the condition

$$\frac{\mathrm{d}\Delta E_{total}}{\mathrm{d}N} = 0, \tag{2.10}$$

where N is a size parameter (e.g. number of atoms, geometric dimensions, etc.) of the cluster. Equation (2.10) defines the critical point (i.e. N_c and ΔE_c) of the nucleating embryo. The condition for nucleation is visualized in Figure 2.6 where the total energy is plotted as a function of N. A real potential energy plot is typically more complex than the one sketched in Figure 2.6 since the size of the cluster is generally determined by more than one parameter. In such cases, the critical size and the energy barrier determined the location of at the saddle point of the potential energy hypersurface.

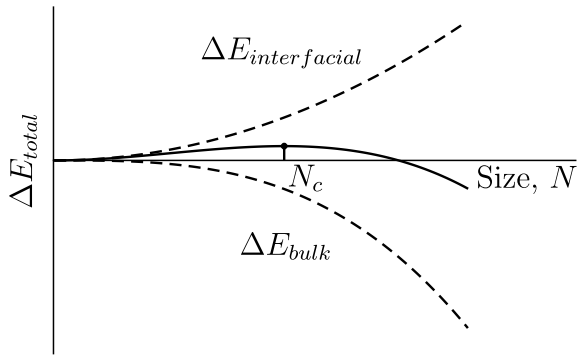

Figure 2.6. ΔE_{bulk}, $\Delta E_{interfacial}$ and ΔE_{total} curves are plotted vs. the cluster size N. ΔE_{total} is shown by the solid curve.

In the deformation twinning problem, the cluster is formed by a homogeneous transformation strain ε_{ij}^{p} applied to a region of the matrix. In such events, misfit strains arise between the matrix and the cluster due to geometric incompatibilities. The elastic strain energy due to the misfit strains constitutes the bulk energy term. If there are no externally applied stresses, the elastic strain energy due to the cluster is positive. Thus, it acts as a barrier to formation. However, if a far-field stress is applied to the entire system, the interaction between the applied stress and the misfit strains might relieve the excess energy introduced by the cluster. The applied stress, in that case, acts as the driving force. The mathematical form of the bulk energy term in the case of elastic strain energy will be discussed in Section 2.4.

The interfacial term can take different forms. For instance, the interface between the cluster and the matrix may or may not be isotropic. In fact, the boundaries of

deformation twins found in Mg are faceted with anisotropic energies. Thus, in the case of twin boundaries in Mg, the interfacial energy term is the sum of all the contributions of these different facets and can be written in general form as

$$\Delta E_{interfacial} = \sum_i \gamma_i A_i. \tag{2.11}$$

Here A_i and γ_i are the area and energy per unit area of the ith interface. In a homogeneous nucleation event, the embryo nucleates inside a homogeneous medium in the absence of a specific site. Then, the newly formed interfaces all contribute excess energy and γ_i will be positive for all interfaces. However, in the case of heterogeneous nucleation on grain boundaries, some part of the preexisting grain boundary transforms into a new boundary between the embryo and the neighboring grain. If the original boundary has a larger excess energy per unit area than the transformed boundary, the interfacial energy sum is reduced by this transformation. In that case, the transformation of the grain boundary acts as a driving force.

One commonly used parameter in nucleation kinetics is the time required to see a stable nucleus, called the incubation time. The incubation time is related to non-steady state nucleation in thermally activated processes [115]. Accordingly, the incubation time for the nucleation of an embryo that consists of N_c atoms is approximately

$$\tau = \frac{12 k_B T N_c^2}{2\beta \Delta E_c}, \tag{2.12}$$

where k_B is the Boltzmann's constant, T is the medium temperature and β is the jump frequency of the atoms into and out of the cluster. The number of atoms contained in a cluster can be estimated from the relation

$$N_c \approx \frac{V_{cluster}}{V_{atom}}, \tag{2.13}$$

where V_{atom} is approximated by the volume of the Voronoi cell around the atom. A crude estimation for the atomic jumping frequency can be given by the Debye frequency of the solid. The Debye frequency of the solid is related to the Debye temperature through the relation

$$\beta = \frac{k_B T_D}{\hbar}, \tag{2.14}$$

where T_D is the Debye temperature and $\hbar$ is the reduced Planck constant. In this thesis, the incubation time is used only as a crude parameter to estimate the size of a twin nucleus observable in a fixed experimental time. A more rigorous discussion of this parameter is given elsewhere [115].

2.4. Eshelby Inhomogeneity Model for Deformation Twins

Eshelby's inclusion theory concerns the elastic fields that arise due to the presence of an inclusion or inhomogeneity inside a surrounding medium. An inclusion has the same elastic constants as the surrounding medium whereas an inhomogeneity has different elastic constants to the medium. The elastic fields arise due to the geometric incompatibilities between the surrounding medium and the inclusion (or inhomogeneity). Deformation twins fit this description since mechanical twinning entails a region of the matrix undergoing a localized finite strain. The transformed region will have a different shape than the original and give rise to incompatibility strains. Eshelby [116] conceived this problem with a thought experiment consisting of cut and paste steps as visualized in Figure 2.7. First, a region is cut from the surrounding medium. Then, a transformation strain ε_{ij}^{p} is applied to this cut piece, freely changing its shape. Since this piece is free of constraints at this point, no elastic field arise. Then, a certain traction $\boldsymbol{T}$ is applied to the surface of this piece to transform it back to its original shape. Next, without releasing the tractions, this piece is put back into the original location in the medium. Finally, the tractions are released to let the medium and the inhomogeneity interact.

For the inclusion case, the fundamental problem reduces to finding the strain fields $\varepsilon_{ij}(\boldsymbol{x})$ that arise at each point in the structure after the inclusion is allowed to interact with the medium. Taking the inclusion as a collection of points and denoting the eigenstrain as $\boldsymbol{\varepsilon}^{*}$ to follow the notation of Mura [117], the total strain field $\boldsymbol{\varepsilon}$ becomes

$$\varepsilon_{ij}(\boldsymbol{x}) = -\frac{1}{2}\int_{V} C_{mnkl}\varepsilon_{kl}^{*}(\boldsymbol{x'})\left\{G_{im,nj}(\boldsymbol{x}-\boldsymbol{x'}) + G_{jm,ni}(\boldsymbol{x}-\boldsymbol{x'})\right\}d^{3}\boldsymbol{x'}. \tag{2.15}$$

The integrand on the right hand side represents the sum of the displacements at point ($\boldsymbol{x}$) of due to point forces at point ($\boldsymbol{x'}$). The individual contribution of each point force is calculated using the Green's function of the medium and the integral is over the volume of the inclusion. If the eigenstrain is constant over the inclusion, then Equation (2.15) can be written as

$$\varepsilon_{ij}\left(\boldsymbol{x}\right) = -\frac{\varepsilon^*_{kl}}{2}\int\limits_V C_{mnkl}\ \{G_{im,nj}\left(\boldsymbol{x}-\boldsymbol{x'}\right) + G_{jm,ni}\left(\boldsymbol{x}-\boldsymbol{x'}\right)\} d^3\boldsymbol{x'}. \tag{2.16}$$

The integral in Equation 2.16 can be expressed with a fourth order tensor, reducing Equation (2.16) to

$$\varepsilon_{ij} = S_{ijkl}\varepsilon^*_{kl}. \tag{2.17}$$

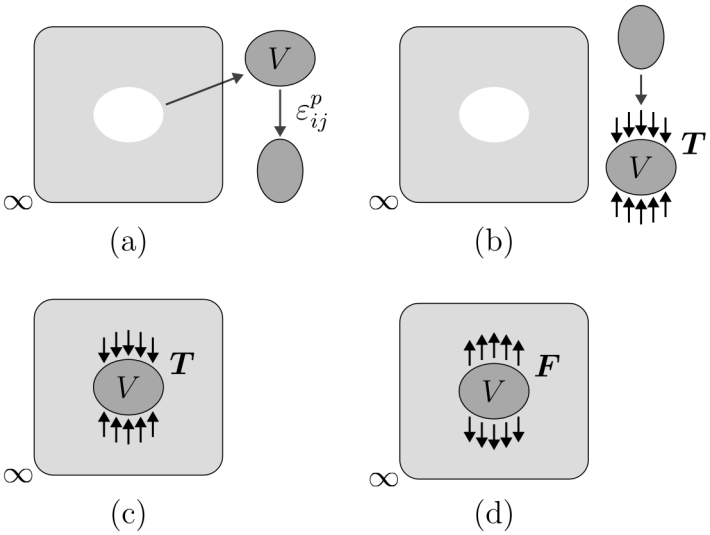

Figure 2.7. The steps of the Eshelby thought experiment. (a) A region (e.g. a twinned region) is cut from the medium and an eigenstrain is applied. (b) The shape of the region is restored to its original state by applying a traction on its surface. (c) The region is placed back in the medium without releasing the tractions. (d) The region and the medium are allowed to interact.

S_{ijkl} is called the Eshelby tensor and it relates the eigenstrain applied over the inclusion to the total strain field. Eshelby showed that the Eshelby tensor and the total strain field inside an ellipsoidal inclusion (or inhomogeneity) are uniform and that the Eshelby tensor is a function of the shape of the inhomogeneity and the elastic constants

of the medium alone. This profound result allows for robust analytical solutions for the elastic fields of crystal defects, specially including deformation twins.

For inhomogeneities, the inclusion problem is extended to an equivalent inclusion problem where the effect of the inhomogeneity is modeled with a combined eigenstrain $\varepsilon_{ij}^{**} = \varepsilon_{ij}^{p} + \varepsilon_{ij}^{*}$. ε_{ij}^{p} is the transformation strain applied to the inhomogeneity and ε_{ij}^{*} is the effect of replacing the inhomogeneity material with the medium material. Eshelby's equivalent inclusion theory [116, 117] allows the total stress and strain to be found as $\sigma_{ij} = \left(C_{ijkl}S_{klmn} - C_{ijmn}\right)\varepsilon_{mn}^{**}$ and $\varepsilon_{ij} = S_{ijkl}\varepsilon_{kl}^{**}$. ε_{ij}^{**} is related to ε_{ij}^{p} by:

$$[(C_{ijkl}^{*} - C_{ijkl})S_{klmn} + C_{ijmn}]\varepsilon_{mn}^{**} = C_{ijkl}^{*}\varepsilon_{kl}^{p}, \tag{2.18}$$

where C_{ijkl}^{*} and C_{ijkl} are the stiffness tensors of the twin and the surrounding medium, respectively.

A very useful outcome of Eshelby's solution is that, in the presence of an applied far-field stress, the total potential energy E_{inh} due to a transformed inhomogeneity embedded inside a medium can be expressed as

$$E_{\text{inh}} = \Delta W = -\frac{1}{2}\int \sigma_{ij}^{0}\epsilon_{ij}^{*}dV - \frac{1}{2}\int \sigma_{ij}\epsilon_{ij}^{p}dV - \int \sigma_{ij}^{0}\epsilon_{ij}^{p}dV, \tag{2.19}$$

where the integrals are over the twinned volume and Equation (2.19) involves only the interior elastic fields and the known applied far-field stress. Equation (2.19) accounts for the elastic strain energy of the twin as well as the interaction between the applied far-field stress and the twin transformation strain. For deformation twinning in Mg, ε_{ij}^{p} is constant and Equation (2.19) reduces to:

$$E_{\text{inh}} = -\frac{1}{2}V\sigma_{ij}^{0}\varepsilon_{ij}^{*} - V\sigma_{ij}^{0}\varepsilon_{ij}^{p} - \frac{1}{2}V\sigma_{ij}\varepsilon_{ij}^{p}, \tag{2.20}$$

where V is the volume of the inhomogeneity, σ_{ij} is the total stress inside the inhomogeneity, σ_{ij}^{0} is the applied stress and the Einstein summation convention is followed. Hence, calculation of the non-uniform exterior elastic fields is not required for an energy-based analysis. In the absence of applied far-field stress, the energy of a deformation twin reduces further to

$$E_{\text{inh}} = -\frac{1}{2}V\sigma_{ij}\varepsilon_{ij}^{p}. \tag{2.21}$$

In this study, the twins observed in the simulation are treated as inhomogeneities, although Liu et al. [94] have shown that the effect of modeling Mg as elastically isotropic and the twins as inclusions is minimal. This is attributed to Mg being almost elastically isotropic [118]. Finally, the shapes of the twins observed in the MD simulations in Ch. 3 are close to elliptic cylinders and the Eshelby's tensor for the elliptic cylinder geometry is given in Appendix A.

3. ENERGETIC CONTRIBUTIONS TO TWINNING IN MAGNESIUM

This chapter has been adapted from the following publication:

Kapan, E., S. Alkan, C. C. Aydıner and J. K. Mason, "Energetic Contributions to Deformation Twinning in Magnesium", *Modelling and Simulation in Materials Science and Engineering*, Vol. 31, No. 7 p. 075002 [119].

There continues to be increasing interest in using Mg as a lightweight structural material due to its high strength-to-density ratio and other desirable properties [120]. Mg and Mg alloys are hexagonal close packed (hcp) and accommodate plastic strains by a combination of deformation twinning and slip at room temperature [4, 99, 121–123]. Twinning involves a localized finite strain accompanied by a reorientation of the parent crystal, and twinning-dominated plastic deformation causes tension-compression asymmetry and plastic anisotropy at the macroscale due to the unipolar nature of twinning [122]. Sample-scale shear banding has been observed [20–22] in Mg AZ31 samples with rolling textures loaded in compression perpendicular to the plate normal, triggering the $\{10\bar{1}2\}$ tension twin mechanism [4]. Deformation heterogeneity patterns observed in wrought Mg alloys are also observed to be a function of loading sense [10,124,125]. These aspects of the twin nucleation process need to be understood more deeply before rigorous models of Mg plasticity can be developed.

Heterogeneous nucleation is preferred for twin embryos in crystalline Mg due to pronounced energy barrier effects [72, 92, 126], with grain boundaries being preferable nucleation sites in polycrystals [76, 127]. Twin nucleation at a grain boundary entails formation of new interfaces (twin boundaries) emanating from the pre-existing grain boundary and is assisted by a set of coordinated dislocation reactions. The complexity of this process makes predicting possible twin nucleation sites a formidable task and requires accurate energetic descriptions for the twin-related structures. The purpose

of this work is to explore the various energetic contributions to heterogeneous twin nucleation in Mg, laying the groundwork for models to eventually predict heterogeneous twin nucleation sites.

Crystal plasticity (CP) approaches have been popular to model deformation twinning at the continuum scale for more than two decades [44, 128]. Phenomenological formulations usually introduce a twinned volume fraction of material within a pseudo-slip formulation [34]. While these approaches are reasonably successful at reproducing the far-field twinning response, they are of limited utility when predicting the nucleation site or the twin embryo morphology [44, 128]. The alternative is to explicitly resolve individual twins as in recently-developed schemes where twin nucleation is modeled as a defect-dissociation reaction, [40, 41] sometimes within phase-field simulations [129–131]. However, these approaches do not yet consistently incorporate the twin/grain boundary energetics which may play a significant role in heterogeneous twin nucleation.

The possibility of there being other significant energetic contributions that are not included in existing models indicates that there is a need for more detailed atomistic information about the twinning event. This encouraged the recent characterization of the defect content of twin-parent grain interfaces (i.e., basal-prismatic/prismatic-basal (BP/PB) boundaries and coherent twin boundaries (CTB)) by transmission electron microscopy (TEM) and the subsequent development of atomic-scale models for twin nucleation and growth mechanisms [54, 83, 85, 132, 133]. These models suggest that the glide of twinning dislocations along a CTB drives the growth of a twin, while the CTB-BP junctions serve as dislocation nucleation and annihilation sites [75]. MD calculations by El Kadiri et al. [16] explain the profuse activity of the $\{10\bar{1}2\}$ tension twinning mode in Mg by the ability of the twin boundary to absorb basal dislocations without a loss of mobility [16]. Liu et al. [51], using a combination of TEM experiments and MD simulations, characterized CTB and BP/PB facets and showed that the interaction of dislocations with these boundaries plays an important role in twinning energetics; this is reinforced by subsequent work [53–56, 134].

While investigations into the atomic structure of twin interfaces generally focus on pre-existing twin domains, this study is instead concerned with heterogeneous twin nucleation. As a starting point, electron backscatter diffraction indicates that the misorientation between neighboring grains as well as the grain boundary length are significant factors affecting the statistics of twin nucleation and propagation [87, 127, 135]. Wang et al. [8] and Beyerlein et al. [127] explored the relationship between GB misorientation and twinning using MD simulations of twins nucleating from a set of symmetrically-tilted grain boundaries (STGBs). The simulations initiated twin nucleation reactions by introducing basal dislocation pile-ups at the STGBs [8, 76, 127, 136], and informed a stochastic twin nucleation model where the likelihood of twin nucleation increases with decreasing misorientation angle [127]. Barrett et al. [85, 137] subsequently investigated the twin nucleation mechanism on a pre-existing BP boundary and identified the relevance of asymmetrically-tilted grain boundaries (ATGB), defect transformation from CTB to BP facets, and the mobility of BP facets to twin nucleation. Giri et al. [138] used the nudged elastic band method to measure the energy barrier of twin embryo formation on a bi-crystal STGB with a specific misorientation and macroscopic stress condition. Though all of these studies consider the energetics of twin nucleation, they initiate twin nucleation by intentionally imposing defects or assuming specific reaction pathways.

Alternatively, simulating twin nucleation in a polycrystalline microstructure with MD has been done in a limited number of studies before [139–141], but a deep understanding of twin nucleation in these conditions has yet to be established. Additional studies of spontaneous twin nucleation driven by external loading, without prior assumptions about the nature of the mechanism, could therefore be valuable.

This study uses an MD simulation described in Section 3.1 to follow the energetic evolution of twin embryos nucleating from ATGBs in a honeycomb polycrystalline structure (Figure 3.1). Section 3.2 provides an overview of the twinning events observed during the MD simulation, identifies the twin-related structures, and measures the overall energetic contribution of the twins to the simulation's potential energy. The

relative energetic contributions of line, surface and volumetric terms to the twin nucleation process are evaluated in Section 3.3, and the stress field around the twin nucleus is estimated using the Eshelby formalism.

A micromechanical model for the twin formation energy is developed in the same section, with the energy contribution arising from the change in character of the prior GB found to be significant. The I_1 stacking faults that form inside the twin and the associated defect structures that bound them are also found to possibly make significant energy contributions, amplifying the conclusions of recent experimental [142, 143] and numerical studies [71] that emphasized the role of I_1 stacking faults inside tension twins. These results suggest that both of these contributions should be included in any comprehensive energy-based twin nucleation model going forward.

3.1. Methods

The MD simulations used the LAMMPS code [144] with a modified embedded-atom method interatomic potential for Mg [111]. The potential was specifically designed to reproduce defect and interface structures and has been widely employed to simulate plastic deformation in pure Mg and Mg-based alloys.

A honeycomb polycrystal with four columnar grains was generated in a simulation box with periodic boundary conditions in all directions (shown in Figure 3.1) using the Voronoi tessellation algorithm implemented by the Atomsk software [145] . The z-axis of the simulation box coincided with the $[\overline{1}\overline{1}20]$ directions of the grains, and together they constituted a $[11\overline{2}0]$-textured system. The central grain (indicated by G1) was oriented to align its c-axis with the global x-axis. Grains 2, 3 and 4 (indicated by G2, G3 and G4) were misoriented with respect to G1 by 15°, 25° and 48° rotations about the z-axis, with examples of the global and grain coordinate systems and the tilt angle ϕ sketched in Figure 3.1.

Given this geometry, a compressive load along the global y-axis would both impose a tensile strain along the c-axis of G1 and result in minimal dislocation activity on the basal plane for which the Schmid factor is zero. Such conditions strongly favor $\{10\bar{1}2\}$ tension twinning in G1, with more dislocation activity expected in the misoriented neighboring grains. The simulation cell geometry and periodic boundary conditions effectively constrained all dislocation lines to be aligned along the global z-axis and the planes of shear of any twins to be parallel with the xy plane.

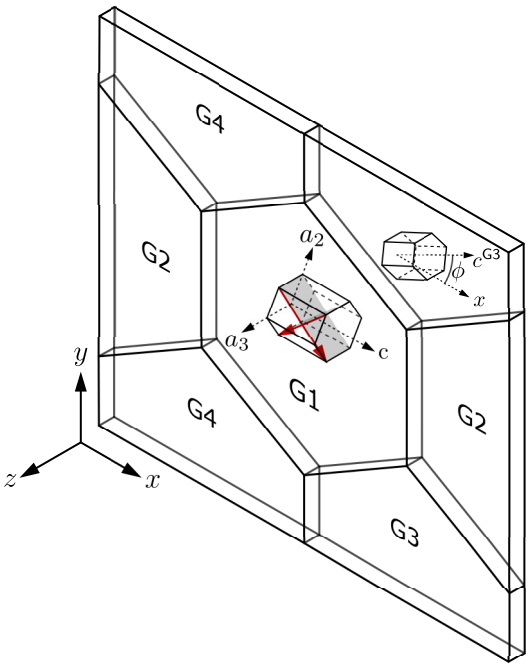

Figure 3.1. Schematic of the periodic quasi-2D simulation cell with honeycomb grains. The $[\bar{1}\bar{1}20]$ crystal axes of all grains are aligned with the global z-axis. Grains 2, 3 and 4 are tilted by a rotation of ϕ about the global z-axis. The $(\bar{1}102)$ and $(1\bar{1}02)$ planes associated with the activated $\{10\bar{1}2\}$ tension twin system are highlighted in the central unit cell.

After initializing the system, the potential energy was minimized using a conjugate gradient method. The initial minimization was followed by an equilibration step at 0 MPa and 300 K for 50 ps using a Nose-Hoover style isothermal-isobaric (NPT) thermostat [112] to relax any remaining high energy GB structures. Each component of the average stress tensor was below 6 MPa after the equilibration step, well below

the reported critical stresses for similar structures [139]. The structure was then compressed in the y-direction at a constant engineering strain rate of -2×10^8 s^{-1} for 160 ps. 41 load points (LPs) were taken at 1 ps intervals between 104 ps and 145 ps after the start of compression (corresponding to far-field strains ε^0_{yy} of -0.0208 and -0.0286) and will be referred to as LP0 to LP40 below.

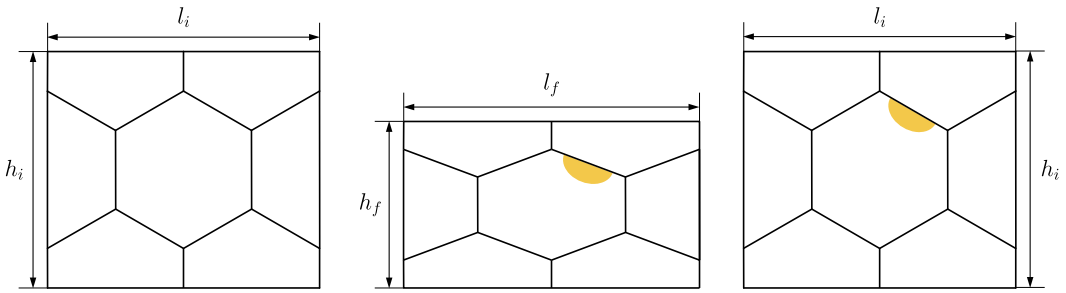

Figure 3.2. A sketch of (a) the simulation cell after initial equilibration, (b) the deformed simulation cell with a twin in G1 (the deformation is exaggerated), (c) the simulation cell after the removal of far-field strain. The initial dimensions l_i, h_i, t_i are 692 Å, 600 Å and 25.6 Å respectively.

After completing the simulation, each LP was instantaneously quenched to 0 K by setting the atomic momenta to zero and minimizing the potential energy. The far-field strains on each LP were then removed by restoring the simulation box dimensions to those of the undeformed state and mapping the atomic coordinates with the corresponding affine transformation. This was followed by a final energy minimization to relax any local elastic strains introduced by the affine transformation. The second minimization did not noticeably affect the shape or extent of the twin nucleus, despite the untwinned structure having a lower potential energy in the undeformed state. The resulting atomic data (potential energies, atomic coordinates, etc.) were stored for each of the selected LPs for subsequent analysis. A graphical description of this loading/remapping sequence is given in Figure 3.2.

The purpose of the minimizations and affine transformation was to remove any thermal fluctuations and far-field elastic strains which would complicate the calculation

of the potential energy of the developing twin nucleus. More specifically, the intention was to examine the potential energy of the twin nucleus in a fixed reference state where the far-field strain vanished, conceptually resembling Eshelby's thought experiment of embedding an inhomogeneity into an infinite medium.

Post-processing and visualization of the atomic data was done using the Open Visualization Tool (OVITO) [146] complemented with custom Python scripts. The OVITO implementations of Polyhedral Template Matching (PTM) and the Dislocation Extraction Algorithm (DXA) were used to identify crystal structures, interfaces and dislocations. A grain segmentation scheme based on local (per atom) orientations returned by PTM was implemented to automate the identification of atoms belonging to the twin.

3.2. Results

The stages of the most significant twinning event that occurred during the MD simulation are shown in Figure 3.3, with Figs. 3.3a and b showing the entire simulation cell at the beginning and end of the event. The LP0 structure in Figure 3.3c contained two twin embryos on the G1-G3 boundary, with one (upper left, indicated by a red arrow) nucleating around LP0 and the other (bottom right) nucleating during the initial equilibration step before any external straining. By LP9 in Figure 3.3d, a third twin nucleus indicated by a red arrow appeared between the two preexisting nuclei. Figure 3.3e shows the coalescence of N1 and N2 at LP19, and all of the nuclei coalesced into a single large twin by LP24 in Figure 3.3f. The twin had extended along the entire prior GB and continued to expand into the interior of G1 by LP32 in Figure 3.3g. The twin at the final loading point LP40 in Figure 3.3h developed new PB and CTB facets on the lower right, and overcame the G1-G2-G3 triple junction barrier to extend along the G1-G2 boundary. The final twin is clearly well-developed and stable, and would continue to expand into the interior of the grain had the simulation continued. The purpose here is to investigate the initial stages of twin formation though, so the later stages of intragranular twin growth will not be considered. Instead, the analysis

that follows will be limited to the twin formation stages on the G1-G3 grain boundary visible in Figure 3.3.

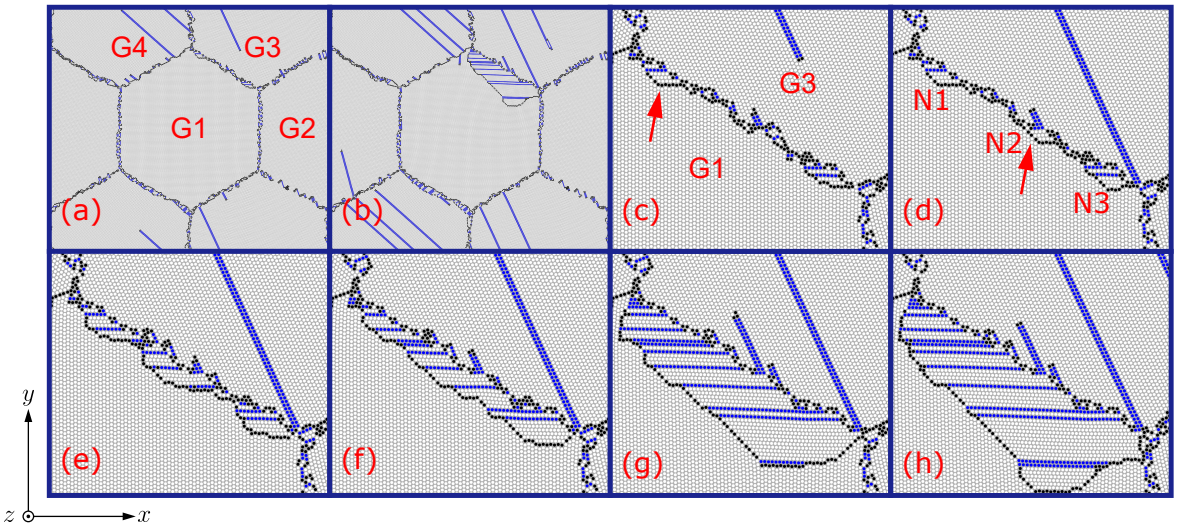

Figure 3.3. (a,b) Snapshots of the simulation box at LP0 ($\varepsilon^0_{yy} = -0.0208$) and LP40 ($\varepsilon^0_{yy} = -0.0286$). (c-h) Snapshots of the twinned G1-G3 boundary at LP0, LP9, LP19, LP24, LP32 and LP40 ($t = 104$, 113, 123, 128, 136 and 144 ps respectively). White and blue indicate atoms in hcp and fcc environments, whereas black denotes a disordered structure on an interface.

3.2.1. Energetic Analysis

The change in potential energy ΔPE of the load points with respect to LP0 are calculated and plotted in Figure 3.4. The potential energy generally increases from LP0 to LP40 with the accumulation of plastic strain and various defect structures. The three curves in the figure correspond to the potential energies of the load points after each of the three post-processing operations described in Section 3.1. The dashed blue curve shows the change in potential energy after the first energy minimization, i.e., after instantaneously quenching the structure to 0 K. The dashed red curve shows the decrease in the potential energy after removing the far-field strain by means of the affine transformation. The solid black curve is obtained after the second energy minimization relaxes the local elastic strains introduced by remapping the atomic coordinates. That is, the solid black curve should reflect only the effect of introducing the twin and other

defects into the system's reference configuration. The advantage of this construction is that the far-field stress that drives the nucleation of the twin is removed, allowing the energetic model for twin nucleation to be simplified by dropping one of the terms. This also allows the remaining elastic strain energy to more readily be approximated by Eshelby's solution to the generalized inhomogeneity problem [116].

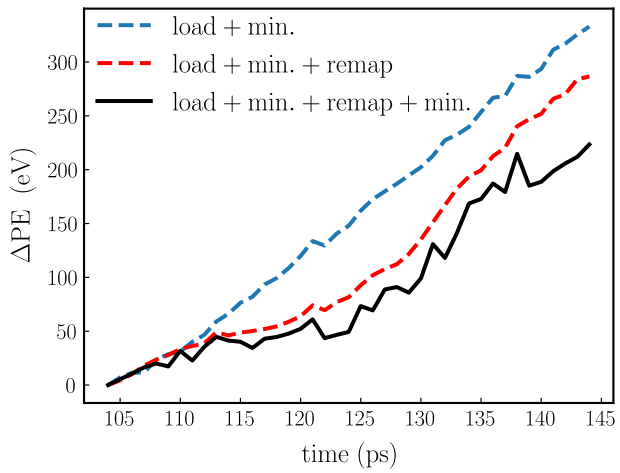

Figure 3.4. The change in potential energy of the simulation cell relative to values at LP0 ($t = 104$ ps) (i) after the first energy minimization, (ii) after removal of the far-field strain ε^0, (iii) after the second energy minimization.

While the energetic analysis of the developing twin nucleus could be performed using the black curve in Figure 3.4, accounting for the energetic contributions of the various defect structures that develop in G2, G3 and G4 would introduce complications. For example, the $1/3\langle\bar{1}100\rangle$ Shockley partials in G3 and G4 in Figure 3.3 contribute dislocation core and elastic strain energies, and the trailing I_2-type stacking faults (visible in blue in Figure 3.3a-b) have a surface energy that would need to be removed from the overall potential energy change. Restricting the analysis to only the region occupied by the twin at LP40 would instead introduce complications from the compatibility strain field surrounding the twin gradually extending outside of the region as the nucleus develops. The significance of this effect can be seen in Figure 3.5 where the solid green curve shows the potential energy change of G1 (the union of green and yellow regions in the inset) and the dashed yellow curve shows only that of the region

occupied by the twin at LP40 (the yellow region in the inset). The potential energy changes are similar when the twin nuclei are small compared to the yellow region, but the yellow curve falls below the green curve as the twin size becomes comparable to that of the yellow region and more of the energy stored in the strain field external to the twin is excluded. The simplest option seems to be to consider the potential energy change of G1, with a comparison of Figs. 3.3a and 3.3b showing that G1 has limited defect activity elsewhere in the grain during the relevant time interval (likely owing to the vanishing of the Schmid factor for basal slip). The potential energy change inside G1 is therefore ascribed to the developing twin nucleus, and the green curve in Figure 3.5 is selected as the basis for the following analysis. It should be noted though that the green curve is not the overall potential energy of the twin nucleus since the energy contribution of the compatibility strains that develop in the neighboring G3 is neglected. The neglected energy will be accounted for by an approximation introduced in Section 3.3.3 below.

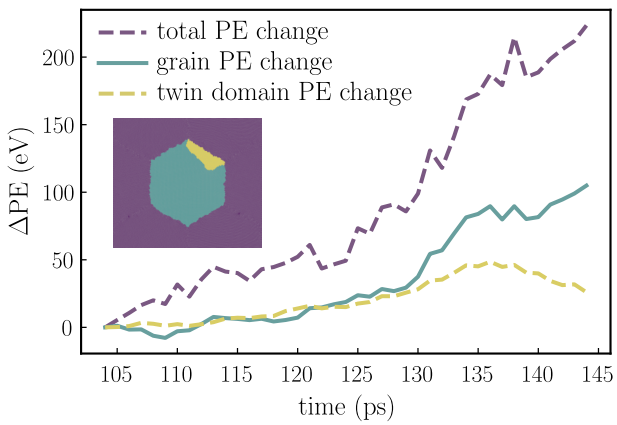

Figure 3.5. The change in potential energy relative to the values at LP0 ($t = 104$ ps) of (i) the entire simulation cell, (ii) G1, and (iii) the region occupied by the twin at 140 ps.

3.2.2. $\{10\bar{1}2\}$ Twin Related Structures

The general structure of the twin observed in the MD simulation is shown in Figure 3.6 with the characteristic structures at LP28 highlighted and labeled. The cross-

section of a $\{10\bar{1}2\}$ twin viewed along the $[\bar{1}\bar{1}20]$ axis usually has a stepped boundary consisting of CTB and PB/BP facets. A CTB facet is one where the plane of the boundary coincides with the twin plane (indicated in the following by K_1), and is the $\{10\bar{1}2\}$ plane for a $\{10\bar{1}2\}$ twin. The orientation of the K_1 plane is indicated with red lines inside the representative hcp unit cells sketched for the matrix and twin in Figure 3.6. There is a negligible misalignment of ~2° between the actual CTB and the expected CTB orientations, likely due to local atomic strains. A PB/BP facet is one where the prismatic/basal plane of the matrix adjoins the basal/prismatic plane of the twin. In Figure 3.6, the facets labeled PB are those where the basal planes of the twin coincide with the prismatic planes of the matrix. Both the basal-prismatic and prismatic-basal boundaries will be indicated by PB in the following since the two have essentially identical characters. Recent studies suggest that the growth of a twin into the interior of the matrix is facilitated by the formation of a terrace (a disconnection pair) on the CTB [75] and subsequent glide of the disconnections along the CTB [71], thereby involving an interplay of CTB and PB boundaries.

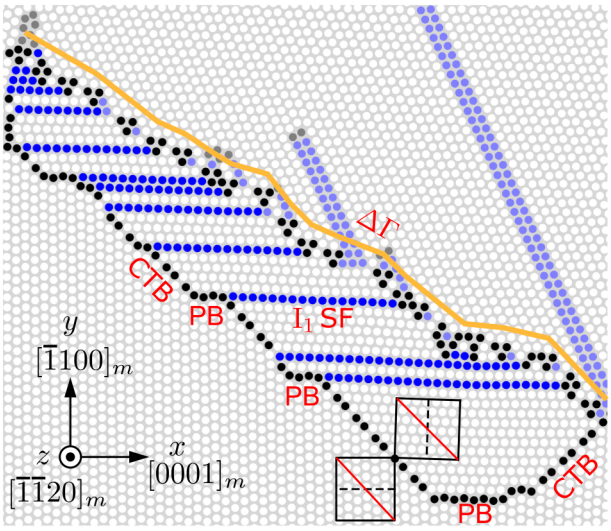

Figure 3.6. Interfacial energy contributions associated with a $\{10\bar{1}2\}$ twin include those for coherent twin boundaries (CTBs), basal-prismatic boundaries (PBs), I_1 stacking faults (I_1 SFs) inside the twin, and the energy change $\Delta\Gamma$ of the prior GB. White and blue indicate atoms in hcp and fcc environments, whereas black denotes a disordered structure on an interface.

As a brief aside, the historical assumption has been that a twin embryo is initially bounded predominantly or even entirely by CTB facets [147]. However, recent HREM studies [83] have established that a twin embryo boundary can have a significant proportion of BP/PB facets. The ratio of total CTB facet area to total PB facet area in the MD simulation is plotted in Figure 3.7 for all load points LP0 to LP36, and is consistent with roughly half of the twin boundary being PB facets.

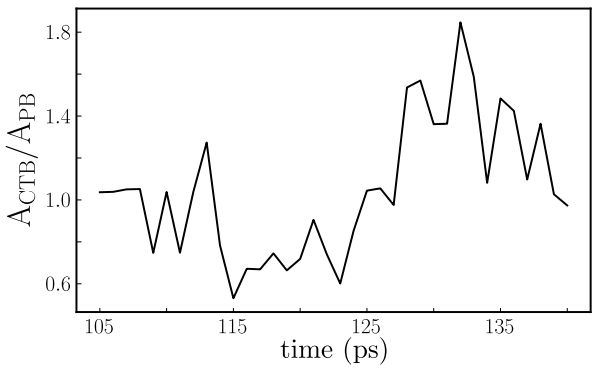

Figure 3.7. The ratio of total CTB facet area to total PB facet area on the boundary of the twin nucleus for all load points LP0 to LP36.

Two other structures are labeled in Figure 3.6 in addition to the twin-matrix boundaries. The first are I_1 stacking faults (SFs) that change the stacking order of the basal planes to $AB\underline{A}CA$ (or equivalently $BA\underline{B}CB$); recent high resolution electron microscopy (HREM) studies have verified the presence of such SFs inside $\{10\bar{1}2\}$ twins [142, 143, 148]. The SFs usually extend from the twin boundary on one side to the GB on the other, with the intersection with the twin boundary frequently occurring at a junction between CTB and PB facets. The second structure is the traced boundary between the twin and the neighboring G3 that is labeled with a $\Delta\Gamma$. The GB initially between G1 and G3 effectively decomposed with the emission of the twin boundary, leaving behind a GB of changed character. Similar decomposition reactions can be seen to have been initiated on several other GBs (e.g., the boundaries between G1 and G2) in Figure 3.3a.

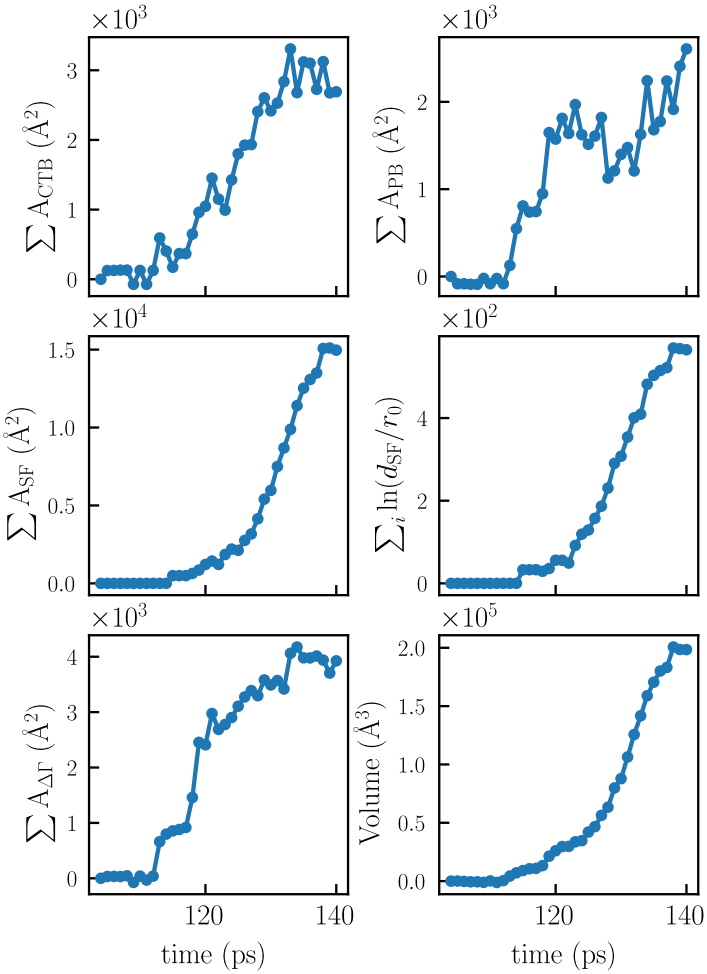

Figure 3.8. Magnitudes of the various $\{10\bar{1}2\}$ twin related structures. In addition to changes in the CTB, PB, SF and $\Delta\Gamma$ areas, changes to the twin nucleus volume and the sum of the natural logarithms of stacking fault lengths (normalized by the twice the lattice constant of Mg) are reported.

The magnitudes of the various twin related structures are quantified by direct measurement and reported in Figure 3.8. Lengths are calculated as the sum of the lengths of line segments connecting adjacent atomic columns, and areas are calculated by multiplying a length by the depth of the simulation cell. Volumes are calculated as the sum of the volumes of the Voronoi cells around the relevant atoms. These quantities are used extensively for the analysis in Section 3.3 below.

3.3. Analysis and Discussion

The total potential energy of the twin nucleus is likely composed of contributions from the interfaces, the defect substructure, and a strain energy arising from the transformation strain. Although a precise partitioning of the twin potential energy between these contributions is almost intractable due to the number of unknowns and the difficulty of mapping concepts like an interface or a dislocation core to a specific set of atoms, a micromechanical model for the potential energy can nevertheless be developed by applying certain simplifications. As a starting point, a model is proposed for the change in the potential energy of G1 that includes terms for the twin boundary facets, the stacking faults, the prior grain boundary, and a term that is proportional to the twin volume:

$$\begin{aligned} \Delta E_{\mathrm{G1}} = \gamma_{\mathrm{CTB}} A_{\mathrm{CTB}} + \gamma_{\mathrm{PB}} A_{\mathrm{PB}} + \gamma_{\mathrm{SF}} A_{\mathrm{SF}} \\ + \gamma_{\Delta\Gamma} A_{\Delta\Gamma} + C_{\mathrm{V}} V. \end{aligned} \tag{3.1}$$

The CTB, PB and SF contributions are modeled as the products of the equilibrium excess surface energies (148, 164 and 11 $\mathrm{mJ/m^2}$ respectively [111, 149, 150]) and the corresponding interfacial areas.

The $\Delta\Gamma$ term accounts for the change in the surface energy of the GB initially between G1 and G3 with the emission of the twin boundary. $\gamma_{\Delta\Gamma}$ will be estimated by a linear regression analysis in Section 3.3.1, with the resulting value verified by a molecular statics calculation in Section 3.3.5.

The volumetric term $C_{\mathrm{V}}V$ will initially be assumed in Secs. 3.3.2 and 3.3.3 to be proportional to the elastic strain energy introduced by applying a transformation strain to an elliptic cylinder inhomogeneity in an infinite elastic medium.

This model will eventually be found to be unable to account for the potential energy of the twin nucleus, resulting in a revision of the model in Section 3.3.4 to include the possible elastic interactions of disconnections in the twin boundary and

the prior GB (Figure 3.8 shows that any potential energy stored in these interactions would be nearly proportional to the twin volume). The final analysis strongly suggests that the energy change of the prior GB, and perhaps the elastic interactions of the disconnections, contribute significantly to the potential energy of the nucleating twin.

3.3.1. Regression Analysis

The CTB, PB, and SF terms in Equation (3.1) are determined by the equilibrium excess surface energies reported in the literature and the interfacial areas in Figure 3.8. This leaves $\gamma_{\Delta\Gamma}$ and C_{V} as the only unknown quantities in Equation (3.1), and since they appear linearly in the equation, they can be estimated by linear least squares using the potential energies of G1 at each of the N loading points.

Explicitly, the linear regression problem takes the following form:

$$\begin{bmatrix} A_{\Delta\Gamma}^{\mathrm{LP}0} & V^{\mathrm{LP}0} \\ \vdots & \vdots \\ A_{\Delta\Gamma}^{\mathrm{LP}N} & V^{\mathrm{LP}N} \end{bmatrix} \begin{bmatrix} \gamma_{\Delta\Gamma} \\ C_{\mathrm{V}} \end{bmatrix} = \begin{bmatrix} \Delta E_{\mathrm{G1}}^{0} - \sum_i \gamma_i^0 A_i^0 \\ \vdots \\ \Delta E_{\mathrm{G1}}^{N} - \sum_i \gamma_i^N A_i^N \end{bmatrix}, \tag{3.2}$$

where the sum on the right hand side includes the CTB, PB and SF interfaces. Solving this gives -0.140 ± 0.011 J/m^2 and 52.6 ± 3.31 MJ/m^3 for the parameters $\gamma_{\Delta\Gamma}$ and C_{V}, respectively.

The results of the regression analysis are plotted in Figure 3.9 alongside the MD measurements for comparison. It is significant that the $\Delta E_{\Delta\Gamma}$ curve shows a significant decrease in the energy of the G1-G3 GB as the twin propagates along the GB.

Note also that C_{V} here includes the energetic contributions from all possible sources that scale with the twin volume, including but not restricted to the elastic strain energy. The elastic strain energy will be estimated by the Eshelby formalism in the following sections, allowing an evaluation of whether this is sufficient to explain the ΔE_{V} curve in Figure 3.9.

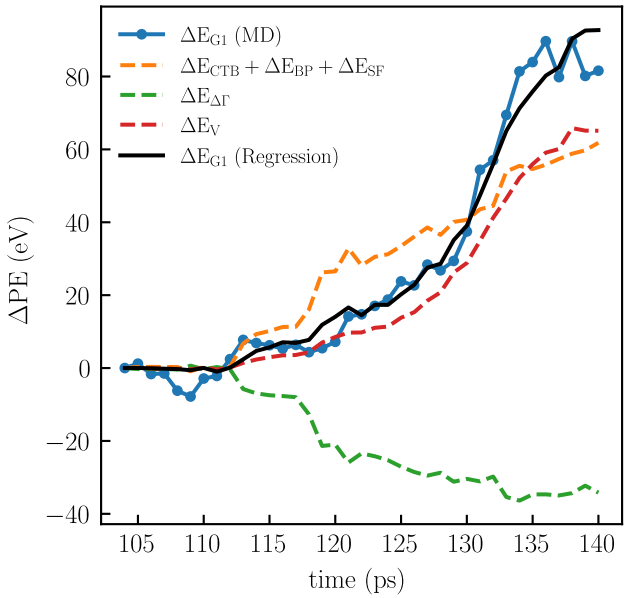

Figure 3.9. Energetic contributions of the various terms involved in the regression analysis in Equation (3.2) are plotted with dashed lines. The change in the G1 potential energy during the MD simulation (blue curve) is used as a measure of the change in the twin potential energy. The black curve is the sum of the dashed curves and is the least squares fit to the blue curve.

3.3.2. Principal Component Analysis

The calculation of the elastic strain energy associated with a twin in the Eshelby inhomogeneity theory requires that the geometric parameters of the twinned regions be known to first obtain the Eshelby tensor. A twin is modeled as an elliptic cylinder since twins are frequently observed to have elliptic morphologies during the initial twinning stages [137]. At each load point, the atoms that belong to each of the twinned regions are identified, and the dimensions of the elliptic cylinder that contains the associated point cloud are found using principal component analysis. Specifically, the atomic coordinates matrix is defined as

$$\mathbf{A} = \begin{bmatrix} x_1 & y_1 \\ x_2 & y_2 \\ \vdots & \vdots \end{bmatrix}. \tag{3.3}$$

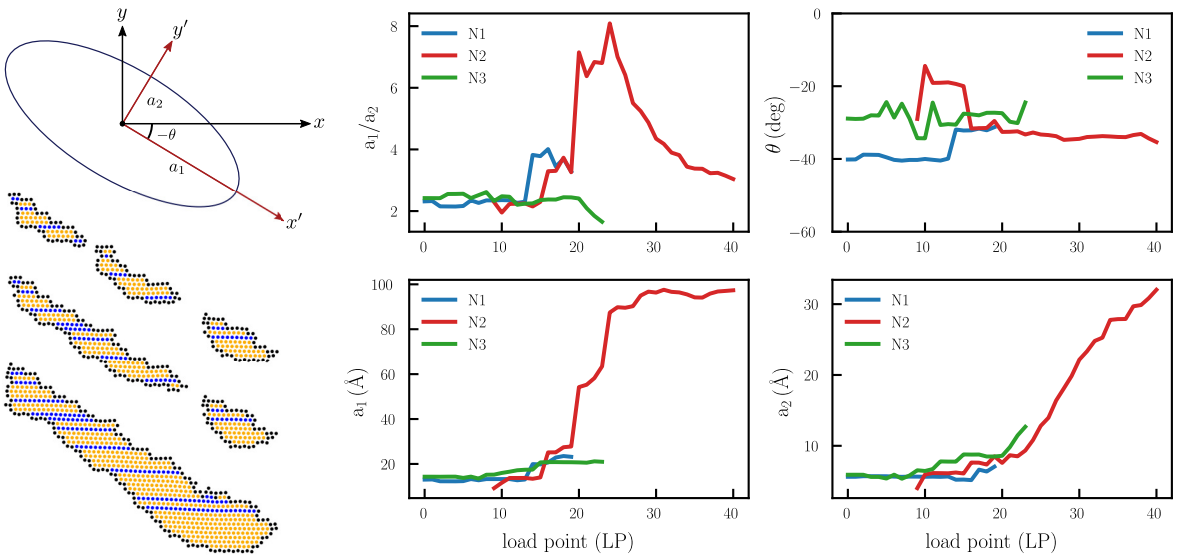

Figure 3.10. The evolution of the the geometric properties of the ellipses fitted to the twin nuclei. All twin nuclei coalesce by LP24 and only the geometric data for the ellipse fitted to N2 is reported for subsequent load points.

The directions of the semi-major and semi-minor axes are taken to be the directions of the first and second eigenvectors of $\mathbf{A}^T\mathbf{A}$. If a_1' and a_2' are the square roots of the corresponding eigenvalues, then the major and minor radii a_1 and a_2 are defined by the conditions that $a_1/a_2 = a_1'/a_2'$ and the volume of the resulting elliptical cylinder is identical to the twin volume.

The orientation of the elliptic cylinder with respect to the simulation cell's coordinate system is expressed as the angle θ between the semi-major axis and the x-axis. The major and minor radii, the aspect ratios and the orientations of the twins obtained from the principle component analysis are all reported in Figure 3.10. Notice that the twin nuclei start to coalesce with increased loading (as portrayed by the isolated snapshots of the nuclei at different LP's given below the reference ellipse) and all three of the twin nuclei coalesce by LP24, leaving only the geometric parameters of the second nucleus in the plots beyond this loading point. The geometric quantities a_1, a_2 and θ are used below to model the twins as elastic inhomogeneities and estimate the associated elastic strain energies following Eshelby formalism.

3.3.3. Elastic Field Model

Eshelby showed that the total strain energy E_{inh} in an infinite elastic medium due to a transformed inhomogeneity embedded inside the medium is equal to

$$E_{\text{inh}} = -\frac{1}{2} V \sigma_{ij} \varepsilon^{p}_{ij}, \tag{3.4}$$

where σ_{ij} is the total stress inside the inhomogeneity, ε^{p}_{ij} is the eigenstrain associated with the twin transformation, and the Einstein summation convention is followed. E_{inh} is the total strain energy in the entire medium and can be decomposed into two parts, namely, the elastic strain energies stored in the interior and exterior of the inhomogeneity [151]:

$$\begin{aligned} E_{\text{inh}} &= E_{\text{int}} + E_{\text{ext}} \\ &= \frac{1}{2} V \sigma_{ij} (\varepsilon_{ij} - \varepsilon^{p}_{ij}) - \frac{1}{2} V \sigma_{ij} \varepsilon_{ij}, \end{aligned} \tag{3.5}$$

where ε_{ij} and $\varepsilon_{ij} - \varepsilon^{p}_{ij}$ are the total and elastic strains in the inhomogeneity, respectively. Eshelby's equivalent inclusion theory [116, 117] allows the total stress and strain to be found as $\sigma_{ij} = \left(C_{ijkl} S_{klmn} - C_{ijmn}\right) \varepsilon^{**}_{mn}$ and $\varepsilon_{ij} = S_{ijkl} \varepsilon^{**}_{kl}$ where S_{ijkl} is the Eshelby tensor and ε^{**}_{kl} is the equivalent eigenstrain tensor in the equivalent inclusion problem. ε^{**}_{ij} is related to ε^{p}_{ij} by:

$$[(C^{*}_{ijkl} - C_{ijkl}) S_{klmn} + C_{ijmn}] \varepsilon^{**}_{mn} = C^{*}_{ijkl} \varepsilon^{p}_{kl}, \tag{3.6}$$

where C^{*}_{ijkl} and C_{ijkl} are the stiffness tensors of the twin and the surrounding medium, respectively.

The eigenstrain tensor $\boldsymbol{\varepsilon}^{p}$ associated with the $\{10\bar{1}2\}$ Mg twin in the simulation cell coordinate system is:

$$\boldsymbol{\varepsilon}^{p} = \begin{bmatrix} 0.065 & 0 & 0 \\ 0 & -0.065 & 0 \\ 0 & 0 & 0 \end{bmatrix}. \tag{3.7}$$

The medium is modeled as having the same isotropic elastic response as polycrystalline Mg [118, 152]; this is not regarded as a severe approximation since the medium is composed of magnesium single crystals with multiple orientations, each of which is

nearly elastically isotropic. The equivalent inclusion (i.e., the twin) is instead modeled as being transversely isotropic in the basal plane, consistent with hcp crystal symmetry. The elastic properties for both the medium and the twins are reported in Table 3.1. The components of the Eshelby tensor for an elliptic cylinder are functions of the major and minor radii a_1 and a_2 and the elastic constants of the medium, and these functions have been tabulated by Mura [117].

Table 3.1. Elastic constants of the medium and the twin in standard orientations. The components of the stiffness tensor of the medium can be obtained from the isotropic elastic properties.

Medium (GPa)		Twin (GPa)	
E	45	C^*_{1111}	63.5
ν	0.28	C^*_{1122}	25.9
μ	17.6	C^*_{1133}	21.7
		C^*_{3333}	66.5
		C^*_{1313}	18.4

After solving for the elastic fields associated with the inhomogeneity, E_{inh} for the Eshelby solution can be compared to the volumetric energy term obtained from the regression results. However, the energy change of G1 is used as the objective for the regression analysis in Equation (3.2), whereas the Eshelby solution accounts for the total elastic strain energy stored in the entire medium. This makes Equation (3.5) not directly comparable to the regression results. The elastic energy stored in G1 is instead modeled as the sum of the elastic strain energy stored on the interior and half that stored on the exterior of the inhomogeneity:

$$\begin{aligned} E_{\text{inh,G1}} &= E_{\text{int}} + E_{\text{ext,G1}} \\ &\approx \frac{1}{2} V \sigma_{ij} (\varepsilon_{ij} - \varepsilon^p_{ij}) - \frac{1}{4} V \sigma_{ij} \varepsilon_{ij}. \end{aligned} \tag{3.8}$$

The prediction of Equation (3.8) is compared to the volumetric energy term obtained from the regression analysis in Figure 3.11, where the volumetric term obtained from the regression analysis is seen to be significantly higher than that predicted by the

Eshelby solution. The discrepancy does not necessarily suggest a failure of the energy model in Equation (3.1) or of the approximations involved in our application of the Eshelby solution, but rather that there could be an additional energy contribution that scales with the volume of the twin and is distinct from the elastic strain energy in the Eshelby solution.

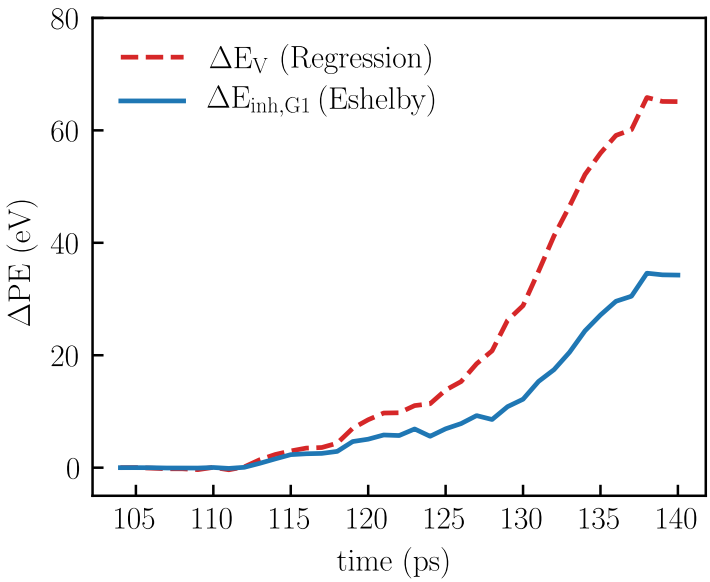

Figure 3.11. The volumetric part of the twin energy (ΔE_V, dashed red curve) as approximated by the regression analysis (Equation (3.2)) is compared with the elastic strain energy predicted $E_{inh,G1}$ by the Eshelby solution (Equation (3.8), solid blue curve).

3.3.4. Revising the Micromechanical Model

A closer examination of the defect substructure inside the twin in Figure 3.12 reveals that the point where a stacking fault intersects the twin boundary almost invariably coincides with a corner of a BP or PB facet. Such stacking faults have also been observed experimentally in $\{10\bar{1}2\}$ twins [142,143], and their possible origins and the character of their bounding defects have been studied in detail [67, 71, 153]. The bounding defect in the twin boundary is specifically known to have disconnection character; the Burgers vectors and the step heights of the disconnections in Figure 3.12

are given in the conventional notation $\mathbf{b}_{\pm\mu/\pm\kappa}$ used in interfacial defect theory [154]. The sign of the subscripts μ and κ indicate a step "up" or "down" with respect to the parent crystal, and their magnitudes signify the height of the step. The other bounding defect of each stacking fault is embedded in the GB and has a Burgers vector determined by the initial defect content of the GB and the dissociation reaction that produces the associated SF.

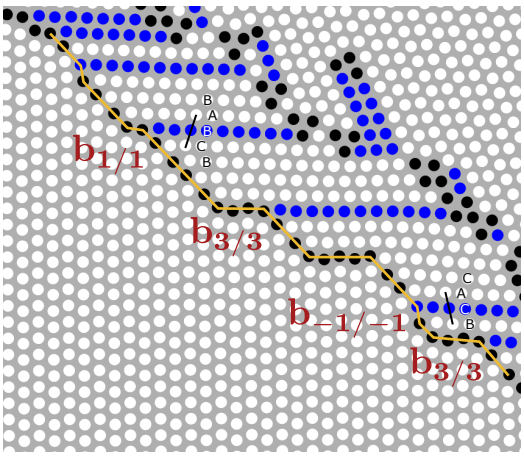

Figure 3.12. I_1 basal stacking faults inside the $\{10\bar{1}2\}$ twin. Each SF is bounded by a defect pair that anchors the SF to the twin boundary on the left and the grain boundary on the right. Defects in the TB have disconnection Burgers vectors denoted by $\mathbf{b}_{\pm\mu/\pm\kappa}$, corresponding to two different changes in the stacking sequence. The stacking changes associated with $\mathbf{b}_{1/1}$ and $\mathbf{b}_{-1/-1}$ steps are identified.

The model in Equation (3.1) presumably includes the self-energies of the defects at the ends of the stacking faults in the effective energies of the bounding interfaces, but does not include the interaction energies of those defects. The conservation of Burgers vector content implies that the defects at either end of a stacking fault have equal and opposite Burgers vectors and hence exert attractive forces per unit length on one another.

By analogy with the work required to separate a full dislocation into a pair of Shockley partials, the work required to separate the defects at either end of the ith stacking fault is modeled as being proportional to $\ln(r_i/r_0)$ where r_i is the length of

the stacking fault, $r_0 = 2a$ is a reference length scale, and a is the lattice constant of Mg. Including this interaction term in the model for the change of the potential energy of G1 gives:

$$\begin{aligned}\Delta E_{\mathrm{G1}} = \gamma_{\mathrm{CTB}} A_{\mathrm{CTB}} + \gamma_{\mathrm{PB}} A_{\mathrm{PB}} + \gamma_{\mathrm{SF}} A_{\mathrm{SF}} \\ + E_{\mathrm{inh,G1}} + \gamma_{\Delta\Gamma} A_{\Delta\Gamma} + Kt \sum_i \ln(r_i/r_0),\end{aligned} \tag{3.9}$$

where t is the thickness of the simulation cell and the prefactor K has units of eV/Å. While the SFs inside the twins are bounded by different defect pairs with different Burgers vectors and the prefactors associated with each defect pair should therefore be different, K is an average prefactor that accounts for the total interaction energy between the arrays of defects on the TB and on the GB.

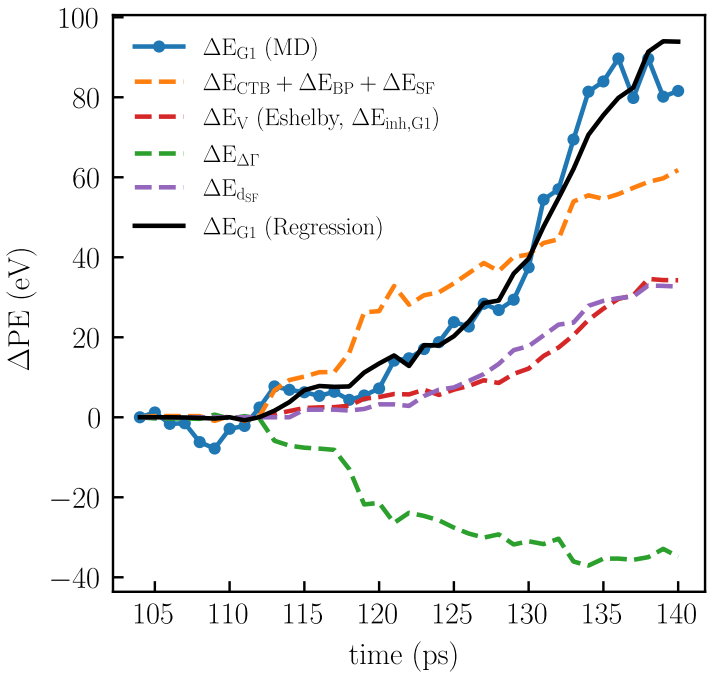

Figure 3.13. Energetic contributions of the various terms involved in the second regression analysis in Equation (3.10) are plotted with dashed lines. The change in the G1 potential energy during the MD simulation (blue curve) is used as a measure of the change in twin potential energy. The black curve is the sum of the dashed curves and is the least squares fit to the blue curve.

With this modification, the linear regression problem to find the two unknown parameters in Equation (3.9) becomes:

$$\begin{bmatrix} A_{\Delta\Gamma}^{\mathrm{LP}0} & t\sum_i \ln\left(\frac{r_i^0}{r_0}\right) \\ \vdots & \vdots \\ A_{\Delta\Gamma}^{\mathrm{LP}N} & t\sum_i \ln\left(\frac{r_i^N}{r_0}\right) \end{bmatrix} \begin{bmatrix} \gamma_{\Delta\Gamma} \\ K \end{bmatrix} = \vec{y}, \tag{3.10}$$

where $\vec{y}$ is the column vector whose jth entry is given by $\Delta E_{\mathrm{G1}}^j - \sum_i \gamma_i^j A_i^j - E_{\mathrm{inh,G1}}^j$. Solving this gives -0.142 ± 0.013 J/m^2 and 0.0578 ± 0.0077 eV/Å for the parameters $\gamma_{\Delta\Gamma}$ and K, respectively. The value for $\gamma_{\Delta\Gamma}$ is nearly the same as that obtained in Section 3.3.1 using Equation (3.2), and will be discussed in more detail in Section 3.3.5. The results of the regression analysis are plotted in Figure 3.13 alongside the MD measurements for comparison.

The estimated value of K should be comparable to the prefactor for a single pair of typical defects that bound an I_1 SF segment inside $\{10\bar{1}2\}$ twins. The Burgers vectors of the PB disconnections on the twin boundary have varying magnitudes between $0.150a$ and $0.350a$ [71]. The $\langle c+a \rangle$ dislocations embedded in the grain boundary on the other end of the stacking fault have Burgers vectors of length $\sim a$. For the average case, the prefactor of the interaction energy between a dislocations with Burgers vector lengths of $b_1 = 0.250a$ and $b_2 = a$ respectively is roughly

$$K \propto \frac{\mu b_1 b_2}{2\pi} = 0.0409 \text{ eV/Å}, \tag{3.11}$$

which is sufficiently close to the least square estimate for the latter to be reasonable. The only remaining term in Equation (3.9) that has not been shown to be physically reasonable is the $\gamma_{\Delta\Gamma} A_{\Delta\Gamma}$, and this is considered in detail below.

3.3.5. Grain Boundary Decomposition

As discussed in the introduction, one of the main unresolved questions relating to hcp twinning is the prediction of the twin nucleation site at grain boundaries in polycrystals. Many studies focus on the connection between the grain boundary misorientation and the tendency for twins to nucleate on the loaded grain boundary; the

grain boundary inclination and the transformed grain boundary character are generally not considered to be relevant. However, our results suggest that both of these could be important factors. Figure 3.14a-b compares the G1-G3 grain boundaries before and after the nucleation of the twin. Figure 3.14a shows that at LP0 the GB contains the prior G1-G3 boundary with ATGB character in the middle and transformed segments on both ends. By comparison, the fully transformed GB shown in Figure 3.14b has a nearly STGB character where the basal planes of the twin and G3 intersect the GB at similar angles. However, the transformed GB has a corrugated topography with a structure that deviates from an STGB particularly at the intersections with stacking faults, suggesting the presence of defects with Burgers vector content there.

The transformation of the GB from a high-energy ATGB into a low-energy STGB during twinning significantly reduces the overall interfacial energy cost of nucleating the twin, as can be seen by comparing the green and orange curves in Figure 3.13. Both the first and second regression analyses suggest a reduction in the grain boundary energy of roughly $\gamma_{\Delta\Gamma} \approx -0.0088$ eV/Å^2 (-0.140 J/m^2). Two auxiliary MD simulations were conducted to verify that this value of $\gamma_{\Delta\Gamma}$ is plausible. First, a copy of the original simulation cell containing the original G1-G3 GB was generated and relaxed by energy minimization. Second, G1 was reoriented to the $\{10\bar{1}2\}$ twinned orientation while keeping the other grain orientations fixed, and the resulting simulation cell was equilibrated. Representative slices of material around the GB regions were taken from both simulations and are shown in Figure 3.14c-d. The grain boundary energies of the G1-G3 and twinned G1-G3 boundaries are computed as

$$\gamma = \frac{E_{\text{tot}} - NE_{\text{eq}}}{A_{\text{GB}}}, \tag{3.12}$$

where E_{tot} is the total potential energy of the slice, N is the number of atoms in the slice, E_{eq} is the equilibrium per atom potential energy for bulk Mg, and A_{GB} is the area of the grain boundary. The slices contain 16 520 and 1388 atoms respectively, and a value of $E_{\text{eq}} = -1.51$ eV/atom as measured by an MD simulation of a single crystal is consistent with the literature [111]. The computed energies for the initial (original) and final (twinned) grain boundaries are $\gamma_i = 0.0345$ eV/Å^2 (0.553 J/m^2) and $\gamma_f = 0.077$ eV/Å^2 (0.124 J/m^2) respectively, where γ_f is expected to be low since

the transformed boundary is nearly a $\{10\bar{1}3\}$ twin boundary with the neighboring grains symmetrically tilted by 31.99° with respect to the $[\bar{1}\bar{1}20]$ axis. This is shown in Figure 3.14d where the angles the basal planes of both grains make with the grain boundary are very close to 32°, with slight unequal deviations on each side. Wang and Beyerlein [155] calculated the energy of this boundary to be 0.105 J/m^2, close to γ_f found for the present structure.

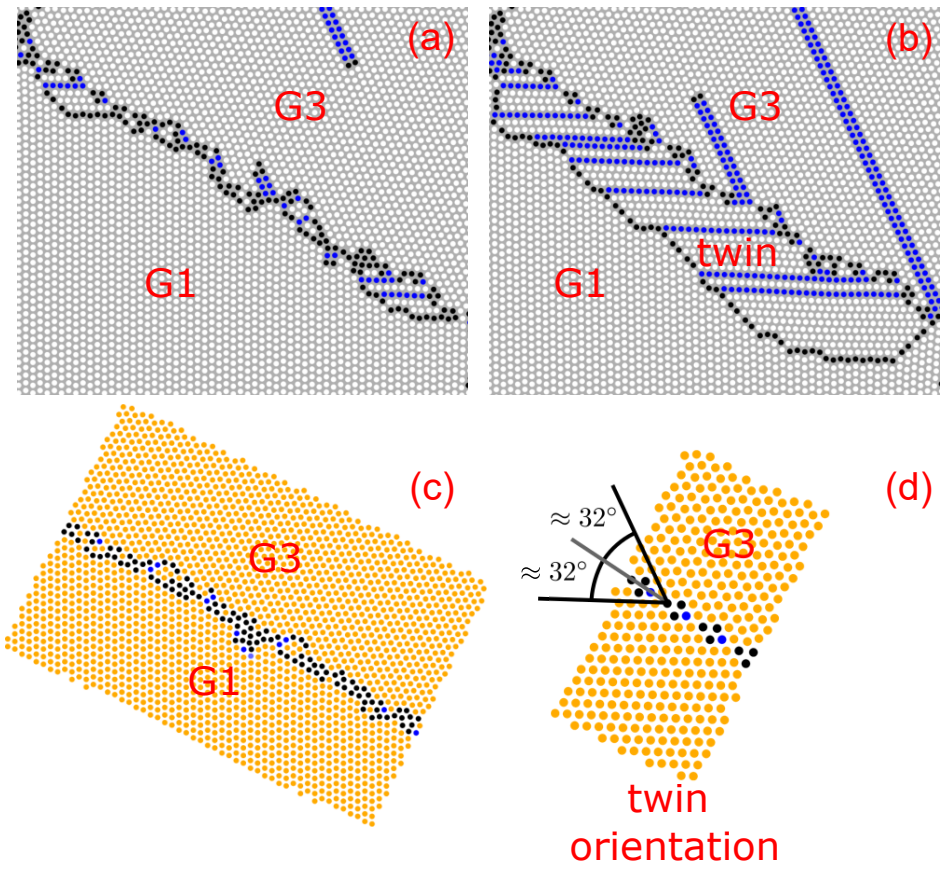

Figure 3.14. (a) Snapshot of the ATGB grain boundary between G1 and G3 at LP0. (b) The propagation of the twin transforms the twin-G3 GB into a (nearly) STGB. (c) The partially-relaxed ATGB structure between G1-G3 prior to equilibration. (d) A fully relaxed GB with identical grain boundary character to the twin-G3 GB. White/orange, blue and black indicate hcp, fcc and border atoms.

Using these results, the reduction in the grain boundary energy could be as much as $\gamma_f - \gamma_i = -0.429$ J/m^2, three times higher than the value $\gamma_{\Delta\Gamma}$ estimated from the regression analyses. Since the actual transformation that takes place upon twinning

does not yield a fully relaxed and equilibrated grain boundary (Figure 3.14d) but rather a corrugated one with excess stresses (Figure 3.14b), this is interpreted as indicating that the value of $\gamma_{\Delta\Gamma}$ from the regression analysis is physically reasonable.

It is significant that the original ATGB shown in Figure 3.14c partially dissociated into the transformed GB shown in Figure 3.14d when equilibrated at higher temperatures for longer durations, even in the absence of external strain. This reaffirms that the change in the character of the prior GB can significantly reduce the energy barrier to twin nucleation. This is consistent with the conclusions of Barrett et al. [85, 137] who investigated twinning along a BP boundary in a bicrystal and found that the defect structure of ATGBs could be an important factor. The implication is that the inclination of the prior grain boundary could be a possible controlling variable as well. As evidence of this, unstable twins nucleated only on the upper of the two G1-G3 GBs (G1 shares two boundaries with G3 of the same misorientation in Figure 3.1) for which the inclination is such that $\{10\bar{1}2\}$ twinning yields an STGB. Thus, the upper G1-G3 GB is a more favorable twinning location. Our conclusion is that the change in the character of the prior GB should be considered in future twinning models.

3.4. Conclusions

Molecular dynamics simulations were performed to investigate the process by which a twin nucleates from a grain boundary in a columnar polycrystal. A far-field strain was applied to drive the twin nucleation, but the potential energy of the twin as a function of time was measured with respect to the unstrained configuration as a consistent point of reference. A model for the potential energy of the nucleating and growing twin was proposed that involves various geometric variables, parameters taken from the literature, and several unknown quantities estimated by linear regression. Our main conclusions based on this energy model are as follows:

(i) The potential energy of the twin could not be satisfactorily modeled as a sum of contributions from only the twin boundary (comprised of coherent twin and

basal-prismatic/prismatic-basal facets), stacking faults inside the twin, and elastic strain energy as estimated using the Eshelby inhomogeneity theory. That is, the potential energy of the nucleating twin necessarily involved more quantities (see below) than just those associated with visibly growing geometric structures in Figure 3.3.

(ii) The reduction in grain boundary energy associated with the change in grain boundary character upon twinning can be substantial, and even to the point of offsetting the energy cost of the twin boundary and stacking fault creation. Specifically for the observed twinning event, the prior boundary decomposed from a high-energy ATGB structure into a low energy STGB structure with a $\{10\bar{1}3\}$ twin boundary relation. The other boundary in the periodic simulation cell with the same misorientation relation but a different inclination was inactive, indicating that grain boundary inclination is potentially a significant variable. Overall, this suggests that the change in grain boundary character during twinning could be a critical consideration when predicting twin nucleation sites.

(iii) The elastic strain energy estimated using the Eshelby inhomogenity theory does not seem to be sufficient to explain the part of the twin potential energy that is approximately proportional to the volume of the twin. It is proposed that the stacking faults inside the twin are bounded by line defects with Burgers vector content embedded in the twin boundary and the prior grain boundary. As part of the extrinsic defect content of the boundaries, these line defects can have interacting elastic strain fields. While not conclusively establishing the existence of such interactions, including an energy contribution proportional to the logarithm of the normalized separation of the proposed line defects is sufficient for the Eshelby inhomogeneity theory to account for the part of the potential energy that is proportional to the twin volume.

These conclusions are envisioned as part of an ongoing effort by the community to establish a micromechanical model which can be used to predict the activation energies and critical geometries of nucleating twins as functions of microstructure variables and far-field loading conditions. It is true that both the molecular dynamics simulations

and the energy model for twin formation developed here are restricted to thin films of $[\overline{1}\overline{1}20]$ fiber textured Mg, but we expect that the insights derived through the use of this simplified geometry will hold more generally, and particularly when the energy model is eventually extended to three dimensions.

4. A MICROMECHANICAL MODEL FOR TWIN NUCLEATION

In this chapter, we extend our energetic analysis of $\{10\bar{1}2\}$ twins in Mg by the application of the classical nucleation theory (CNT) to the twin nucleation problem. According to the CNT, the nucleation energy barrier is the saddle point of the potential energy hypersurface. The twin geometry that corresponds to the saddle point gives the critical size and shape of the nucleated twin. Our aim is to construct, from a few given parameters, a model for the potential energy surface for $\{10\bar{1}2\}$ twin configurations nucleating on a grain boundary.

As a starting point, in Chapter 3, we developed a model for the potential energy of a nucleating twin in Equation (3.9). This expression can be rewritten to include the entire long-range elastic strain energy (i.e. the Eshelby term) rather than only considering the energy component in the parent grain that was relevant in Section 3.3.3:

$$\begin{aligned} \Delta E = {} & \gamma_{\mathrm{CTB}} A_{\mathrm{CTB}} + \gamma_{\mathrm{PB}} A_{\mathrm{PB}} + \gamma_{\mathrm{SF}} A_{\mathrm{SF}} \\ & + E_{\mathrm{inh}} + \gamma_{\Delta\Gamma} A_{\Delta\Gamma} + Kt \sum_i \ln(r_i/r_0) \end{aligned} \tag{4.1}$$

Equation (4.1) describes the potential energy of a twin as a function of several material parameters (γ_{CTB}, γ_{PB}, γ_{SF}, K, etc.) and geometric variables that define the twin configuration (A_{CTB}, A_{PB}, A_{SF}, etc.). The missing material parameters $\gamma_{\Delta\Gamma}$ and K are assumed to be equal to the values derived from a series of least square fits of the potential energy curve of the $\{10\bar{1}2\}$ twin formed in the MD simulation analyzed in Ch. 3. The remaining requirement to be able to model the potential energy of a twin is a geometric model that accurately predicts the geometric variables in Equation (4.1). For this, we propose a simple geometric model where the shape of the twin is idealized as an elliptic cylinder. The boundary of the cylinder is decomposed into CTB, PB and $\Delta\Gamma$ segments. Likewise, the average lengths of stacking fault segments as well as the number of stacking faults per twin are estimated. The calculated geometric quantities

are substituted into the model to construct the potential energy surface for a nucleating twin. Then, minimum energy pathways (MEP)s and the corresponding saddle points of the potential surface are found using a string relaxation method. We start with the discussion of the geometric model.

4.1. The Geometric Model

4.1.1. Twin Boundary Decomposition

The general scheme of the twin boundary decomposition model is sketched in Figure 4.1. Figure 4.1a shows a twin with an elliptic cylinder geometry nucleated on a grain boundary between grains G1 and G3 (named identically to the MD case to ease the comparison). The cylinder axis of the twin is aligned with the page normal. The depicted twin, although growing into G1, is bulging into G3 as was observed in the MD snapshots. However, to retain physicality for larger twins by avoiding excessively curved boundaries, the bulging distance δ_{max} is limited to a maximum of 1-2 lattice constants in the model. To further simplify the problem, the twin nucleus is assumed to grow either along or perpendicular to the grain boundary. The main motivation for this simplification is to ease the identification of the initial twin growth direction when the twin is still in the embryo stage. The radii along and perpendicular to the grain boundary are a and b respectively as indicated in Figure 4.1b. For fixed lattice orientations of G1 and G3, as well as fixed grain boundary inclination (θ in Figure 4.1d), the perimeter of the ellipse (i.e. the boundary area) and the geometric variables A_{CTB}, A_{PB}, A_{SF} and V reduce to functions of a and b only.

The twin boundary is comprised of two major parts. First, the boundary segment indicated by the blue-colored arc $Q'Q$ in Figure 4.1b is the $\Delta\Gamma$ (the transformed grain boundary) segment. Hence, the length of the counter clock-wise (ccw) arc $Q'Q$ gives the length of the $\Delta\Gamma$ boundary. Second, the interface between the twin and G1, represented by the ccw arc QQ', is the twin-G1 boundary. The twin-G1 boundary

is composed of CTB and PB facets as characterized in the MD snapshot provided in Figure 3.6.

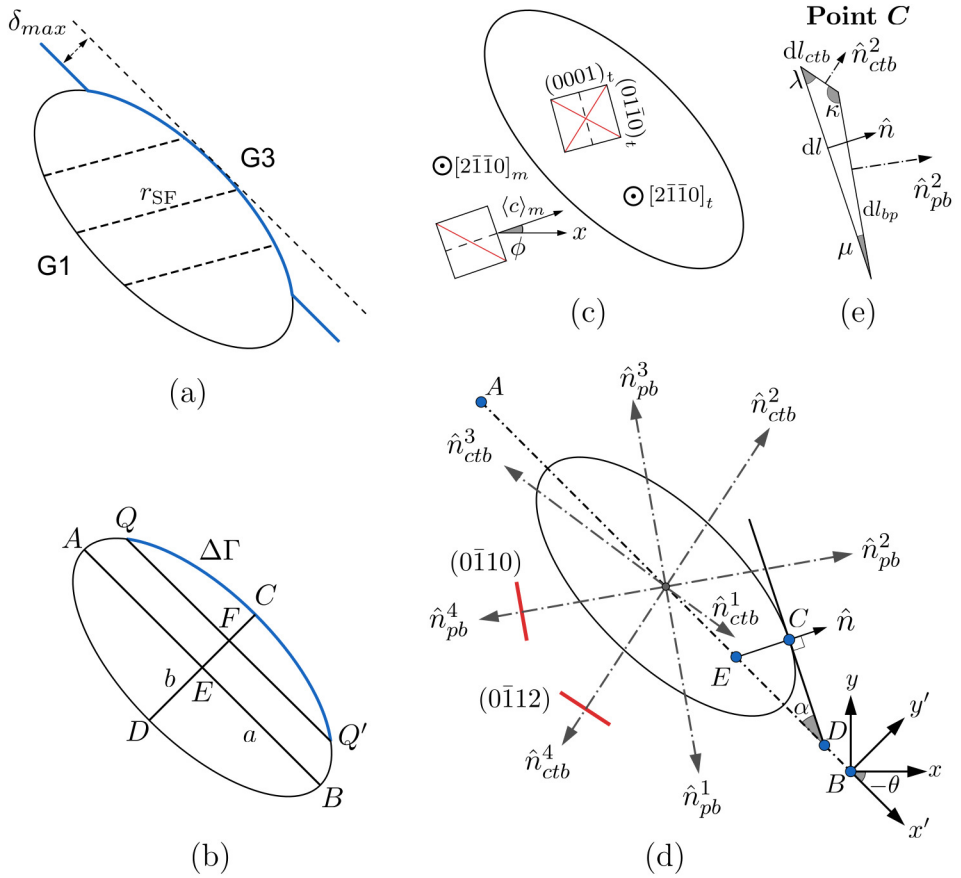

Figure 4.1. The sketches show (a) the bulging of the twin into the neighboring grain and the distribution of SFs inside the twin, (b) the $\Delta\Gamma$ boundary modeled as the $Q'Q$ arc, (c) crystallographic planes that contribute to twin boundary faceting, (d) orientations of the boundary plane normals for the twin lattice and (e) an example triangle construction for boundary decomposition at the representative point C.

The decomposition scheme of the twin-G1 interface in our model is illustrated in Figure 4.1c-e. Figure 4.1c shows a generalized 2D twin-G1 configuration that has the same orientation as the columnar polycrystal shown in Figure 3.1 (observe the rotated basal axes). Here, the crystal orientation of G1 and the twin are such that the c-axis of the parent lattice makes an angle of ϕ with the global x-axis and the twin lattice is mirrored from the parent lattice. The indices of the basal and the prismatic

planes are indicated and the traces of $\{10\bar{1}2\}$ planes are highlighted with red lines on the representative unit cell of the twin lattice. These planes are involved in faceting during twin boundary formation. The angle θ in Figure 4.1d denotes the inclination of the prior grain boundary with respect to the global x-axis. Since twin expansion is assumed to occur only along or perpendicular to the grain boundary, θ is also the angle between the x and x' axes in the model, where the primed axes $x' - y'$ are aligned with the semi-axes of the ellipse. All the ensuing calculations are carried out in the primed axes for convenience.

For the twin-G1 interface decomposition, the ccw arc QQ' (the black arc segment in Figure 4.1b) is divided into sections with respect to the crystallographic plane normals that are shown on the ellipse in Figure 4.1d. While the sketch in Figure 4.1d does not show the location of the arc segments for clarity this partitioning is only relevant for the ccw arc QQ'. Each section is bounded by the unit normals of the faceting planes shown in Figure 4.1c. Specifically, $\hat{n}^i_{ctb}$ are the unit normals of the primary and conjugate twin planes and $\hat{n}^i_{pb}$ are the basal and prismatic plane normals (two normals each to include the positive and negative directions). If the activated twin variant (to find the twin orientation), the ϕ of G1, and the inclination θ of the grain boundary, are given, we can determine the directions $\hat{n}^i_{ctb}$ and $\hat{n}^i_{pb}$ in the $x'y'$-coordinate system by change of basis operations. Each section after this first division is then decomposed into infinitesimal sub-segments, dl, that consist of CTB and PB facets. For example, at an arbitrary point C on the ellipse in Figure 4.1d, the normal $\hat{n}$ lies between bounding normals $\hat{n}^2_{ctb}$ and $\hat{n}^2_{pb}$. Using these three normals, a triangle can be constructed at point C as in Figure 4.1e such that the end points of the infinitesimal arc segment dl are connected by a CTB and a PB step of lengths dl_{ctb} and dl_{pb} that are normal to $\hat{n}^2_{ctb}$ and $\hat{n}^2_{pb}$ respectively. The total length of the CTB and PB components can be calculated by numerically integrating dl_{ctb} and dl_{pb} over the perimeter of the ellipse. The way these infinitesimal triangles are constructed ensures a roughly convex shape of the twin.

For simplicity, all the geometrical calculations associated with the described partitioning scheme are done using the parametric equation of the ellipse. An arbitrary point C on the ellipse with coordinates (x, y) is given by the equations in terms of the major and minor semiaxes (a_1 and a_2) and the parametric angle ψ as

$$x = a_1 \cos\psi \tag{4.2a}$$

$$y = a_2 \sin\psi. \tag{4.2b}$$

The major and minor semiaxes a_1 and a_2 are directions and should not be confused with the radii a and b, where b can be larger than a. The tangent of the angle α that the tangent line at point C makes with the major axis (as depicted in Figure 4.1d) can be expressed in terms of the ellipse parameters as

$$\tan\alpha = \frac{dy}{dx} = \tan\left(-\frac{a_2\cos\psi}{a_1\sin\psi}\right). \tag{4.3}$$

Consequently, the unit normal vector at the same point is (brackets indicate normalization):

$$\hat{n} = \langle a_1 \sin\psi, a_2 \cos\psi \rangle . \tag{4.4}$$

Likewise, for the normal directions $\hat{n}^i_{ctb}$ and $\hat{n}^i_{pb}$, we can write:

$$\hat{n}^i_{pb} = \left\langle a_1 \sin\psi^i_{pb}, a_2 \cos\psi^i_{pb} \right\rangle \tag{4.5a}$$

$$\hat{n}^i_{ctb} = \left\langle a_1 \sin\psi^i_{ctb}, a_2 \cos\psi^i_{ctb} \right\rangle . \tag{4.5b}$$

As stated earlier, the vectors $\hat{n}^i_{ctb}$ and $\hat{n}^i_{pb}$ are already known from the orientation of the twin and the inclination of the ellipse. Therefore, the angular coordinates ψ^i_{ctb} and ψ^i_{pb} of the section boundaries can be calculated directly from Equation (4.5). Since $\hat{n}$, $\hat{n}^i_{ctb}$ and $\hat{n}^i_{pb}$ are all known at point C, the lengths of the CTB and PB steps, $\mathrm{d}l_{ctb}$ and $\mathrm{d}l_{bp}$ respectively, can be calculated in terms of the length of the arc segment $\mathrm{d}l$ by the law of sines as indicated in Figure 4.1e:

$$\frac{\mathrm{d}l}{\sin\kappa} = \frac{\mathrm{d}l_{ctb}}{\sin\mu} = \frac{\mathrm{d}l_{bp}}{\sin\lambda}. \tag{4.6}$$

To compute the total length of CTB and PB facets forming the elliptic twin boundary, $\mathrm{d}l_{ctb}$ and $\mathrm{d}l_{pb}$ are integrated with respect to ψ over each arc section as

$$l_{ctb} = \sum_{i=0} \int_{\psi_i}^{\psi_{i+1}} \mathrm{d}l_{ctb} = \int_{\psi_i}^{\psi_{i+1}} \frac{\sin\mu}{\sin\kappa}\mathrm{d}l = \int_{\psi_i}^{\psi_{i+1}} \frac{\sin\mu}{\sin\kappa} a_1 \sqrt{1 - e^2\cos^2\psi}\,\mathrm{d}\psi \tag{4.7a}$$

$$l_{pb} = \sum_{i=0} \int_{\psi_i}^{\psi_{i+1}} \mathrm{d}l_{pb} = \int_{\psi_i}^{\psi_{i+1}} \frac{\sin\lambda}{\sin\kappa}\mathrm{d}l = \int_{\psi_i}^{\psi_{i+1}} \frac{\sin\lambda}{\sin\kappa} a_1\sqrt{1-e^2\cos^2\psi}\,\mathrm{d}\psi \tag{4.7b}$$

respectively and summed afterwards, where e is the eccentricity of the ellipse. The angles κ, μ, λ are the inverse cosines of the dot products of the corresponding unit normals:

$$\kappa = \pi - \arccos\left(\hat{n}^i_{ctb} \cdot \hat{n}^i_{pb}\right) \tag{4.8a}$$

$$\mu = \arccos\left(\hat{n}^i_{ctb} \cdot \hat{n}\right) \tag{4.8b}$$

$$\lambda = \arccos\left(\hat{n}^i_{pb} \cdot \hat{n}\right). \tag{4.8c}$$

The computation of the length of the $\Delta\Gamma$ segment follows the same approach. To calculate the length of the ccw arc $Q'Q$ in Figure 4.1b, we first need to find the ψ coordinates of the points Q and Q'. Using the intersecting chords theorem, we can write

$$\frac{CF \times FD}{QF^2} = \frac{CE^2}{AE^2}. \tag{4.9}$$

In Equation (4.9), CF and QF are unknown. Since the twin is assumed to be aligned with the grain boundary, FD can be found from the relation $FD = 2b - CF$. However, to have a single solution for a twin with given dimensions, one more condition is needed. We introduce the following condition:

$$CF = \begin{cases} b & \text{if } b \leq \delta_{max} \\ \delta_{max} & b > \delta_{max}. \end{cases} \tag{4.10}$$

The introduced condition suggests that the twin is centralized on the grain boundary if its radius perpendicular to the grain boundary b is shorter than the maximum bulging distance. If b is larger than the maximum bulging distance, then the twin bulges into the neighboring grain by the maximum distance. The actual twin bulging distance is expected to strongly depend on the boundary type. However, to our knowledge, there is no systematic study on the relation between twin embryo geometry and grain boundary misorientation in Mg. The proposed condition is preferred for its simplicity. Using Equation (4.10) to set CF, we solve for QF in Equation (4.9). Since point F is on one of the axes of the ellipse (the minor axis for the geometry depicted in Figure 4.1b), the y' coordinate is already known from CF. Point Q shares the same coordinate

by the construction of the model. Thus, the unknown coordinate is directly equal to the distance QF. After finding the coordinates of points Q and Q', the length of the $\Delta\Gamma$ arc can be calculated from the elliptic integral:

$$l_{\Delta\Gamma} = \int_{Q'}^{Q} \mathrm{d}l = \int_{\psi_{Q'}}^{\psi_Q} a_1 \sqrt{1 - e^2 \cos^2 \psi}\, \mathrm{d}\psi. \tag{4.11}$$

The lengths of the CTB, PB and $\Delta\Gamma$ segments are multiplied by the out-of-plane height of the cylinder t to get the respective areas.

4.1.2. Estimation of Stacking Fault Related Parameters

In Equation (4.1), stacking faults contribute to the total twin energy through the $\sum \gamma_{\mathrm{SF}} A_{\mathrm{SF}}$ and $Kt \sum \ln(r_i/r_0)$ terms where we sum the contribution of individual SFs. Hence, both terms require the calculation of the number N_{SF} of SFs per twin and the length r_i of the ith SF. With a simple approach, N_{SF} can be computed by assuming a constant spacing between SF planes. The experimental studies do not provide quantitative information about the spacing of the I_1 stacking faults inside twins in Mg; they merely verify the presence of dense SF populations inside twins. Modeling these SFs as having a regular spacing between them, the number of SFs per load point measured from the MD simulations (from Chapter 3) was divided by the length of the total major semiaxes of the ellipses given in Figure 3.10 and plotted against the load point in Figure 4.2. The results seen in Figure 4.2 suggests that modeling the fault planes as having a regular spacing is reasonable. The average value of the linear density along the major semiaxis direction is found to be ~ 0.055 1/Å (the average value inferred from Figure 4.2 is divided by two to scale it to the entire diameter). In the MD simulations the fault planes are inclined with respect to the semiaxes of the ellipse. By projection, this corresponds to a linear density of ~ 0.075 1/Å in the fault plane normal direction. Using this density value, we define a perpendicular distance of $d_\perp = 1/0.075 = 13.3$Å. It should be noted that the derived SF density value is likely valid only for the specific orientation relations of the MD simulation of the thesis. The actual SF spacing is expected to vary with the change in the grain boundary character and inclination. However, for practical purposes, we take $d_\perp$ to be constant.

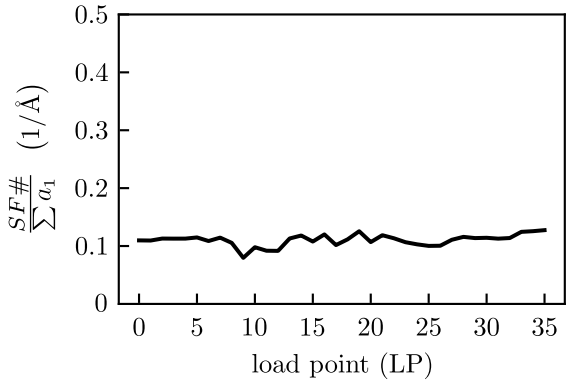

Figure 4.2. The ratio of the number of SF to the total major semiaxis length of the nuclei measured from the MD simulation.

Secondly, we revisit the ellipse geometry to seek a model of individual SF segment lengths r_i. Here, we discuss an explicit and a statistical approach. Figure 4.3 illustrates the main steps of the two approaches for a sample SF orientation ($\phi = 0°$ case in Figure 4.1c). In the explicit approach, we start by placing the longest SF inside the ellipse (for instance, the dashed horizontal line in the middle in Figure 4.3a). Then, we continue placing SFs on both sides of the central SF with the derived spacing $d_\perp$ until the ellipse boundary is reached. The upper and lower bounds for SFs are designated by the horizontal lines that are tangent to the ellipse at the (x_{ini}, y_{ini}) and (x_{fin}, y_{fin}) points. The solid line that connects (x_{ini}, y_{ini}) and (x_{fin}, y_{fin}) is the conjugate diameter to the SF direction and it bisects the SF lines. The longest SF by construction, and the conjugate diameter by definition, pass through the center of the ellipse.

In the explicit approach, the length of the placed SFs that remain inside the ellipse are used as explicit values for r_i. The end points (x_1, y_1) and (x_2, y_2) of each SF need to be found to solve for r_i. To find the end points of a SF, we first find the midpoints (x_m, y_m) of each SF. The midpoints of SFs are equidistantly spaced along the conjugate diameter. The distance between two adjacent SFs along the conjugate diameter can be found by the inverse projection of $d_\perp$ onto the conjugate diameter which requires the relative orientations of the two directions. The slopes of the conjugate diameter and

the SF lines are related through their product as [156]

$$m'm = -\frac{a_2^2}{a_1^2}, \tag{4.12}$$

where m' is the slope of the conjugate diameter and m is the slope of individual SFs. In addition, since the SF lines are oriented along the basal plane, equations similar to Equation (4.5) can be solved to find the ψ_{pb} coordinates of the basal normals. With these, the coordinates of the tangent points can be found in terms of a_1, a_2 and ψ_{pb}^i as:

$$(x_{ini}, y_{ini}) = (a_1 \cos \psi_{pb}^{ini}, a_2 \sin \psi_{pb}^{ini}) \tag{4.13}$$

$$(x_{fin}, y_{fin}) = (a_1 \cos \psi_{pb}^{fin}, a_2 \sin \psi_{pb}^{fin}), \tag{4.14}$$

where ψ_{pb}^{ini} and ψ_{pb}^{fin} are the ψ coordinates of the corresponding basal normals. Consequently, the slope of the conjugate diameter and the slope of the SF lines are readily found to be $m' = (y_{ini} - y_{fin})/(x_{ini} - x_{fin})$ and $m = -(a_2^2)/(a_1^2 m')$ respectively. Since the conjugate diameter and the central SF pass through the origin, the unit vectors along both are known, from which the angle between two lines can be obtained straightforwardly. As a result, the distance d between adjacent SFs along the conjugate diameter can be found in terms of m, m' and $d_\perp$. The midpoint coordinates (x_m, y_m) can, then, be found by traversing along the conjugate diameter by steps with size d. To find (x_1, y_1) and (x_2, y_2) for each SF, we need the equation of each. The quadratic equation for each SF line is found using the slope m and midpoints (x_m, y_m). Finally, solving the quadratic equation for each SF line together with the ellipse equation, we obtain the endpoints of the SFs, and in turn, the r_i's as

$$y_{1,2} = -\frac{a_2^2}{a_1^2 m'} x_{1,2} + \left[y_m + \frac{a_2^2}{a_1^2 m'} x_m \right] \tag{4.15a}$$

$$1 = \frac{x_{1,2}^2}{a_1^2} + \frac{y_{1,2}^2}{a_2^2} \tag{4.15b}$$

$$r_i = \|(x_1, y_1) - (x_2, y_2)\|. \tag{4.15c}$$

Similarly, the value of N_{SF} can be calculated from the obtained parameters as

$$N_{\mathrm{SF}} = 1 + \left\lfloor \frac{l_\perp}{2d_\perp} \right\rfloor, \tag{4.16}$$

where $l_\perp$ is the total perpendicular distance between the bounding SFs as shown in Figure 4.3b. The floor function is used for the explicit approach to get discrete number of stacking faults per twin.

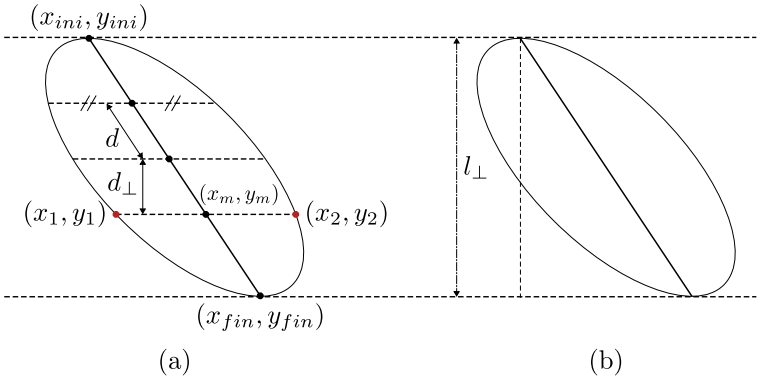

Figure 4.3. (a) the distribution of SFs inside the twin with perpendicular spacing of $d_\perp$. Limiting points of the SF distribution are designated with the horizontal tangent lines at the top and bottom. (b) The perpendicular distance $l_\perp$ between the top and bottom horizontal boundaries.

In the statistical distribution approach, the SF lines are not considered explicitly. Rather, a statistical distribution for SF lines is presumed where the density of SFs is given by $\rho_{SF} = 1/d_\perp = 0.075$. Likewise the expected value of an individual SF line length is calculated from a weighted average as

$$\langle r_{SF} \rangle = \frac{\int r_i \, \mathrm{d}l}{l}, \tag{4.17}$$

where r_i is the length of the SF passing through the integration point. The integration is along the conjugate diameter and the integral is normalized by the length of the conjugate diameter l. The computation of the integrand r_i follows the same steps as the explicit SF method. The number of SF becomes

$$N_{\mathrm{SF}} = l_\perp \times \rho_{SF}. \tag{4.18}$$

The computations of r_i (or r_{SF} for the distribution method) and N_{SF} complete the geometric model. The total SF area is obtained as $\sum_i r_i \times t$ and the argument of the interaction term is obtained as $\sum_i \ln(r_i/r_0)$, where the summations are over the number of SFs. In the distribution method, these expressions become

$$A_{\mathrm{SF}} = N_{\mathrm{SF}} \times r_{SF} \times t, \tag{4.19}$$

and

$$\sum_i \ln r_i/r_0 = N_{\mathrm{SF}} \ \ln\left(\frac{r_{SF}}{r_0}\right). \tag{4.20}$$

The results of both approaches are computed for a range of a and b values and the computed total SF area surfaces are contour-plotted against a and b in Figure 4.4.

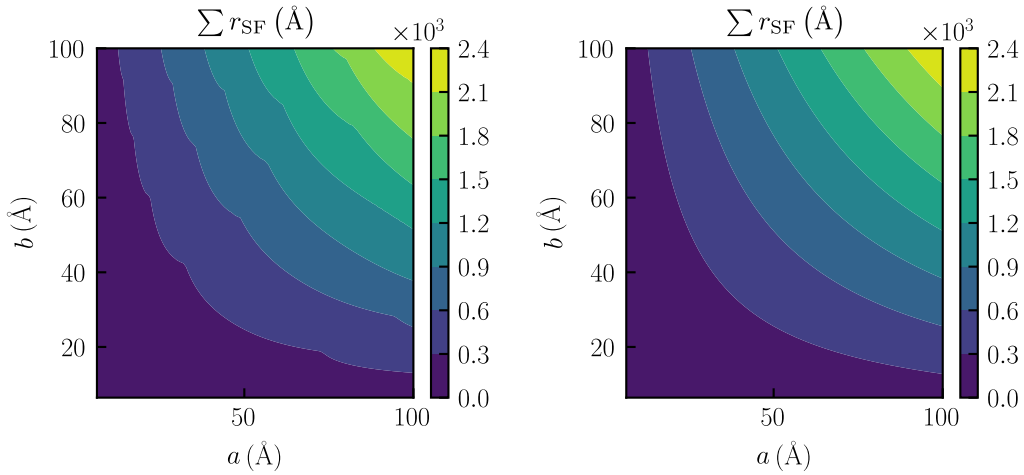

Figure 4.4. Contourplots of the length sum of stacking fault lines as estimated by the (a) explicit stacking fault and (b) statistical distribution of stacking faults approaches over a range of a and b.

Figure 4.4a and Figure 4.4b show the total SF areas predicted by the explicit method and the distribution method respectively. Both surfaces are almost symmetric with respect to a and b. This is expected since the computation of the total length of regularly-spaced lines falling within a region of the plane is analogous to an area calculation. The area of the elliptic face of the cylinder is a function of a_1 and a_2 only and thus the product of the number of stacking faults and SF line lengths should be symmetric in the limit. However, the contour lines in the explicit method plot are not smooth with visible cusps on them. In contrast, the isolines for the distribution method plot do not display any cusps. These cusps cause erratic gradients, and the explicit SF method assumes more regular SF spacing than is supported by the MD results anyway. The statistical approach is therefore much more practical for the ensuing minimum

energy pathway (MEP) computations which will be carried out using a gradient descent method.

4.1.3. Comparison of the Geometric Model Results to MD Results

The computations of stacking fault configurations compose the complete geometric model together with the twin boundary decomposition. Although a direct experimental verification of the geometric model is not available, we can compare the predictions of the model to the MD measurements of the respective variables. The orientations as well as the dimensions $a,\ b$ of the ellipses fitted to the twin nuclei observed in the MD simulation were provided in Figure 3.10. We feed this data to the geometric model (with the tilt angle of the parent grain ϕ set to 0° and θ set to -30°), and compute all the geometric variables for the respective geometries. The results are plotted against the MD measurements in Figure 4.5. The volume curves for MD and the model match perfectly since the semiaxes of the ellipse fitted to the MD data were scaled with respect to the volume measurements from the MD simulation.

Although the MD and the model perimeter area curves are generally close to each other, indicating the overall success of the model, comparison of individual elements require closer attention. First, there seems to be an offset between the A_{CTB} prediction of the model and the MD measurements. The average ratio of model predictions to MD measurements for A_{CTB} is 0.83. This value is curiously close to the average ratio of MD measurements to the model predictions for A_{PB} which is 0.79. This could be related to Gibbs-Wulff relation of boundary energies and facet lengths [58]. In the proposed geometric model, the decomposition scheme is based on only the directions of the faceting plane normals and energetic effects on faceting were not considered.

Secondly, the comparative trends of the A_{PB} curves of the model and the MD measurements differ from what we observe in the A_{CTB} plot. At around load point 23, the A_{PB} curve obtained from the model rises to match the MD curve. Around the same load point, the $A_{\Delta\Gamma}$ curve for the model takes a turn downwards. This change in

the trend is a direct result of the way we treat the bulging distance in the model. To see this, first revisit Figure 3.10.

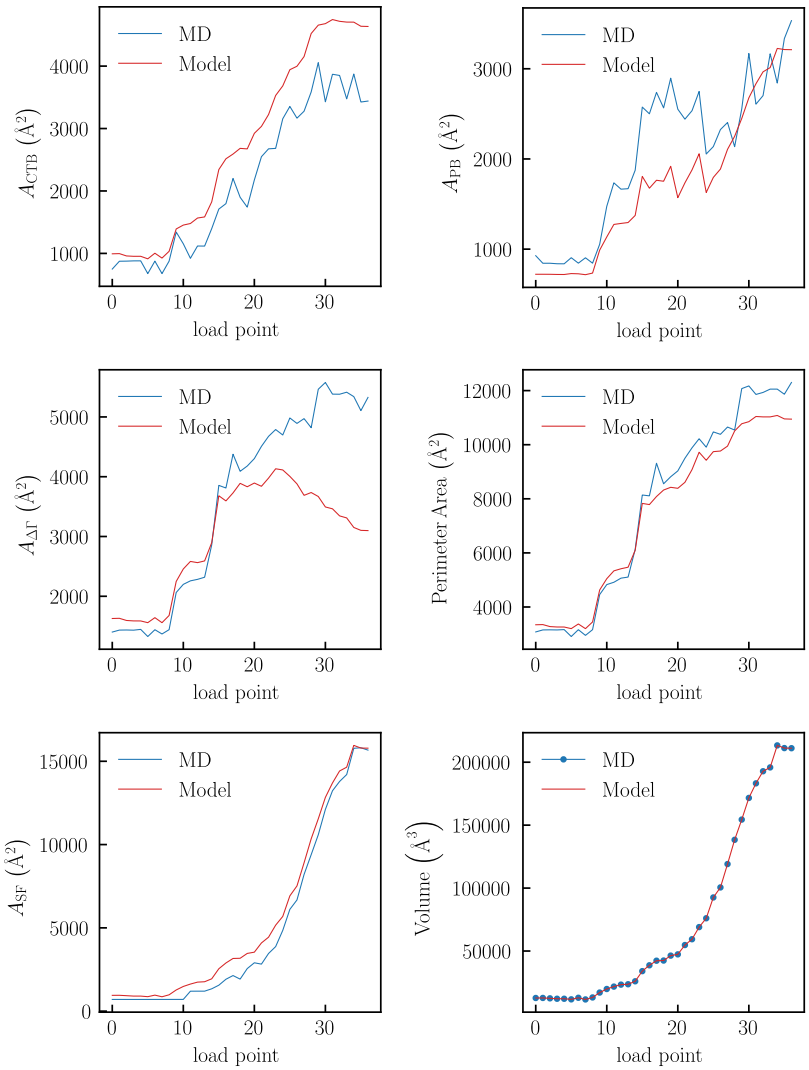

Figure 4.5. Magnitudes of the various $\{10\bar{1}2\}$ twin related structures as estimated by the geometric model for the twin nuclei dimensions given in Figure 3.10 are compared to MD measurements. In addition to the computations of the CTB, PB, SF and $\Delta\Gamma$ areas, overall changes in the total perimeter area and twin volume are reported.

Around load point 23, the nucleus 3 coalesce with nucleus 2, the unified twin reaches the triple points on both sides and the a_1 dimension stays constant afterwards. Simultaneously, the twin growth towards the interior of the grain starts leading to an increase of the a_2 dimension. On the other hand, since we posit the condition in the

model that the twin can bulge into the neighboring grain only to a maximum distance, a part of the $\Delta\Gamma$ segment is transferred to A_{PB} when the twin dimension along the grain boundary stabilizes and the twin grows perpendicular to the grain boundary. In contrast, in the MD simulation, the area of the $\Delta\Gamma$ boundary stays almost a constant fraction of the total perimeter area even after load point 23 as seen from Figure 4.6. However, the results of the model are not directly comparable to the MD results, as the twinning event observed in the MD simulation involves merging of multiple nuclei which is not addressed by the model. The approximation of $A_{\Delta\Gamma}$, otherwise, seems to be reasonable within the limitations of the model. The A_{SF} term, on the other hand, seems to be successfully predicted by the model. The current geometric model, estimates the bending points satisfactorily despite its simplicity.

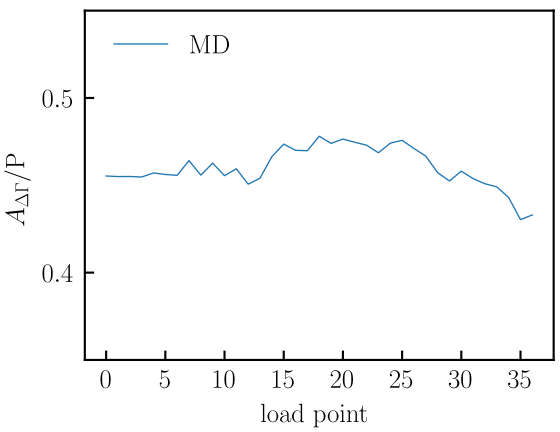

Figure 4.6. The ratio of $A_{\Delta\Gamma}$ to the perimeter area as measured from MD output is plotted against the load point.

The natural logarithms of stacking fault lengths are also computed from the model and are plotted against the MD measurements in Figure 4.7. Here the prediction is less successful compared to the stacking fault area estimation. Specifically, the two curves differ by larger distances when the twin nuclei are small. At this stage, some of the twin nuclei in the MD simulation have dimensions shorter than the stacking fault spacing $d_{\perp}$, and likely contain one or even zero stacking faults. The stacking fault distribution approach, on the other hand, effetively assumes a fractional number of stacking faults. This discrepancy causes the overshoot at the initial stage. The stacking fault model

becomes much more successful when the nuclei reach considerable size. Overall, the bending points of the MD curve is matched by the model curve.

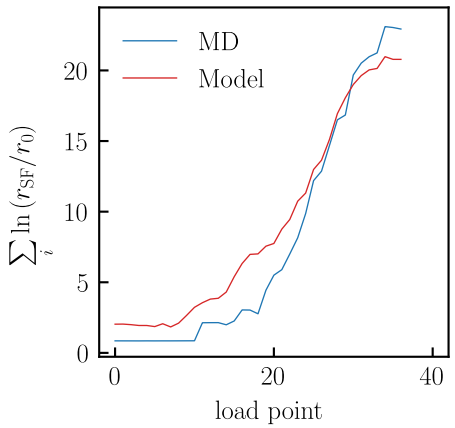

Figure 4.7. The natural logarithms of stacking fault lengths as estimated by the geometric model is compared to the MD measurements. The natural logarithms are normalized by twice the lattice constant of Mg (and are not multiplied by the thickness of the cylinder).

After the verification of the model, we compute the geometric variables appearing in the total energy expression given by Equation (4.1) for a and b values between the range of 6.42 Å to 2000 Å. The tilt angle ϕ of the parent grain is set to 0° and the grain boundary inclination θ is set to $-30°$. These parameters match those of the twinning boundary examined in Chapter 3 closely.

The lower limit of 6.42 Å for a and b is enforced to avoid twins with dimensions shorter than the dimensions of a unit cell. This is particularly required for the $Kt\sum_i \ln(r_i/r_0)$ term, since stacking fault lines shorter than the reference separation of two times the lattice constant causes this term to unphysically perturb the potential energy surface. The results are presented in Figure 4.8 via contour plots of the geometric variables.

The stacking fault area and the twin volume plots are symmetric with respect to the dimensions of the twin. On the other hand, the A_{CTB}, A_{PB}, r_{SF} and $A_{\Delta\Gamma}$ plots

strongly depend on the aspect ratio of the twin (AR), suggesting that the shape of a critical nucleus can be affected by the interplay of these terms.

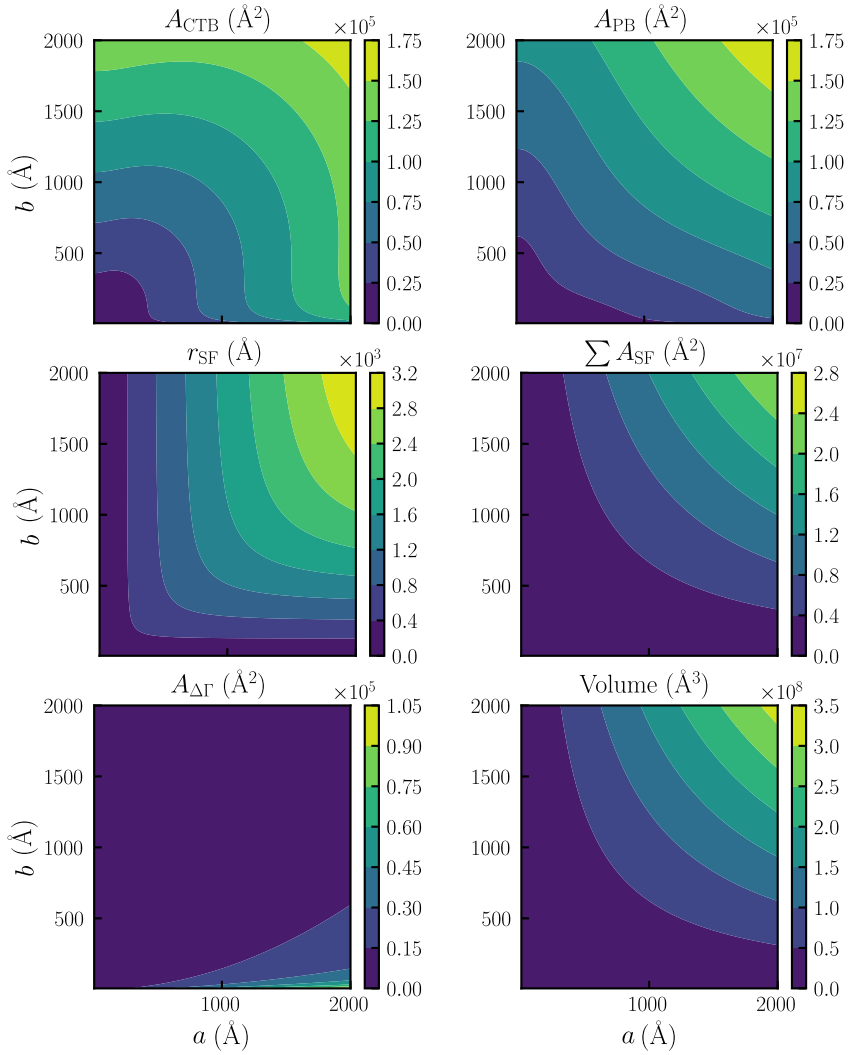

Figure 4.8. The areas of the CTB, PB, $\Delta\Gamma$ interfaces, expected lengths of individual SF lines in the x-y plane, the total area of the SF's (extending along the z-direction in Figure 3.1), and the total volume of the twins plotted against a and b.

It is important to note again that the problem regarding the $\Delta\Gamma$ model discussed above is clearly visible from the $A_{\Delta\Gamma}$ plot in Figure 4.8. For constant values of a, $A_{\Delta\Gamma}$ values artificially decrease with increasing b. However, the trends of the isolines are indeed correct: the dependence of $A_{\Delta\Gamma}$ on a is much stronger than its dependence on

b, though this is not visible with the color scaling in the figure. Hence, the values of $A_{\Delta\Gamma}$ will be assumed reasonable and will be used for qualitative analysis of the results.

4.2. Results

4.2.1. Total Energy of a Twin

We revisit Equation (2.20) to compute the potential energy of a twin associated with the generated elastic fields, which is the remaining term E_{inh} in Equation (4.1). Accordingly, E_{inh} is

$$E_{\text{inh}} = -\frac{1}{2}V\sigma_{ij}^{0}\varepsilon_{ij}^{*} - V\sigma_{ij}^{0}\varepsilon_{ij}^{p} - \frac{1}{2}V\sigma_{ij}\varepsilon_{ij}^{p}, \tag{4.21}$$

where σ_{ij}^{0} is the applied far-field stress, σ_{ij} is the stress inside the twin, ε_{ij}^{p} is the transformation shear strain for the $\{10\bar{1}2\}$ twin mode, ε_{ij}^{*} is the disturbance strain caused by the difference between elastic properties of the medium and the inhomogeneity, and V is the volume of the twin.

The computation of E_{inh} completes the micromechanical model proposed in Equation (4.1). Hence, the computed geometric quantities are substituted into Equation (4.1) together with E_{inh} to get the total potential energies of twin nuclei with different dimensions. E_{inh} for the free and the loaded states are computed for the a and b range in the contour plots shown in Figure 4.8. The tilt angle ϕ for the parent grain and the grain boundary inclination θ are set to 0° and 30° respectively to match the configurations considered in the MD simulation and the geometric computations. The systems are compressed along the y-axis (with respect to the coordinate system in Figure 4.1c). The resultant total potential energies of twins are conveyed with contour plots in Figure 4.9.

The total energy of twins at the unloaded state are shown in Figure 4.9a. Accordingly, as the size of the twin enlarges, the elastic strain energy of the twin increases symmetrically with respect to a and b, yielding symmetry about the diagonal in Figure 4.9a. When the system is uniaxially compressed to an external stress of $\sigma_{yy} = -0.85$ GPa

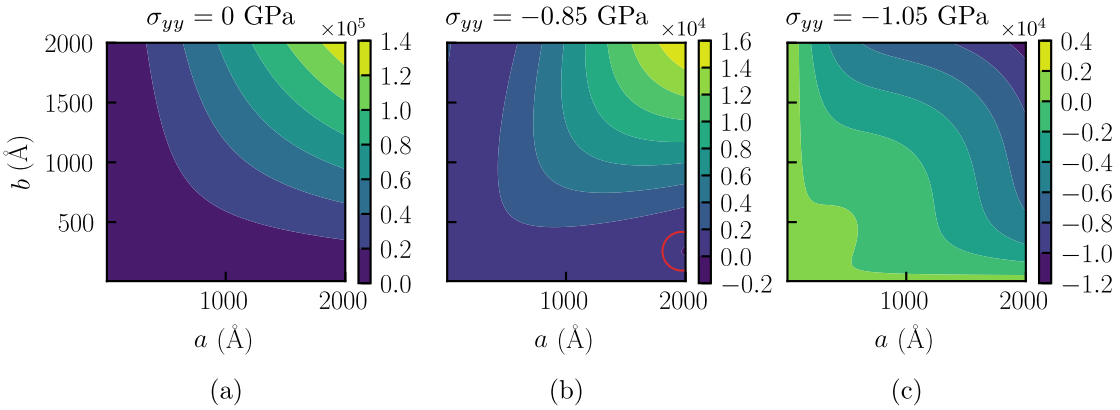

Figure 4.9. ΔE for the (a) unloaded ($\sigma_{ij}^0 = 0$) and (b-c) the loaded states ($\sigma_{yy} = -0.85\,\text{GPa}$ and $\sigma_{yy} = -1.25\,\text{GPa}$) as estimated by the micromechanical model.

along the y-direction, the elastic strain energy due to the twin transformation strain is partially relieved by the interaction of the twin transformation strain with the applied far-field stress as shown in Figure 4.9b. A $\{10\bar{1}2\}$ twin, for the present parent grain orientation, extends the structure along the x-axis and contracts it along the y-axis. Hence, the interaction of the far-field stress and the transformation strain in the present setting reduces the total strain energy. This corresponds to the second term on the right hand side in Equation (4.21) that quantifies the energy reduction from the unloaded to the loaded state. If the external stresses are high enough, a second energetically favorable state other than the untwinned state appears, signified by the emergence of one or more negative energy regions on the plot (loosely referred to as a 'basin' here). In Figure 4.9b, two different basins at locations almost symmetric with respect to the diagonal emerge pointing to the fact that two twin geometries are favored at this stress level for the given parent grain orientation. The first basin appears close to the lower right corner (circled in red on the contour plot), indicating an energetically favorable configuration with the corresponding (a, b) dimensions. The second basin on the upper left becomes noticeable only after when the stress is increased to -0.95 GPa (the energy plot for this case is omitted here for brevity but is provided in Figure 4.11). $\Delta\Gamma$ reduces the potential energy by a larger amount near the lower right basin, favoring the nucleation of the twin with the observed geometry. When the magnitude of the external stress is increased to $\sigma_{yy} = -1.25$ GPa, the energy basin shifts towards

the region on the diagonal in Figure 4.9c which was a previously a high energy region in Figure 4.9b. This signifies the change in the preferred final geometry of the twin in response to increased loading.

The change in the preferred twin geometry lies in the interplay of the energetic terms. At lower applied stresses, the energetic contributions from the interfacial terms are comparable to the volumetric term (i.e. the Eshelby term), causing the preferred twin geometry to maximize the length of the transformed grain boundary (which relieves excess energy) and reducing the overall interfacial and stacking fault energy. That resulted in a preferred geometry with a high aspect ratio where the major axis was aligned with the grain boundary. Further increasing the load causes the volumetric term to dominate and the system minimizes the overall interface area and maximizes the volume, shifting the energy basin towards the diagonal of the plot.

The minimum energy path (MEP) from the state where there is no twin to the state where there is a twin with a favorable geometry can be found from the total energy plots. The minimum energy path corresponds to the path between the initial and the basins of the energy surface that goes through the saddle point. The saddle point of the potential energy surface corresponds to the critical geometry for twin nucleation. The MEP follows the direction normal to the steepest descent direction. The height of the potential energy surface along the MEP, or equivalently the potential energy at the saddle point, gives the potential energy barrier against twinning and is a key quantity for the determination of the twinning condition under loading. Likewise, the shape of the twin at the saddle point gives the shape of the critical nucleus.

4.2.2. Finding the Minimum Energy Path

The MEP for the potential energy surfaces can be found using the well established zero-temperature-string (ZTS) method [157]. In this method, the MEP is initially estimated as a straight path between predetermined initial state and final states. Then, the actual MEP is found by iterative relaxation of the path by aligning it with the

gradient of the potential energy field. The ZTS method is known to be a robust method for finding local minimum energy paths for relatively well-behaving potential surfaces.

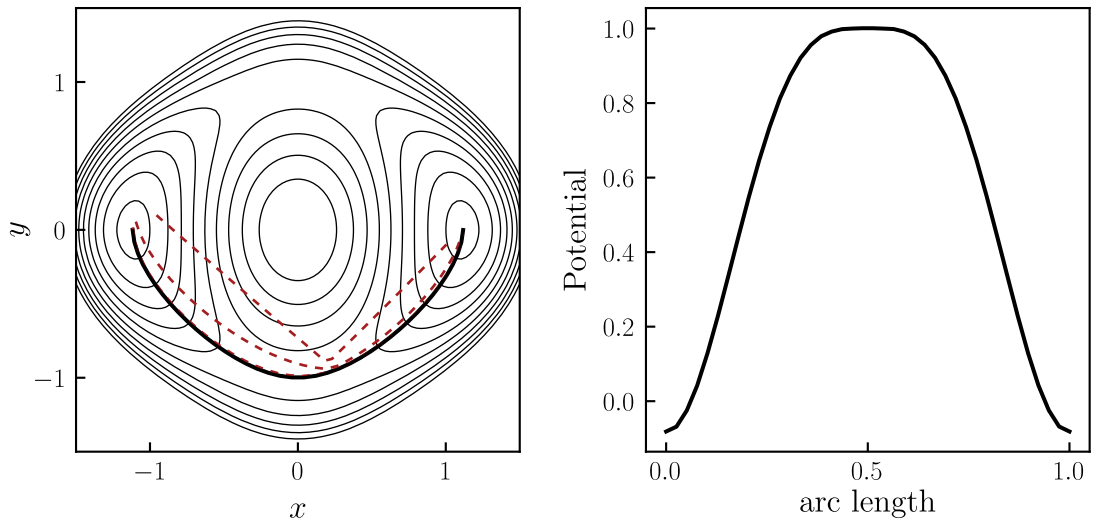

Figure 4.10. An illustration of the ZTS method. (a) The initial and intermediate guesses of MEP between the two basins are shown with dashed red curves. The actual MEP is shown with the solid black curve. (b) Potential energy profile over the actual MEP curve. The MEP curve is parametrized by the arc length between the string nodes.

An illustration of the ZTS method is given in Figure 4.10 over a sample potential field. In Figure 4.10a, a 2-D potential surface is plotted in a contour map. First, the MEP is guessed with an initial chain that consists of nodes. If the potential surface is already available, a guess for the transition basin can also be provided, making the initial estimate a piecewise path instead of a straight one. The trial paths for the sample potential in Figure 4.10a are shown by the dashed curves. As the chain is relaxed, the chain is nudged incrementally to finally match the actual MEP (the solid curve in Figure 4.10) with the velocity of the evolution of the path given by the gradient of the potential field:

$$\boldsymbol{v} = -\nabla E. \tag{4.22}$$

In the ZTS method, after nudging the points at a timestep, the path is reparametrized such that the arc lengths between the new parametrization points of the path are kept equal. When the MEP is reached, the potential energies at the parametrization points provides the potential energy profile over the MEP as shown in Figure 4.10b.

The same objective is also achieved by the nudged elastic band (NEB) method [158], but the nudging of the trial chain is constrained to the direction perpendicular to the chain in this method, adding computational complexity to the implementation. The ZTS method is preferred for its computational simplicity. As a side note, using ZTS on potential energy surfaces with more than two energy basins can cause the trial path to relax to the path between unintended basins. This requires a careful initialization of the path between the intended end points.

We apply the ZTS method to the total energy surfaces obtained from the micromechanical model. The MEPs of the potential energy surfaces are found for applied stresses of $\sigma_{yy} = -0.85$ GPa, $\sigma_{yy} = -0.95$ GPa, $\sigma_{yy} = -1.05$ GPa, $\sigma_{yy} = -1.15$ GPa, $\sigma_{yy} = -1.25$ GPa and $\sigma_{yy} = -1.4$ GPa. Moreover, the potential energy profiles over the MEPs are concurrently computed.

The potential energy surfaces for all but the $\sigma_{yy} = -1.15$ GPa and $\sigma_{yy} = -1.4$ GPa cases are presented with contour plots in Figure 4.11 next to the potential energy profiles along the MEPs. The MEPs are indicated on the respective potential energy surfaces. The colorbar levels are limited to a fraction of the maximum potential energy of the surfaces to ease the identification of the emerging energy basins as well as the transition regions. The white regions represent the high energy regions that are filtered out by the colorbar limit. The critical points for each loading case are marked with a dot on the potential energy profiles.

The first observation from the plots is that as the applied stress gradually increases, the critical points of the potential surfaces shift towards the left.

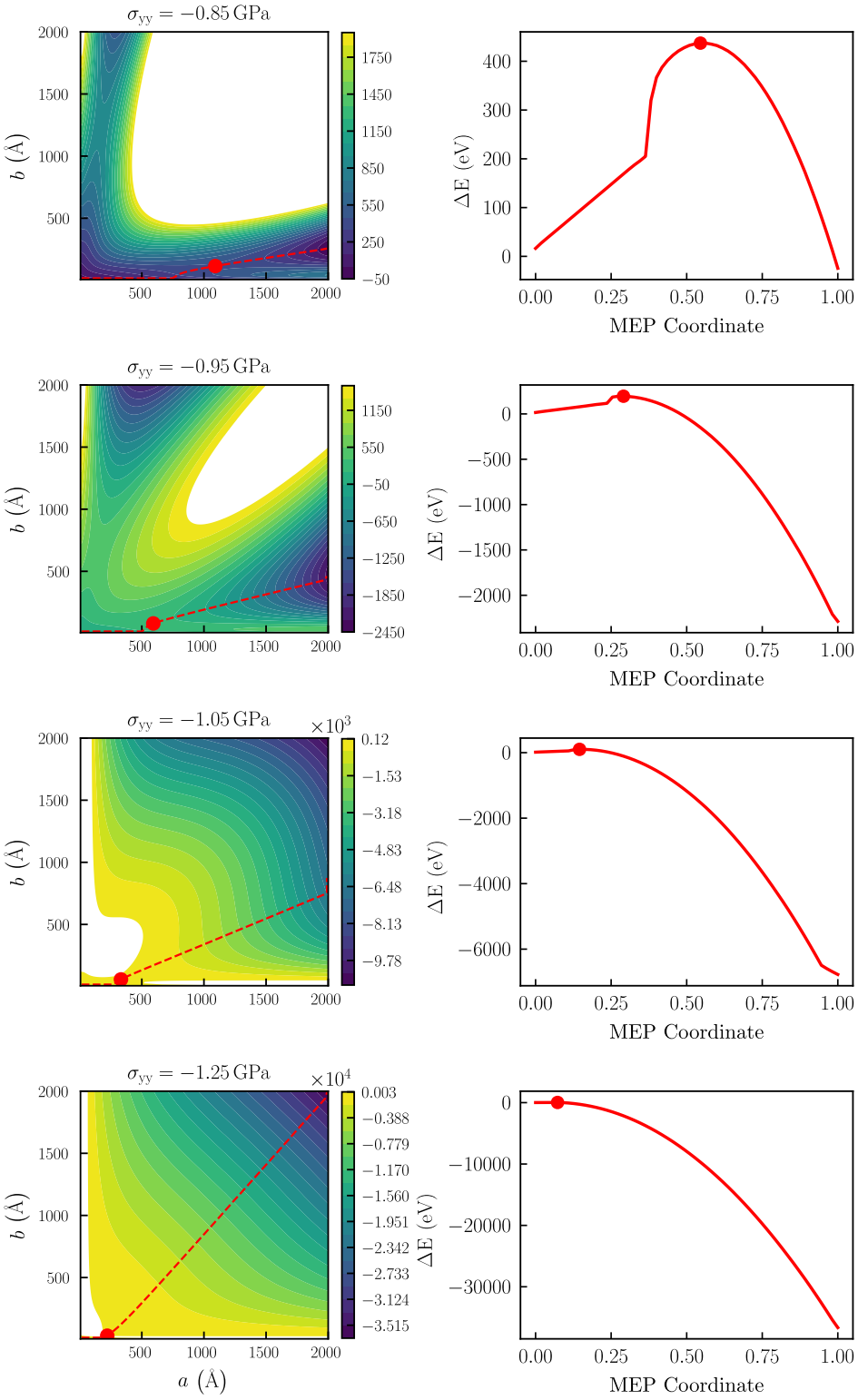

Figure 4.11. The contour plots of total potential energy surfaces for applied stress levels of $\sigma_{yy} = -0.85$, -0.95, -1.05, and -1.25 GPa. The MEPs are designated on each plot along with the location of the critical point. Potential energy profiles along the MEPs are provided on the right.

When there is no applied stress, nucleating a twin of any size increases the energy of the material and the only minimum is at the origin. As the driving force is gradually increases, smaller nuclei with finite size become stable conforming with the expectations of the classical nucleation theory. Empirically however, for a twin embryo to nucleate and become stable it has to have nanoscale dimensions. Since a large twin is difficult to nucleate due to the very large energy barriers, only ellipse dimensions smaller than 200 nm are considered here. Second, notice that the critical nuclei for all applied stresses have aspect ratios larger than one. Although the supercritical nuclei (i.e. nuclei that are larger than the critical nuclei) will eventually grow into more circular shapes at high stresses, the critical nuclei have increasing aspect ratios with decreasing stress. For clarity, the critical data for all applied stress levels (including the -1.15 GPa and -1.4 GPa cases) are plotted against the applied stress level in Figure 4.12. The a^c and b^c plots quantify the first observation whereas the AR plot corroborates the second observation, at least for the situation where $\gamma_{\Delta\Gamma} < 0$.

One outlier to the trends above is the erratic upturn in the AR curve around $\sigma_{yy} = -1.25$ GPa. On closer inspection, this occurs because a^c stays almost constant while b^c drops from 51.6 Å to 31.7 Å as the stress magnitude increases from -1.15 GPa to -1.25 GPa. The significant energy barrier drop from 58.9 eV to 30.8 eV, despite almost the same a^c dimensions of the two twins, raises questions about the geometric model. Specifically, the reduction in interface energy from the change of boundary character tends to extend the twin nucleus along the prior grain boundary, and this effect increases as the relative magnitude of the other energetic contributions decreases with decreasing critical nucleus size and increasing applied stress. Whether this upturn on the AR curve is a physical or a numerical effect, it does not prevent us making qualitative conclusions about twin nucleation.

The ΔE^c plot provided in Figure 4.12 rapidly decreases with increasing applied stress, displaying the characteristics of a stress-dependent activation energy curve for a thermally activated process. However, the energy barrier does not completely vanish even at extremely high stresses.

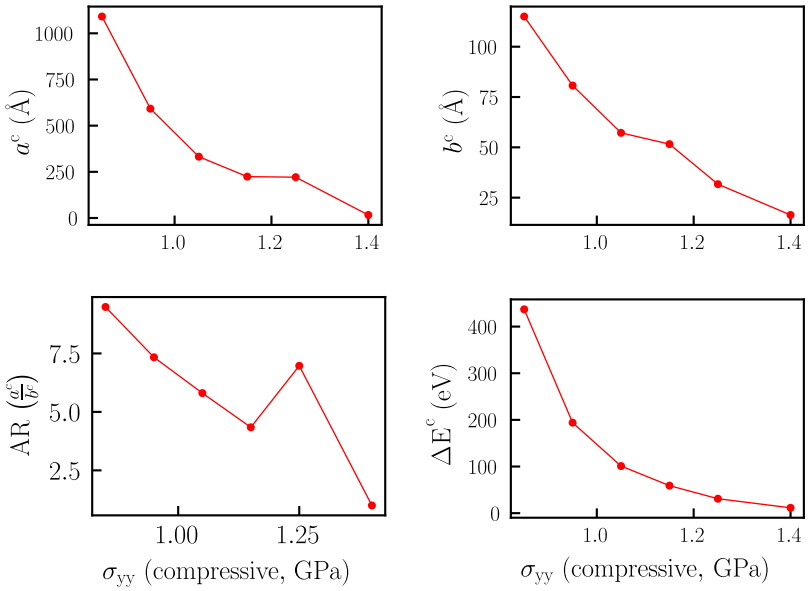

Figure 4.12. The evolutions of a^c, b^c, aspect ratio and ΔE^c for the critical nuclei with increasing applied stress determined from MEPs of the potential energy surfaces.

At -1.4 GPa, the energy barrier is calculated to be 11.5 eV. The corresponding dimensions of the twin at the same applied stress are 16.5 Å for a and b, already at the order of 4 to 5 lattice constants. Such a twin would have a size of a few atoms which is typically the case for the empirical nuclei. For the same applied stress level, the position of the critical point is the first point on the MEP, signaling that what is effectively the observable activation stress is reached.

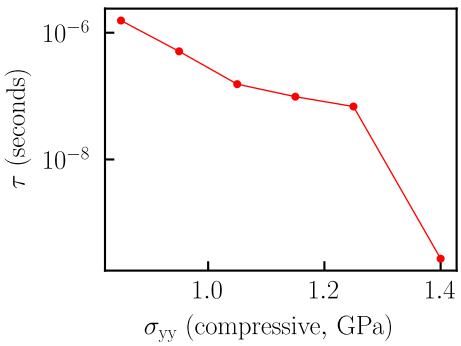

Figure 4.13. The change of incubation time for the critical nuclei with varying applied stress levels estimated by the micromechanical model. The axis of the incubation time plotted on a logarithmic scale.

Although a crude measure for this work, the incubation time can provide further insight about the mode of twin nucleation. Thus, the incubation time for the critical nuclei at the tested applied stress levels are calculated using Equation 2.12 and is plotted in Figure 4.13 against the applied stress. The incubation time curve is roughly exponentially decreasing until $\sigma_{yy} = -1.25$ GPa where there is a significant drop to $\sigma_{yy} = -1.4$ GPa. As discussed above, this is a sign of what is effectively the observable activation condition.

4.3. Discussion

The stress required for the observable activation of the $\{10\bar{1}2\}$ mode in Mg is found to be between -1.25 GPa and -1.4 GPa. In bulk Mg, however, the critical resolved shear stress for the $\{10\bar{1}2\}$ mode is generally reported to be two orders of magnitude lower than this value. As the study by Liu et al. [94] suggests, the discrepancy between the theoretical value and the experimental value suggests that twinning takes place at defect-dense localities inside a real sample with atomic defect reaction facilitating twin formation. Despite the discrepancy between the experimental value and the theoretical value, the model results can still provide insight into the energetic barrier for twin nucleation and the preferred shape of twins in the embryo stage. Liu et al. [94] also developed an analytical model based on the Eshelby formalism and used it to study homogeneous nucleation of a spheroidal shaped twin in Mg. They found that the energy barrier against the formation of a $\{10\bar{1}2\}$ twin with a size of $55 \times 61 \times 19.4$ Å^3 is about 80 eV. They formed this twin with a resolved shear stress of -1.1 GPa over the twin plane, which corresponds approximately to a normal stress of -2.2 GPa. Compared to their finding, our results suggest a $\sim 36\%$ reduction in CRSS and $\sim 85\%$ reduction in ΔE^c. The geometries of the nuclei are different though, so a direct comparison between the observable activation stresses is not entirely accurate. Nevertheless, both the required applied stresses and energy barrier sizes we found are significantly lower than for the homogeneous model. Another first-principles study by Ishii et al. [159] that focused on homogeneous nucleation of $\{10\bar{1}2\}$ in Mg reported a CRSS value of 3 GPa, which corroborates both the findings of this study and the

one by Liu et al. [94]. Barrett et al. [39] investigated the heterogeneous nucleation of $\{10\bar{1}2\}$ twins in single crystals and reported a CRSS value of 2.2 GPa for the $\{10\bar{1}2\}$ mechanism in the presence of a small void. Compared to these studies, our approach predicts much lower CRSS or ΔE^c values closer to the empirical ones, and enables qualitative explanation of the role of twin related structures observed to be at play in heterogeneous nucleation.

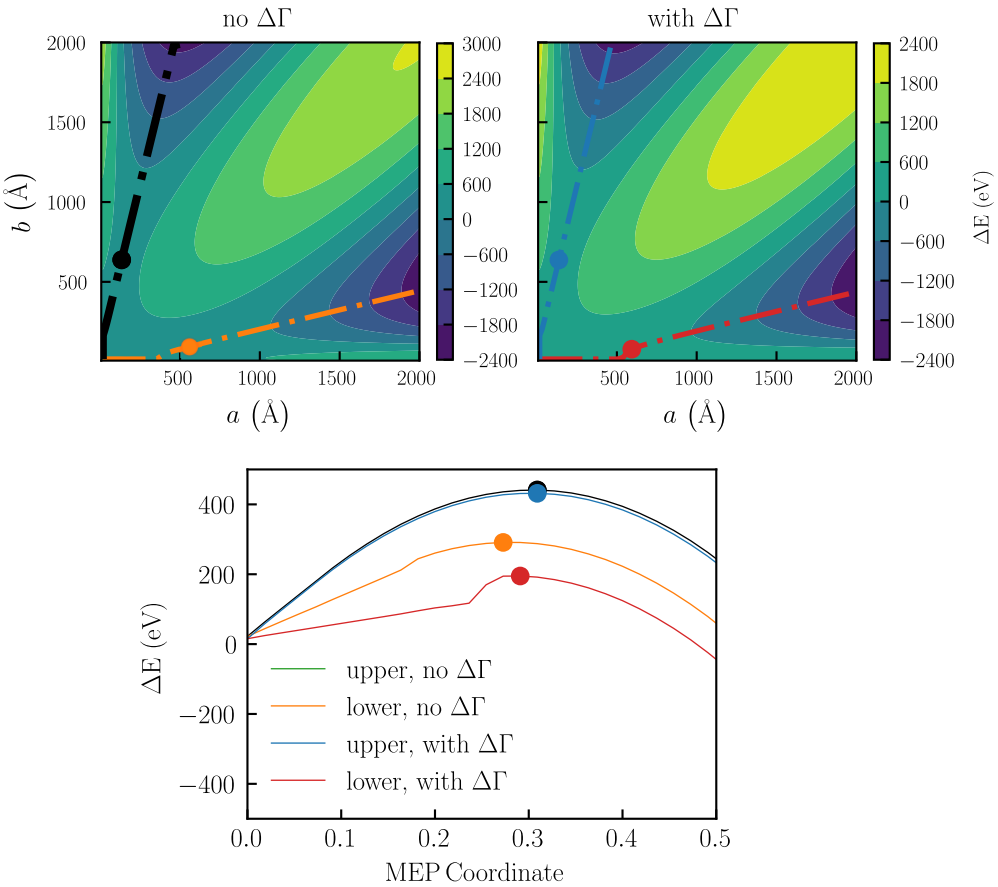

Figure 4.14. The alternative MEP paths between the origin and basin states at $\sigma_{yy} = -0.95$ GPa stress that include and exclude the contribution of the $\gamma_{\Delta\Gamma} A_{\Delta\Gamma}$ term are shown. Below the potential energy plots is the energy profile along each MEP.

The effect of the $\Delta\Gamma$ boundary merits more consideration. Recalling the discussion of the occurrence of multiple basins, we said that the lower right basin was more favorable than the upper left basin in Figure 4.9b. To quantify the effect of the $\Delta\Gamma$

boundary, the total potential energy surface is compared in Figure 4.14 (contour plot on the right) with the potential energy of the same twin except for the contribution of the $\Delta\Gamma$ term (contour plot on the left). For both surfaces, the ZTS routine is run for all the candidate paths and the resultant MEPs are designated. The potential energy profiles for all four MEPs are plotted on the same graph below the contour maps. The difference between the ΔE^cs of the two paths for the 'with $\Delta\Gamma$' surface is about 55% (the blue curve has an energy barrier of 431 eV whereas the red curve has an energy barrier of 195 eV). The difference between the two paths for the 'no $\Delta\Gamma$' path is found to be 33% (the green curve has an energy barrier of 440 eV whereas the orange curve has an energy barrier of 291 eV). Consequently, the inclusion of the $\Delta\Gamma$ term caused about a 33% reduction in the energy barrier for the lower path but left the upper path almost unchanged. The significant reduction in the energy barrier caused by the transformation of the grain boundary increases the likelihood of a nucleation event occurring over the lower path.

5. CONCLUSIONS

In the first part of a two-part study, we performed molecular dynamics simulations to discern energetic terms contributing to the total energy of a $\{10\bar{1}2\}$ twin nucleating from a grain boundary in a columnar polycrystal Mg. The main conclusions of the first part are detailed at the end of Chapter 3. To briefly recapitulate, an energetic model was proposed relating the total energy of a twin to several geometric quantities and material properties. The evolution of the geometric quantities associated with twin-related structures were measured by MD and the unknown material properties were estimated by linear regression. The results of Chapter 3 implied that the energetic change caused by the transformation of the grain boundary acting as the nucleation site was significant, suggesting that this could be part of the explanation for preferred twin nucleation sites in polycrystalline Mg.

In the second part of the study, we laid the groundwork for a geometric model for 2D $\{10\bar{1}2\}$ twins where the twin is modeled as an elliptic cylinder. The geometric variables involved in the energetic model proposed in the first part of the study were calculated and then substituted along with the material properties into the potential energy expression. Potential energy surfaces for a wide range of twin configurations under different levels of applied stresses were calculated. MEPs over the potential energy surface were found by the zero temperature string method. The incubation times for the resulting critical nucleus configurations were found within the classical nucleation theory framework.

The geometric model was generally able to reasonably predict the geometric variables in agreement with the MD measurements. Specifically, the total stacking fault area inside the twin was predicted accurately. The areas of CTB and PB facets show a close trend with the MD measurements, though with relatively consistent offsets. We speculate that an energetic factor like the Gibbs-Wulff relations of boundary energies plays a role in the twin-parent grain boundary decomposition. The $\Delta\Gamma$ boundary area

was predicted accurately for twin configurations with a shorter radius perpendicular to the grain boundary. The geometric model proposed here is simple though, meaning it could be improved with conditions motivated by twin physics to remedy the shortcomings.

The results of the potential energy calculations show qualitative agreement with other atomic scale or analytic studies of $\{10\bar{1}2\}$ nucleation in Mg. However, our results include significantly lowered energy barriers for $\{10\bar{1}2\}$ nucleation compared to those of homogeneous nucleation studies as should be expected. Specifically, the energy reduction caused by the $\Delta\Gamma$ term is found to be a possible deciding factor for the twinning site and the twinning trajectory as expressed by the MEP. Given the computational efficiency as well as robustness of the model, we suggest that the model could be a useful tool to direct MD simulations. For instance, instead of performing hundreds of MD simulations with grain orientations and grain boundary inclinations at regular intervals,, the micromechanical model could be used to identify critical grain boundary configurations prone to accommodate twins. These critical configurations could then be examined in much greater detail at the atomic scale through MD simulations.

6. FUTURE WORK

The currently developed framework to study $\{10\bar{1}2\}$ twinning nucleation in Mg is based on a compound model that predicts both the quantities of geometric variables associated with the twin-related structures and the total energy due to these structures from a few mesoscopic variables. Namely, these variables are the orientation of the parent grain (ϕ) and the inclination of the grain boundary (θ)) with respect to the applied loading direction, the dimensions of the elliptic cylinder ($a,\ b$) in the plane of twin shear and the twin variant that is activated in response to external loading. Thus, in principal, this model can study twin nucleation in systems with different orientations for G1 and G3. Changing orientations of G1 and G3 directly changes ϕ and $\gamma_{\Delta\Gamma}$. The ϕ and θ are built-in into the model as geometric parameters, but $\gamma_{\Delta\Gamma}$ is known only for a specific G1-G3 misorientation and a grain boundary orientation between them. To generalize the findings of the study, the grain boundary energies in Mg as a function of misorientations of neighboring grains would need to be available.. Obtaining all these energies for different grain boundaries could involve performing a vast array of MD simulations. Alternatively, semi-analytic methods could be used to estimate grain boundary energies [160]. However, determination of grain boundary energies for the entire spectrum is an exhaustive task and is practically intractable by MD. Therefore, only a subset of grain boundaries that constitute critical structures observed in Mg would be studied. These MD simulations could also be used to verify the results predicted by the developed model.

The relative effects of the contributing terms involved in the potential energy of a twin could be studied before beginning computations of $\gamma_{\Delta\Gamma}$ though. A sensitivity study would treat the geometric and material parameters given to the model as free variables. This task seems tractable and is intended as future work. An immediate sub-task for this work would be updating the $\Delta\Gamma$ model in the current geometric model to address the predicted length of the transformed grain boundary.

Finally, as a research opportunity, the current model could be generalized to 3D by extending boundary decomposition schemes to ellipsoidal surface decompositions. However, a fully 3D granular structure involves quadruple points where 4 grains meet and around which stress concentrations can be very high making quadruple points potentially prone to twin nucleation. In such an event, twinning could cause the transformation of more than one boundary. That kind of transformation would require a more complex analysis [161] than the one carried out in Chapter 3.

REFERENCES

1. Pollock, T. M., "Weight Loss with Magnesium Alloys", *Science*, Vol. 328, No. 5981, pp. 985–986, 2010.

2. Abbott, T. B., "Magnesium: Industrial and Research Developments Over the Last 15 Years", *Corrosion*, Vol. 71, No. 2, pp. 120–127, 2015.

3. Housecroft, C. and A. Sharpe, *Inorganic Chemistry*, Third Edition, Prentice Hall, Gosport, 2008.

4. Nie, J. F., K. S. Shin and Z. R. Zeng, "Microstructure, Deformation, and Property of Wrought Magnesium Alloys", *Metallurgical and Materials Transactions A: Physical Metallurgy and Materials Science*, Vol. 51, No. 12, pp. 6045–6109, 2020.

5. Agnew, S. R., "Deformation Mechanisms of Magnesium Alloys", C. Bettles and M. Barnett (Editors), *Advances in Wrought Magnesium Alloys*, pp. 63–104, Woodhead Publishing, Cambridge, 2012.

6. Taylor, G. I., "Plastic Strain in Metals", *Journal of Institute of Metals*, Vol. 62, pp. 307–324, 1938.

7. Kocks, U. F. and D. G. Westlake, "The Importance of Twinning for the Ductility of CPH Polycrystals", *Transactions of the Metallurgical Society of AIME*, Vol. 239, No. 7, pp. 1107–1109, 1967.

8. Wang, J., I. J. Beyerlein and C. N. Tomé, "An Atomic and Probabilistic Perspective on Twin Nucleation in Mg", *Scripta Materialia*, Vol. 63, No. 7, pp. 741–746, 2010.

9. El Kadiri, H., J. C. Baird, J. Kapil, A. L. Oppedal, M. Cherkaoui and S. C. Vogel, "Flow Asymmetry and Nucleation Stresses of $\{10\bar{1}2\}$ Twinning and Non-Basal

Slip in Magnesium", *International Journal of Plasticity*, Vol. 44, pp. 111–120, 2013.

10. Orozco-Caballero, A., D. Lunt, J. D. Robson and J. Quinta da Fonseca, "How Magnesium Accommodates Local Deformation Incompatibility: A High-Resolution Digital Image Correlation Study", *Acta Materialia*, Vol. 133, pp. 367–379, 2017.

11. Reed-Hill, R. and W. D. Robertson, "Additional Modes of Deformation Twinning in Magnesium", *Acta Metallurgica*, Vol. 5, No. 12, pp. 717–727, 1957.

12. Kitahara, T., S. Ando, M. Tsushida, H. Kitahara and H. Tonda, "Deformation Behavior of Magnesium Single Crystals in C-Axis Compression", *Key Engineering Materials*, Vol. 345-346, pp. 129–132, 2007.

13. Barnett, M. R., "Twinning and the Ductility of Magnesium Alloys. Part I: "Tension" Twins", *Materials Science and Engineering A*, Vol. 464, No. 1-2, pp. 1–7, 2007.

14. Barnett, M. R., "Twinning and the Ductility of Magnesium Alloys. Part II. "Contraction" Twins", *Materials Science and Engineering: A*, Vol. 464, No. 1-2, pp. 8–16, 2007.

15. Pozuelo, M., S. N. Mathaudhu, S. Kim, B. Li, W. H. Kao and J. M. Yang, "Nanotwins in Nanocrystalline Mg-Al Alloys: An Insight From High-Resolution Tem and Molecular Dynamics Simulation", *Philosophical Magazine Letters*, Vol. 93, No. 11, pp. 640–647, 2013.

16. El Kadiri, H., C. D. Barrett, J. Wang and C. N. Tomé, "Why Are $\{10\bar{1}2\}$ Twins Profuse in Magnesium?", *Acta Materialia*, Vol. 85, pp. 354–361, 2015.

17. Lou, X. Y., M. Li, R. K. Boger, S. R. Agnew and R. H. Wagoner, "Hardening Evolution of AZ31B Mg Sheet", *International Journal of Plasticity*, Vol. 23, No. 1, pp. 44–86, 2007.

18. Proust, G., C. N. Tomé, A. Jain and S. R. Agnew, "Modeling the Effect of Twinning and Detwinning During Strain-Path Changes of Magnesium Alloy AZ31", *International Journal of Plasticity*, Vol. 25, No. 5, pp. 861–880, 2009.

19. Wu, W., P. K. Liaw and K. An, "Unraveling Cyclic Deformation Mechanisms of a Rolled Magnesium Alloy Using In Situ Neutron Diffraction", *Acta Materialia*, Vol. 85, pp. 343–353, 2015.

20. Aydiner, C. C. and M. A. Telemez, "Multiscale Deformation Heterogeneity in Twinning Magnesium Investigated With In Situ Image Correlation", *International Journal of Plasticity*, Vol. 56, pp. 203–218, 2014.

21. Kapan, E., N. Shafaghi, S. Uçar and C. C. Aydıner, "Texture-Dependent Character of Strain Heterogeneity in Magnesium AZ31 Under Reversed Loading", *Materials Science and Engineering A*, Vol. 684, pp. 706–711, 2017.

22. Shafaghi, N., E. Kapan and C. C. Aydıner, "Cyclic Strain Heterogeneity and Damage Formation in Rolled Magnesium Via In Situ Microscopic Image Correlation", *Experimental Mechanics*, Vol. 60, No. 6, pp. 735–751, 2020.

23. Ando, D., J. Koike and Y. Sutou, "Relationship Between Deformation Twinning and Surface Step Formation in AZ31 Magnesium Alloys", *Acta Materialia*, Vol. 58, No. 13, pp. 4316–4324, 2010.

24. Koike, J., N. Fujiyama, D. Ando and Y. Sutou, "Roles of Deformation Twinning and Dislocation Slip in the Fatigue Failure Mechanism of AZ31 Mg Alloys", *Scripta Materialia*, Vol. 63, No. 7, pp. 747–750, 2010.

25. Ando, D., J. Koike and Y. Sutou, "The Role of Deformation Twinning in the Fracture Behavior and Mechanism of Basal Textured Magnesium Alloys", *Materials Science and Engineering A*, Vol. 600, pp. 145–152, 2014.

26. Yu, Q., J. Zhang and Y. Jiang, "Fatigue Damage Development in Pure Polycrystalline Magnesium Under Cyclic Tension-Compression Loading", *Materials Science and Engineering A*, Vol. 528, No. 25-26, pp. 7816–7826, 2011.

27. Vasilev, E. and M. Knezevic, "Role of Microstructural Heterogeneities in Damage Formation and Fracture of Oligocrystalline Mg Under Tensile Loading", *Materials Science and Engineering A*, Vol. 827, p. 142096, 2021.

28. Huppmann, M., M. Lentz, S. Chedid and W. Reimers, "Analyses of Deformation Twinning in the Extruded Magnesium Alloy AZ31 After Compressive and Cyclic Loading", *Journal of Materials Science*, Vol. 46, No. 4, pp. 938–950, 2011.

29. Kumar, M. A. and I. J. Beyerlein, "Local Microstructure and Micromechanical Stress Evolution During Deformation Twinning in Hexagonal Polycrystals", *Journal of Materials Research*, Vol. 35, No. 3, pp. 217–241, 2020.

30. Jiang, L., J. J. Jonas, R. K. Mishra, A. A. Luo, A. K. Sachdev and S. Godet, "Twinning and Texture Development in Two Mg Alloys Subjected to Loading Along Three Different Strain Paths", *Acta Materialia*, Vol. 55, No. 11, pp. 3899–3910, 2007.

31. Knezevic, M., A. Levinson, R. Harris, R. K. Mishra, R. D. Doherty and S. R. Kalidindi, "Deformation Twinning in Az31 : Influence on Strain Hardening and Texture Evolution", *Acta Materialia*, Vol. 58, No. 19, pp. 6230–6242, 2010.

32. Hirth, J. P. and J. Lothe, *Theory of Dislocations*, Second Edition, Krieger Publishing Company, Malabar, 1992.

33. Asaro, R. J. and A. Needleman, "Overview No. 42 Texture Development and Strain Hardening in Rate Dependent Polycrystals", *Acta Metallurgica*, Vol. 33, No. 6, pp. 923–953, 1985.

34. Roters, F., P. Eisenlohr, L. Hantcherli, D. D. Tjahjanto, T. R. Bieler and D. Raabe, "Overview of Constitutive Laws, Kinematics, Homogenization and Multiscale Methods in Crystal Plasticity Finite-Element Modeling: Theory, Experiments, Applications", *Acta Materialia*, Vol. 58, No. 4, pp. 1152–1211, 2010.

35. Roters, F., P. Eisenlohr, T. R. Bieler and D. Raabe, *Crystal Plasticity Finite Element Methods: In Materials Science and Engineering*, Wiley-VCH, Singapore, 2011.

36. Kalidindi, S. R., "Incorporation of Deformation Twinning in Crystal Plasticity Models", *Journal of the Mechanics and Physics of Solids*, Vol. 46, No. 2, pp. 267–290, 1998.

37. Staroselsky, A. and L. Anand, "A Constitutive Model for Hcp Materials Deforming by Slip and Twinning: Application to Magnesium Alloy AZ31B", *International Journal of Plasticity*, Vol. 19, No. 10, pp. 1843–1864, 2003.

38. Aydiner, C. C., J. V. Bernier, B. Clausen, U. Lienert, C. N. Tomé and D. W. Brown, "Evolution of Stress in Individual Grains and Twins in a Magnesium Alloy Aggregate", *Physical Review B*, Vol. 80, No. 2, pp. 1–6, 2009.

39. Barrett, C. D., H. El Kadiri and M. A. Tschopp, "Breakdown of the Schmid Law in Homogeneous and Heterogeneous Nucleation Events of Slip and Twinning in Magnesium", *Journal of the Mechanics and Physics of Solids*, Vol. 60, No. 12, pp. 2084–2099, 2012.

40. Cheng, J. and S. Ghosh, "Crystal Plasticity Finite Element Modeling of Discrete Twin Evolution in Polycrystalline Magnesium", *Journal of the Mechanics and Physics of Solids*, Vol. 99, pp. 512–538, 2017.

41. Cheng, J., J. Shen, R. K. Mishra and S. Ghosh, "Discrete Twin Evolution in Mg Alloys Using a Novel Crystal Plasticity Finite Element Model", *Acta Materialia*, Vol. 149, pp. 142–153, 2018.

42. Cheng, J., X. Hu, H. Jong Bong, S. Ghosh and X. Sun, "A Finite Element Formulation for Deformation Twinning Induced Strain Localization in Polycrystal Magnesium Alloys", *Computational Materials Science*, Vol. 190, p. 110323, 2021.

43. Ardeljan, M., R. J. McCabe, I. J. Beyerlein and M. Knezevic, "Explicit Incorporation of Deformation Twins Into Crystal Plasticity Finite Element Models", *Computer Methods in Applied Mechanics and Engineering*, Vol. 295, pp. 396–413, 2015.

44. Paudel, Y., D. Giri, M. W. Priddy, C. D. Barrett, K. Inal, M. A. Tschopp, H. Rhee and H. El Kadiri, "A Review on Capturing Twin Nucleation in Crystal Plasticity for Hexagonal Metals", *Metals*, Vol. 11, No. 9, pp. 1–53, 2021.

45. Cheng, J., H. Jong Bong, H. Qiao, X. Hu, X. Sun, S. Ghosh and P. Wu, "Comparison of Three State-of-the-Art Crystal Plasticity Based Deformation Twinning Models for Magnesium Alloys", *Computational Materials Science*, Vol. 210, p. 111480, 2022.

46. Beyerlein, I. J. and M. Knezevic, "Review of Microstructure and Micromechanism-Based Constitutive Modeling of Polycrystals With a Low-Symmetry Crystal Structure", *Journal of Materials Research*, Vol. 33, No. 22, pp. 3711–3738, 2018.

47. Pitteri, M., "On the Kinematics of Mechanical Twinning in Crystals", *Archive for Rational Mechanics and Analysis*, Vol. 88, No. 1, pp. 25–57, 1985.

48. Sun, D., M. Ponga, K. Bhattacharya and M. Ortiz, "Proliferation of Twinning in Hexagonal Close-Packed Metals: Application to Magnesium", *Journal of the Mechanics and Physics of Solids*, Vol. 112, pp. 368–384, 2018.

49. Gao, Y., J.-H. Ke, B. Mao, Y. Liao, Y. Zheng and L. Aagesen, "Twinning Path Determined by Broken Symmetry: A Revisit to Deformation Twinning in Hexagonal Close-Packed Titanium and Zirconium", *Physical Review Materials*, Vol. 4, No. 7, pp. 1–6, 2020.

50. Hirth, J. P., J. Wang and C. N. Tomé, "Disconnections and Other Defects Associated with Twin Interfaces", *Progress in Materials Science*, Vol. 83, pp. 417–471, 2016.

51. Liu, Y., N. Li, S. Shao, M. Gong, J. Wang, R. J. McCabe, Y. Jiang and C. N. Tomé, "Characterizing the Boundary Lateral to the Shear Direction of Deformation Twins in Magnesium", *Nature Communications*, Vol. 7, pp. 8–13, 2016.

52. Liu, Y., P. Z. Tang, M. Y. Gong, R. J. McCabe, J. Wang and C. N. Tomé, "Three-dimensional Character of the Deformation Twin in Magnesium", *Nature Communications*, Vol. 10, No. 1, pp. 1–7, 2019.

53. Wang, S., M. Gong, R. J. McCabe, L. Capolungo, J. Wang and C. N. Tomé, "Characteristic Boundaries Associated With Three-Dimensional Twins in Hexagonal Metals", *Science Advances*, Vol. 6, No. 28, p. eaaz2600, 2020.

54. Gong, M., J. P. Hirth, Y. Liu, Y. Shen and J. Wang, "Interface Structures and Twinning Mechanisms of Twins in Hexagonal Metals", *Materials Research Letters*, Vol. 5, No. 7, pp. 449–464, 2017.

55. Gong, M., J. Graham, V. Taupin and L. Capolungo, "The Effects of Stress, Temperature and Facet Structure on Growth of $\{10\bar{1}2\}$ Twins in Mg: A Molecular Dynamics and Phase Field Study", *Acta Materialia*, Vol. 208, p. 116603, 2021.

56. Spearot, D. E., V. Taupin, K. Dang and L. Capolungo, "Structure and Kinetics of Three-Dimensional Defects on the $\{10\bar{1}2\}$ Twin Boundary in Magnesium: Atomistic and Phase-Field Simulations", *Mechanics of Materials*, Vol. 143, p. 103314, 2020.

57. Pei, Z., X. Zhang, T. Hickel, M. Friák, S. Sandlöbes, B. Dutta and J. Neugebauer, "Atomic Structures of Twin Boundaries in Hexagonal Close-Packed Metallic Crystals With Particular Focus on Mg", *npj Computational Materials*, Vol. 3, No. 1, pp. 1–6, 2017.

58. Paidar, V. and A. Ostapovets, "The Balance Between the Energies of the Symmetric $\left(10\bar{1}2\right)$ Twin Boundaries and Asymmetric Basal/prismatic Interfaces in Hcp Metals", *Materials Letters*, Vol. 198, pp. 93–96, 2017.

59. Xu, B., L. Capolungo and D. Rodney, "On the Importance of Prismatic/basal Interfaces in the Growth of $\left(10\bar{1}2\right)$ Twins in Hexagonal Close Packed Crystals", *Scripta Materialia*, Vol. 68, No. 11, pp. 901–904, 2013.

60. Leclercq, L., L. Capolungo and D. Rodney, "Atomic-scale Comparison Between $\{\bar{1}101\}$ and $\{\bar{1}102\}$ Twin Growth Mechanisms in Magnesium", *Materials Research Letters*, Vol. 2, No. 3, pp. 152–159, 2014.

61. Sato, Y., T. Swinburne, S. Ogata and D. Rodney, "Anharmonic Effect on the Thermally Activated Migration of $\{10\bar{1}2\}$ Twin Interfaces in Magnesium", *Materials Research Letters*, Vol. 9, No. 5, pp. 231–238, 2021.

62. Hu, Y., V. Turlo, I. J. Beyerlein, S. Mahajan, E. J. Lavernia, J. M. Schoenung and T. J. Rupert, "Disconnection-mediated Twin Embryo Growth in Mg", *Acta Materialia*, Vol. 194, pp. 437–451, 2020.

63. Hu, Y. and D. M. Kochmann, "Atomistic Insight Into Three-Dimensional Twin Embryo Growth in Mg Alloys", *Journal of Materials Science*, Vol. 58, No. 9, pp. 3972–3995, 2023.

64. Sun, Q., X. Zhang, Y. Shu, L. Tan and Q. Liu, "Two Types of Basal Stacking Faults Within $\{10\bar{1}2\}$ Twin in Deformed Magnesium Alloy", *Materials Letters*, Vol. 185, pp. 355–358, 2016.

65. Song, S. G. and G. T. Gray, "Transmission Electron Microscopy Examination and Analysis of an Anomalous Stacking Fault in H.c.p. Metals", *Philosophical Magazine A: Physics of Condensed Matter, Structure, Defects and Mechanical Properties*, Vol. 71, No. 2, pp. 263–274, 1995.

66. Zhang, X. Y., B. Li and Q. Liu, "Non-Equilibrium Basal Stacking Faults in Hexagonal Close-Packed Metals", *Acta Materialia*, Vol. 90, pp. 140–150, 2015.

67. Wang, F., K. Hazeli, K. D. Molodov, C. D. Barrett, T. Al-Samman, D. A. Molodov, A. Kontsos, K. T. Ramesh, H. El Kadiri and S. R. Agnew, "Characteristic Dislocation Substructure in $\{10\bar{1}2\}$ Twins in Hexagonal Metals", *Scripta Materialia*, Vol. 143, pp. 81–85, 2018.

68. Li, B., Q. Sun and X. Y. Zhang, "Lattice Correspondence Analysis on the Formation Mechanism for Partial Stacking Faults in Hexagonal Close-Packed Metals", *Computational Materials Science*, Vol. 198, 2021.

69. Ostapovets, A., A. Serra and R. C. Pond, "Non-Diffusional Growth Mechanism of I1 Basal Stacking-Faults Inside Twins in Hcp Metals", *Scripta Materialia*, Vol. 172, pp. 149–153, 2019.

70. Wang, F., Y. Gu, R. J. McCabe, L. Capolungo, J. A. El-Awady and S. R. Agnew, "<c+a> Dislocations in $\{10\bar{1}2\}$ Twins in Mg: A Kinematic and Energetic Requirement", *Acta Materialia*, Vol. 195, pp. 13–24, 2020.

71. Yue, Y., Y. Zhang and J. F. Nie, "Stability of Single-Atomic-Layer-Height Disconnections on $\left(10\bar{1}2\right)$ Twin Boundary in Mg", *Scripta Materialia*, Vol. 209, p. 114407, 2022.

72. Christian, J. W. and S. Mahajan, "Deformation Twinning", *Progress in Materials Science*, Vol. 39, pp. 1–157, 1995.

73. Su, Y., M. Arul Kumar and I. J. Beyerlein, "Critical Shape for the Growth of Grain Boundary Twin Embryos in Mg and Mg Alloys: Crystal Plasticity Modeling", *Alloys*, Vol. 1, No. 2, pp. 212–231, 2022.

74. Jonas, J. J., S. Mu, T. Al-Samman, G. Gottstein, L. Jiang and E. Martin, "The Role of Strain Accommodation During the Variant Selection of Primary Twins in Magnesium", *Acta Materialia*, Vol. 59, No. 5, pp. 2046–2056, 2011.

75. Ostapovets, A. and A. Serra, "Characterization of the Matrix – Twin Interface of a $(10\bar{1}2)$ Twin During Growth", *Philosophical Magazine*, Vol. 94, No. 25, pp. 2827–2839, 2014.

76. Wang, J., S. K. Yadav, J. P. Hirth, C. N. Tomé and I. J. Beyerlein, "Pure-Shuffle Nucleation of Deformation Twins in Hexagonal-Close-Packed Metals", *Materials Research Letters*, Vol. 1, No. 3, pp. 126–132, 2013.

77. He, Y., B. Li, C. Wang and S. X. Mao, "Direct Observation of Dual-Step Twinning Nucleation in Hexagonal Close-Packed Crystals", *Nature Communications*, Vol. 11, No. 1, pp. 1–8, 2020.

78. Huang, Q., Q. Zhu, Y. Chen, M. Gong, J. Li, Z. Zhang, W. Yang, J. Wang, H. Zhou and J. Wang, "Twinning-Assisted Dynamic Adjustment of Grain Boundary Mobility", *Nature Communications*, Vol. 12, No. 1, 2021.

79. Molnár, P., A. Jäger and P. Lejček, "Twin Nucleation at Grain Boundaries in Mg-3 wt.% Al-1 Wt.% Zn Alloy Processed by Equal Channel Angular Pressing", *Scripta Materialia*, Vol. 67, No. 5, pp. 467–470, 2012.

80. Yu, Q., L. Qi, K. Chen, R. K. Mishra, J. Li and A. M. Minor, "The Nanostructured Origin of Deformation Twinning", *Nano Letters*, Vol. 12, No. 2, pp. 887–892, 2012.

81. Jiang, L., V. R. Radmilović, J. E. Sabisch, L. Qi, A. M. Minor, D. C. Chrzan and M. Asta, "Twin Nucleation From a Single <c+a> Dislocation in Hexagonal Close-Packed Crystals", *Acta Materialia*, Vol. 202, pp. 35–41, 2021.

82. Su, H., X. Zhou, S. Zheng, H. Ye and Z. Yang, "Dislocation Facilitated Formation and Evolution of Basal-prismatic/prismatic-basal Interfaces in a Mg alloy", *Scripta Materialia*, Vol. 206, p. 114237, 2022.

83. Jiang, L., M. Gong, J. Wang, Z. Pan, X. Wang, D. Zhang, Y. M. Wang, J. Ciston, A. M. Minor, M. Xu, X. Pan, T. J. Rupert, S. Mahajan, E. J. Lavernia, I. J. Beyerlein and J. M. Schoenung, "Visualization and Validation of Twin Nucleation and Early-Stage Growth in Magnesium", *Nature Communications*, Vol. 13, No. 1, pp. 1–11, 2022.

84. Fernández, A., A. Jérusalem, I. Gutiérrez-Urrutia and M. T. Pérez-Prado, "Three-Dimensional Investigation of Grain Boundary-Twin Interactions in a Mg AZ31 Alloy by Electron Backscatter Diffraction and Continuum Modeling", *Acta Materialia*, Vol. 61, No. 20, pp. 7679–7692, 2013.

85. Barrett, C. D. and H. El Kadiri, "The Roles of Grain Boundary Dislocations and Disclinations in the Nucleation of $\{10\bar{1}2\}$ Twinning", *Acta Materialia*, Vol. 63, pp. 1–15, 2014.

86. Orme, A. D., I. Chelladurai, T. M. Rampton, D. T. Fullwood, A. Khosravani, M. P. Miles and R. K. Mishra, "Insights Into Twinning in Mg AZ31: A Combined

EBSD and Machine Learning Study", *Computational Materials Science*, Vol. 124, pp. 353–363, 2016.

87. Khosravani, A., D. T. Fullwood, B. L. Adams, T. M. Rampton, M. P. Miles and R. K. Mishra, "Nucleation and Propagation of $\{10\bar{1}2\}$ Twins in AZ31 Magnesium Alloy", *Acta Materialia*, Vol. 100, pp. 202–214, 2015.

88. Meyers, M. A., O. Vöhringer and V. A. Lubarda, "The Onset of Twinning in Metals: A Constitutive Description", *Acta Materialia*, Vol. 49, No. 19, pp. 4025–4039, 2001.

89. Wang, J., Q. Yu, Y. Jiang and I. J. Beyerlein, "Twinning-Associated Boundaries in Hexagonal Close-Packed Metals", *JOM*, Vol. 66, No. 1, pp. 95–101, 2014.

90. Yu, Q., J. Wang, Y. Jiang, R. J. McCabe, N. Li and C. N. Tomé, "Twin-Twin Interactions in Magnesium", *Acta Materialia*, Vol. 77, pp. 28–42, 2014.

91. Lee, J. K. and M. H. Yoo, "Elastic Strain Energy of Deformation Twinning in Tetragonal Crystals", *Metallurgical Transactions A*, Vol. 21, No. 9, pp. 2521–2530, 1990.

92. Yoo, M. H. and J. K. Lee, "Deformation Twinning in H.c.p. Metals and Alloys", *Philosophical Magazine A: Physics of Condensed Matter, Structure, Defects and Mechanical Properties*, Vol. 63, No. 5, pp. 987–1000, 1991.

93. Lebensohn, R. A. and C. N. Tomé, "A Study of the Stress State Associated With Twinning Nucleation and Propagation in H.c.p. Materials", *Philosophical Magazine A: Physics of Condensed Matter, Structure, Defects and Mechanical Properties*, Vol. 63, No. 5, p. 1116, 1991.

94. Liu, H., F. Lin, N. Moelans, L. Peng, J. Nie and I. Beyerlein, "Three-dimensional Shape and Stress Field of a Deformation Twin in Magnesium", *Acta Materialia*, Vol. 250, p. 118845, 2023.

95. Liu, H., F. Lin, P. Liu, Y. Yue, K. S. Shin, L. Peng, L. Delannay, J. F. Nie and N. Moelans, "Variant Selection of Primary–secondary Extension Twin Pairs in Magnesium: An Analytical Calculation Study", *Acta Materialia*, Vol. 219, p. 117221, 2021.

96. Paudel, Y. R., C. Barrett, S. Mujahid, H. Rhee and H. El Kadiri, "Micromechanics-Based Strain Energy Study of $\{10\bar{1}2\}$ Twin-Band Pattern in a Three-Point Bend Mg Alloy", *Journal of Materials Research*, Vol. 38, No. 2, pp. 461–472, 2023.

97. Fan, H., Y. Zhu, J. A. El-Awady and D. Raabe, "Precipitation Hardening Effects on Extension Twinning in Magnesium Alloys", *International Journal of Plasticity*, Vol. 106, pp. 186–202, 2018.

98. Liu, H., F. X. Lin, P. Zhao, N. Moelans, Y. Wang and J. F. Nie, "Formation and Autocatalytic Nucleation of Co-Zone $\{10\bar{1}2\}$ Deformation Twins in Polycrystalline Mg: A Phase Field Simulation Study", *Acta Materialia*, Vol. 153, pp. 86–107, 2018.

99. Koike, J., "Enhanced Deformation Mechanisms by Anisotropic Plasticity in Polycrystalline Mg Alloys at Room Temperature", *Metallurgical and Materials Transactions A: Physical Metallurgy and Materials Science*, Vol. 36, No. 7, pp. 1689–1696, 2005.

100. Britton, T. B., F. P. Dunne and A. J. Wilkinson, "On the Mechanistic Basis of Deformation at the Microscale in Hexagonal Close-Packed Metals", *Proceedings of the Royal Society A: Mathematical, Physical and Engineering Sciences*, Vol. 471, No. 2178, p. 20140881, 2015.

101. Agnew, S. R., C. N. Tomé, D. W. Brown, T. M. Holden and S. C. Vogel, "Study of Slip Mechanisms in a Magnesium Alloy by Neutron Diffraction and Modeling", *Scripta Materialia*, Vol. 48, No. 8, pp. 1003–1008, 2003.

102. Brown, D. W., S. R. Agnew, M. A. Bourke, T. M. Holden, S. C. Vogel and C. N. Tomé, "Internal Strain and Texture Evolution During Deformation Twinning in Magnesium", *Materials Science and Engineering A*, Vol. 399, No. 1-2, pp. 1–12, 2005.

103. Jain, A., O. Duygulu, D. W. Brown, C. N. Tomé and S. R. Agnew, "Grain Size Effects on the Tensile Properties and Deformation Mechanisms of a Magnesium Alloy, AZ31B, Sheet", *Materials Science and Engineering A*, Vol. 486, No. 1, pp. 545–555, 2008.

104. Clausen, B., C. N. Tomé, D. W. Brown and S. R. Agnew, "Reorientation and Stress Relaxation Due to Twinning: Modeling and Experimental Characterization for Mg", *Acta Materialia*, Vol. 56, No. 11, pp. 2456–2468, 2008.

105. Ahmad, R., B. Yin, Z. Wu and W. A. Curtin, "Designing High Ductility in Magnesium Alloys", *Acta Materialia*, Vol. 172, pp. 161–184, 2019.

106. Xie, K. Y., Z. Alam, A. Caffee and K. J. Hemker, "Pyramidal I Slip in c-axis Compressed Mg Single Crystals", *Scripta Materialia*, Vol. 112, pp. 75–78, 2016.

107. Wang, J., J. P. Hirth and C. N. Tomé, "$(\bar{1}012)$ Twinning Nucleation Mechanisms in Hexagonal-Close-Packed Crystals", *Acta Materialia*, Vol. 57, No. 18, pp. 5521–5530, 2009.

108. LeSar, R., *Introduction to Computational Materials Science: Fundamentals to Applications*, Cambridge University Press, Cambridge, 2013.

109. Swope, W. C., H. C. Andersen, P. H. Berens and K. R. Wilson, "A Computer Simulation Method for the Calculation of Equilibrium Constants for the Formation of Physical Clusters of Molecules: Application to Small Water Clusters", *The Journal of Chemical Physics*, Vol. 76, No. 1, pp. 637–649, 1982.

110. Verlet, L., "Computer Experiments on Classical Fluids. I. Thermodynamical Properties of Lennard-Jones Molecules", *Physical Review*, Vol. 159, No. 1, p. 98, 1967.

111. Wu, Z., M. F. Francis and W. A. Curtin, "Magnesium Interatomic Potential for Simulating Plasticity and Fracture Phenomena", *Modelling and Simulation in Materials Science and Engineering*, Vol. 23, pp. 1–19, 2015.

112. Shinoda, W., M. Shiga and M. Mikami, "Rapid Estimation of Elastic Constants by Molecular Dynamics Simulation Under Constant Stress", *Physical Review B*, Vol. 69, No. 13, pp. 16–18, 2004.

113. Frenkel, D. and B. Smit, *Understanding Molecular Simulation: From Algorithms to Applications*, Second Edition, Elsevier, London, 2023.

114. Tuckerman, M., *Statistical Mechanics: Theory and Molecular Simulation*, Oxford University Press, New York, 2010.

115. Balluffi, R. W., S. M. Allen and W. C. Carter, *Kinetics of Materials*, John Wiley & Sons, New Jersey, 2005.

116. Eshelby, J. D., "The Determination of the Elastic Field of an Ellipsoidal Inclusion, and Related Problems", *Proceedings of the Royal Society of London. Series A. Mathematical and Physical Sciences*, Vol. 241, No. 1226, pp. 376–396, 1957.

117. Mura, T., *Micromechanics of Defects in Solids*, Second Edition, Martinus Nijhoff Publishers, Dordrecht, 2013.

118. Capolungo, L., I. J. Beyerlein and Z. Qwang, "The Role of Elastic Anisotropy on Plasticity in Hcp Metals: A Three-Dimensional Dislocation Dynamics Study", *Modelling and Simulation in Materials Science and Engineering*, Vol. 18, No. 8, 2010.

119. Kapan, E., S. Alkan, C. C. Aydıner and J. K. Mason, "Energetic Contributions to Deformation Twinning in Magnesium", *Modelling and Simulation in Materials Science and Engineering*, Vol. 31, No. 7, p. 075002, 2023.

120. Agnew, S. R., "Wrought Magnesium: A 21st Century Outlook", *JOM*, Vol. 56, No. 5, pp. 20–21, 2004.

121. Agnew, S. R. and Ö. Duygulu, "Plastic Anisotropy and the Role of Non-Basal Slip in Magnesium Alloy AZ31B", *International Journal of Plasticity*, Vol. 21, No. 6, pp. 1161–1193, 2005.

122. Arul Kumar, M., I. J. Beyerlein and C. N. Tomé, "A Measure of Plastic Anisotropy for Hexagonal Close Packed Metals: Application to Alloying Effects on the Formability of Mg", *Journal of Alloys and Compounds*, Vol. 695, pp. 1488–1497, 2017.

123. Wu, Z. and W. A. Curtin, "The Origins of High Hardening and Low Ductility in Magnesium", *Nature*, Vol. 526, No. 7571, pp. 62–67, 2015.

124. Wang, F., S. Sandlöbes, M. Diehl, L. Sharma, F. Roters and D. Raabe, "In Situ Observation of Collective Grain-Scale Mechanics in Mg and Mg-Rare Earth Alloys", *Acta Materialia*, Vol. 80, pp. 77–93, 2014.

125. Üçel, I. B., E. Kapan, O. Türkoğlu and C. C. Aydiner, "In Situ Investigation of Strain Heterogeneity and Microstructural Shear Bands in Rolled Magnesium AZ31", *International Journal of Plasticity*, Vol. 118, pp. 233–251, 2019.

126. Capolungo, L. and I. J. Beyerlein, "Nucleation and Stability of Twins in Hcp Metals", *Physical Review B*, Vol. 78, No. 2, pp. 1–19, 2008.

127. Beyerlein, I. J., R. J. McCabe and C. N. Tomé, "Effect of Microstructure on the Nucleation of Deformation Twins in Polycrystalline High-Purity Magnesium: A Multi-Scale Modeling Study", *Journal of the Mechanics and Physics of Solids*, Vol. 59, No. 5, pp. 988–1003, 2011.

128. Paudel, Y. R., C. D. Barrett and H. El Kadiri, "Full-Field Crystal Plasticity Modeling of $\{10\bar{1}2\}$ Twin Nucleation", J. Jordon, V. Miller, V. Joshi and N. Neelameggham (Editors), *Magnesium Technology 2020*, pp. 141–146, San Diego, 2020.

129. Kondo, R., Y. Tadano and K. Shizawa, "A Phase-Field Model of Twinning and Detwinning Coupled With Dislocation-Based Crystal Plasticity for Hcp Metals", *Computational Materials Science*, Vol. 95, pp. 672–683, 2014.

130. Liu, C., P. Shanthraj, M. Diehl, F. Roters, S. Dong, J. Dong, W. Ding and D. Raabe, "An Integrated Crystal Plasticity-Phase Field Model for Spatially Resolved Twin Nucleation, Propagation, and Growth in Hexagonal Materials", *International Journal of Plasticity*, Vol. 106, pp. 203–227, 2018.

131. Liu, G., H. Mo, J. Wang and Y. Shen, "Coupled Crystal Plasticity Finite Element-Phase Field Model With Kinetics-Controlled Twinning Mechanism for Hexagonal Metals", *Acta Materialia*, Vol. 202, pp. 399–416, 2021.

132. Wang, J., L. Liu, C. N. Tomé, S. X. Mao and S. K. Gong, "Twinning and Detwinning via Glide and Climb of Twinning Dislocations Along Serrated Coherent Twin Boundaries in Hexagonal-Close-Packed Metals", *Materials Research Letters*, Vol. 1, No. 2, pp. 81–88, 2013.

133. Sun, Q., X. Y. Zhang, Y. Ren, J. Tu and Q. Liu, "Interfacial Structure of $\{10\bar{1}2\}$ Twin Tip in Deformed Magnesium Alloy", *Scripta Materialia*, Vol. 90, No. 1, pp. 41–44, 2014.

134. Gong, M., G. Liu, J. Wang, L. Capolungo and C. N. Tomé, "Atomistic Simulations of Interaction Between Basal Dislocations and Three-Dimensional Twins in Magnesium", *Acta Materialia*, Vol. 155, pp. 187–198, 2018.

135. Beyerlein, I. J., L. Capolungo, P. E. Marshall, R. J. McCabe and C. N. Tome, "Statistical Analyses of Deformation Twinning in Magnesium", *Philosophical Magazine*, Vol. 90, No. 16, pp. 2161–2190, 2010.

136. Wang, J., I. J. Beyerlein and C. N. Tomé, "Reactions of Lattice Dislocations With Grain Boundaries in Mg: Implications on the Micro Scale From Atomic-Scale Calculations", *International Journal of Plasticity*, Vol. 56, pp. 156–172, 2013.

137. Barrett, C. D. and H. El Kadiri, "Impact of Deformation Faceting on $\{10\bar{1}2\}$, $\{10\bar{1}1\}$ and $\{10\bar{1}3\}$ Embryonic Twin Nucleation in Hexagonal Close-Packed Metals", *Acta Materialia*, Vol. 70, pp. 137–161, 2014.

138. Giri, D., H. ElKadiri, K. R. Limmer and C. D. Barrett, "An Atomistic Gateway Into Capturing Twin Nucleation in Crystal Plasticity", *Philosophical Magazine Letters*, Vol. 100, No. 8, pp. 375–385, 2020.

139. Kim, D. H., M. V. Manuel, F. Ebrahimi, J. S. Tulenko and S. R. Phillpot, "Deformation Processes in $\left[11\bar{2}0\right]$-textured Nanocrystalline Mg by Molecular Dynamics Simulation", *Acta Materialia*, Vol. 58, No. 19, pp. 6217–6229, 2010.

140. Miyazawa, N., T. Yoshida, M. Yuasa, Y. Chino and M. Mabuchi, "Effect of Segregated Al on $\{10\bar{1}2\}$ and $\{10\bar{1}1\}$ Twinning in Mg", *Journal of Materials Research*, Vol. 30, No. 23, pp. 3629–3641, 2015.

141. Agarwal, G. and A. M. Dongare, "Deformation Twinning in Polycrystalline Mg Microstructures at High Strain Rates at the Atomic Scales", *Scientific Reports*, Vol. 9, No. August 2018, pp. 1–11, 2019.

142. Wang, F., C. D. Barrett, R. J. McCabe, H. El Kadiri, L. Capolungo and S. R. Agnew, "Dislocation Induced Twin Growth and Formation of Basal Stacking Faults in $\{10\bar{1}2\}$ Twins in Pure Mg", *Acta Materialia*, Vol. 165, pp. 471–485, 2019.

143. Zhou, X., H. Su, H. Ye and Z. Yang, "Removing Basal-Dissociated $\langle C+a \rangle$ Dislocations by $\{10\bar{1}2\}$ Deformation Twinning in Magnesium Alloys", *Acta Materialia*, Vol. 217, p. 117170, 2021.

144. Thompson, A. P., H. M. Aktulga, R. Berger, D. S. Bolintineanu, W. M. Brown, P. S. Crozier, P. J. in 't Veld, A. Kohlmeyer, S. G. Moore, T. D. Nguyen, R. Shan, M. J. Stevens, J. Tranchida, C. Trott and S. J. Plimpton, "LAMMPS - A Flexible Simulation Tool for Particle-Based Materials Modeling at the Atomic, Meso, and Continuum Scales", *Computer Physics Communications*, Vol. 271, p. 108171, 2022.

145. Hirel, P., "Atomsk: A Tool for Manipulating and Converting Atomic Data Files", *Computer Physics Communications*, Vol. 197, pp. 212–219, 2015.

146. Stukowski, A., "Visualization and Analysis of Atomistic Simulation Data with OVITO-the Open Visualization Tool", *Modelling and Simulation in Materials Science and Engineering*, Vol. 18, No. 1, p. 015012, 2010.

147. Pond, R. C., J. P. Hirth, A. Serra and D. J. Bacon, "Atomic Displacements Accompanying Deformation Twinning: Shears and Shuffles", *Materials Research Letters*, Vol. 4, No. 4, pp. 185–190, 2016.

148. Zhao, X., H. Chen, N. Wilson, Q. Liu and J. F. Nie, "Direct Observation and Impact of Co-Segregated Atoms in Magnesium Having Multiple Alloying Elements", *Nature Communications*, Vol. 10, No. 1, pp. 1–7, 2019.

149. Wu, Z., B. Yin and W. A. Curtin, "Energetics of Dislocation Transformations in Hcp Metals", *Acta Materialia*, Vol. 119, pp. 203–217, 2016.

150. Dang, K., S. Wang, M. Gong, R. J. McCabe, J. Wang and L. Capolungo, "Formation and Stability of Long Basal-Prismatic Facets in Mg", *Acta Materialia*, Vol. 185, pp. 119–128, 2020.

151. Barnett, D. M. and W. Cai, "Properties of the Eshelby Tensor and Existence of the Equivalent Ellipsoidal Inclusion Solution", *Journal of the Mechanics and Physics of Solids*, Vol. 121, pp. 71–80, 2018.

152. Tromans, D., "Elastic Anisotropy of Hcp Metal Crystals and Polycrystals", *International Journal of Research and Review in Applied Science*, Vol. 6, No. 4, pp. 462–483, 2011.

153. He, C., Y. Zhang, C. Q. Liu, Y. Yue, H. W. Chen and J. F. Nie, "Unexpected Partial Dislocations Within Stacking Faults in a Cold Deformed Mg-Bi Alloy", *Acta Materialia*, Vol. 188, No. 2020, pp. 328–343, 2020.

154. Pond, R. C., A. Serra and D. J. Bacon, "Dislocations in Interfaces in the H.c.p. Metals - II. Mechanisms of Defect Mobility Under Stress", *Acta Materialia*, Vol. 47, No. 5, pp. 1441–1453, 1999.

155. Wang, J. and I. J. Beyerlein, "Atomic Structures of Symmetric Tilt Grain Boundaries in Hexagonal Close Packed (Hcp) Crystals", *Modelling and Simulation in Materials Science and Engineering*, Vol. 20, No. 2, pp. 1–22, 2012.

156. Silverman, R. A., *Modern Calculus and Analytic Geometry*, The McMillan Company, New York, 1969.

157. E, W., W. Ren and E. Vanden-Eijnden, "Simplified and Improved String Method for Computing the Minimum Energy Paths in Barrier-Crossing Events", *The Journal of Chemical Physics*, Vol. 126, No. 16, p. 164103, 2007.

158. Jónsson, H., G. Mills and K. W. Jacobsen, "Nudged Elastic Band Method for Finding Minimum Energy Paths of Transitions", B. J. Berne, G. Ciccotti and D. F. Coker (Editors), *Classical and Quantum Dynamics in Condensed Phase Simulations*, pp. 385–404, World Scientific, Singapore, 1998.

159. Ishii, A., J. Li and S. Ogata, "Shuffling-Controlled Versus Strain-Controlled Deformation Twinning : The Case for Hcp Mg Twin Nucleation", *International Journal of Plasticity*, Vol. 82, pp. 1–12, 2016.

160. Runnels, B., I. J. Beyerlein, S. Conti and M. Ortiz, "A Relaxation Method for the Energy and Morphology of Grain Boundaries and Interfaces", *Journal of the Mechanics and Physics of Solids*, Vol. 94, pp. 388–408, 2016.

161. Eren, E., B. Runnels and J. Mason, "Comparison of Evolving Interfaces, Triple Points, and Quadruple Points for Discrete and Diffuse Interface Methods", *Computational Materials Science*, Vol. 213, p. 111632, 2022.

APPENDIX A: ESHELBY TENSOR FOR ELLIPTIC CYLINDER

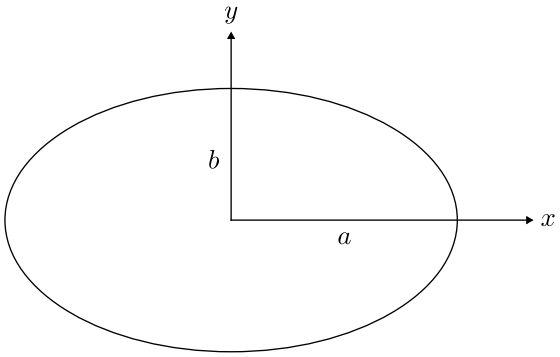

Figure A.1. The elliptic cross-section of the elliptic cylinder geometry. a and b are the radii along the x-axis and y-axis respectively.

The components of the Eshelby tensor S_{ijkl} for an inclusion with elliptic cylinder geometry inside an isotropic medium are

$$S_{1111} = \frac{1}{2(1-\nu)}\left\{\frac{b^2+2ab}{(a+b)^2} + (1-2\nu)\frac{b}{a+b}\right\} \tag{A.1}$$

$$S_{2222} = \frac{1}{2(1-\nu)}\left\{\frac{a^2+2ab}{(a+b)^2} + (1-2\nu)\frac{a}{a+b}\right\} \tag{A.2}$$

$$S_{3333} = 0 \tag{A.3}$$

$$S_{1122} = \frac{1}{2(1-\nu)}\left\{\frac{b^2}{(a+b)^2} - (1-2\nu)\frac{b}{a+b}\right\} \tag{A.4}$$

$$S_{2233} = \frac{1}{2(1-\nu)}\frac{2\nu a}{a+b} \tag{A.5}$$

$$S_{3311} = 0 \tag{A.6}$$

$$S_{1133} = \frac{1}{2(1-\nu)}\frac{2\nu b}{a+b} \tag{A.7}$$

$$S_{2211} = \frac{1}{2(1-\nu)}\left\{\frac{a^2}{(a+b)^2} - (1-2\nu)\frac{a}{a+b}\right\} \tag{A.8}$$

$$S_{3322} = 0 \tag{A.9}$$

$$S_{1212} = \frac{1}{2(1-\nu)}\left\{\frac{a^2+b^2}{2(a+b)^2} + \frac{(1-2\nu)}{2}\right\} \tag{A.10}$$

$$S_{2323} = \frac{a}{2(a+b)} \tag{A.11}$$

$$S_{3131} = \frac{b}{2(a+b)} \tag{A.12}$$

respectively, where a and b are the radii of the elliptic surface as shown in Fig A.1 and ν is the Poisson's ratio for the medium.

In general, the minor symmetries apply for the Eshelby tensor such that $S_{ijkl} = S_{jikl} = S_{ijlk}$ for all ellipsoidal geometries. The components which cannot be obtained by the cyclic permutation are zero, e.g. $S_{2111} = S_{2213} = S_{2312} = 0$.

APPENDIX B: COPYRIGHT STATEMENT

All the figures produced in this work and for which the copyrights are transferred to a publisher for a peer-reviewed publication are reused in the dissertation in compliance with the publisher's policy on the reuse of the copyrighted material.